



HAL
open science

Probabilistic service life modeling of RC structures subjected to the combined effect of chloride-induced corrosion and cyclic loading

Emilio Bastidas-Arteaga

► **To cite this version:**

Emilio Bastidas-Arteaga. Probabilistic service life modeling of RC structures subjected to the combined effect of chloride-induced corrosion and cyclic loading. Civil Engineering. Universidad de los Andes, 2009. English. NNT: . tel-01065817

HAL Id: tel-01065817

<https://theses.hal.science/tel-01065817>

Submitted on 18 Sep 2014

HAL is a multi-disciplinary open access archive for the deposit and dissemination of scientific research documents, whether they are published or not. The documents may come from teaching and research institutions in France or abroad, or from public or private research centers.

L'archive ouverte pluridisciplinaire **HAL**, est destinée au dépôt et à la diffusion de documents scientifiques de niveau recherche, publiés ou non, émanant des établissements d'enseignement et de recherche français ou étrangers, des laboratoires publics ou privés.

EMILIO BASTIDAS-ARTEAGA

**Probabilistic service life model of RC structures
subjected to the combined effect of chloride-induced
corrosion and cyclic loading**

BOGOTÁ 2009

Probabilistic service life model of RC structures subjected to
the combined effect of chloride-induced corrosion and cyclic loading

A dissertation
by
EMILIO BASTIDAS-ARTEAGA

Submitted to the School of Engineering, of
UNIVERSIDAD DE LOS ANDES
in partial fulfillment for the requirements for the Degree of
DOCTOR OF PHILOSOPHY

Approved by:

Committee Chair,	Mauricio Sánchez-Silva
Committee Members,	Alaa Chateauneuf
	Sankaran Mahadevan
	Bernardo Caicedo
Dean School of Engineering,	Alain Gauthier
Assistant Dean,	Rubby Casallas

SEPTEMBER 2009
FIELD: CIVIL ENGINEERING

*A Dios,
a mis abuelos Victoria y Ezequiel,
a mis padres María Teresa y Édgar,
a mi familia y a Elodie.*

ACKNOWLEDGEMENTS

There are many people whose help and contributions I would like to acknowledge. First of all, I am deeply indebted to my principal advisors Dr. Mauricio Sánchez-Silva and Dr. Alaa Chateauf. Beyond having provided critical evaluation of my work and exceptional professional and personal support, they have consistently provided me with opportunities and encouragement that have allowed me to be self sufficient in carrying out my research.

I would like to extend special gratitude to Dr. Franck Schoefs for inviting me to participate in his research group. His discussions and comments were important for the fulfillment of this project.

Thanks to the active collaboration of several French research my research was greatly enhanced. I would therefore also like to mention the kindness and valuable discussions with various individuals: Dr. Philippe Bressolette, Dr. Bruno Capra, Dr. Stéphanie Bonnet, Dr. Géraldine Vilain and Dr. Abdelhafid Khelidj.

I would further like to express my gratitude to the examining committee members, Dr. Bernardo Caicedo and Dr. Sankaran Mahadevan for their helpful and valuable comments on this study.

I would also like to thank the fellow doctoral candidates at the Universidad de los Andes, the French Institute for Advanced Mechanics, Université Blaise Pascal, Université de Nantes and IUT de Saint-Naizaire. Their fruitful discussions helped me to better understand research problems, and without their friendship, it would have been difficult to carry out this study. I am grateful to the staff of all the above mentioned institutions for their administrative support. I am also indebted to Silvia Caro for her assistance in the calibration of the finite element model.

The work reported here has been funded by: the Universidad de los Andes, Colciencias, the French embassy at Colombia, the French Institute for Advanced Mechanics, Université Blaise Pascal, Université de Nantes, Societé Oxand and the MAREO Project. I am thankful to these institutions for their financial support.

I am forever grateful for the unconditional love and support of my family. In particular, I would like to extend my heartfelt gratitude to my mother Maria Teresa Arteaga. She consistently backed all my projects and taught me to forge ahead and accomplish my dreams. Finally, I can never forget the love and encouragement of Elodie Pélissier who was present throughout this project to brighten up my days.

SUMMARY

Durability of reinforced concrete (RC) structures placed in non-aggressive environments is often satisfactory. However, under certain environmental conditions there are internal or external actions that significantly reduce their lifetime. Nowadays, lifetime assessment of deteriorating structures is focused on the isolated effect of the main deterioration processes (corrosion, fatigue, creep, etc.). However, it is paramount to study the combined effect of various deterioration processes because such interaction could reduce structural integrity.

This study proposes a new model for lifetime assessment of RC structures subjected to corrosion-fatigue deterioration processes. The proposed model distinguishes between the following phenomena: chloride penetration, corrosion of reinforcement, concrete cracking and corrosion-fatigue of reinforcing bars. Chloride penetration determines corrosion initiation. Corrosion reduces the cross-section of reinforcing steel. The accumulation of corrosion products in the steel/concrete interface produces concrete cracking. Fatigue causes the nucleation and the propagation of cracks in steel bars. The interaction between corrosion and fatigue can only be taken into account when modeling the combined problem. Thus, pitting corrosion generates stress concentrations that nucleate cracks in the reinforcing bars. Cyclic loading and environmental factors affect the kinematics of crack propagation.

There exists significant uncertainty related to the combined corrosion-fatigue problem. This study also addresses this problem by considering the uncertainty inherent in (1) material properties, (2) model and its parameter and (3) environmental actions. Time-invariant random variables represent the uncertainty of material properties and model. Stochastic processes consider the uncertainty of environmental actions. The proposed stochastic models for weather (temperature and humidity) take into account seasonal variations and global warming. The stochastic models for environmental chloride concentration differentiate between exposure to de-icing salts or the sea. Finally, a fuzzy approach accounts for the uncertainty related to corrosion rate.

The proposed model is applied to the reliability analysis of RC members located in various chloride-contaminated environments. Overall results reveal that the combined effect of corrosion-fatigue depends on environmental conditions and strongly influences the performance of RC structures leading to large reductions in expected lifetime.

Key-words: chloride ingress, corrosion, fatigue, reinforced concrete, reliability.

RESUMEN

La durabilidad de las estructuras del concreto reforzado (CR) situadas en ambientes no agresivos es a menudo satisfactoria. Sin embargo, bajo ciertas condiciones ambientales, existen acciones internas o externas que reducen significativamente su ciclo de vida. Hoy en día, la estimación del ciclo de vida de las estructuras se centra en el efecto aislado de los principales procesos de deterioro (corrosión, fatiga, fluencia, etc.). Sin embargo, es importante estudiar el efecto combinado de varios procesos de deterioro porque su interacción puede reducir la durabilidad estructural.

Este estudio propone un nuevo modelo para la determinación del ciclo de vida de estructuras de CR sujetas al deterioro producido por corrosión y fatiga. El modelo propuesto distingue entre los siguientes fenómenos: penetración de cloruros, corrosión del refuerzo, agrietamiento del concreto y corrosión-fatiga del refuerzo. La penetración de cloruros determina el inicio de la corrosión. La corrosión reduce la sección transversal del acero de refuerzo. La acumulación de productos de corrosión en la interfaz acero/hormigón genera el agrietamiento del concreto. La fatiga induce la nucleación y la propagación de fisuras en las barras de acero. La interacción corrosión-fatiga solamente se puede modelar considerando el comportamiento combinado de estos dos fenómenos. Así, la corrosión localizada genera concentraciones de esfuerzo que crean fisuras en las barras. La carga cíclica y los factores ambientales afectan la cinemática de la propagación de las fisuras.

Existe una incertidumbre significativa en todo el proceso de corrosión-fatiga. Este estudio trata también con este problema considerando la incertidumbre inherente a (1) las propiedades de los materiales, (2) el modelo y sus parámetros y (3) las acciones ambientales. Las variables aleatorias invariantes en el tiempo representan la incertidumbre de las propiedades de los materiales y del modelo. Los procesos estocásticos implementados consideran la incertidumbre de las acciones ambientales. Los modelos estocásticos propuestos para el clima (temperatura y humedad) tienen en cuenta las variaciones estacionales y el calentamiento del planeta. Los modelos estocásticos para la concentración ambiental de cloruros distinguen entre la exposición a las sales de deshielo o marítimas. Finalmente, un análisis difuso toma en cuenta la incertidumbre en el cambio en la tasa de corrosión.

El modelo propuesto se aplica al análisis de confiabilidad de elementos de CR situados en varios ambientes corrosivos. Los resultados demuestran que el efecto combinado corrosión-fatiga depende de las condiciones ambientales y afecta fuertemente el funcionamiento de las estructuras de CR generando reducciones importantes del ciclo la vida.

Palabras clave: ingreso de cloruros, corrosión, fatiga, concreto reforzado, confiabilidad.

CONTENTS

Acknowledgements	vii
Summary	ix
Resumen	xi
Contents	xiii
Notation	xvii
1 Introduction	1
1.1 Background	1
1.2 RC deterioration due to corrosion and fatigue	2
1.3 Research objectives	4
1.4 Thesis organization	4
2 Effect of corrosion-fatigue on the deterioration of reinforced concrete	5
2.1 Introduction	5
2.2 Life-cycle of RC structures subjected to corrosion and fatigue	6
2.3 Chloride ingress into concrete	8
2.3.1 Chloride penetration in saturated concrete	8
2.3.2 Chloride penetration in unsaturated concrete	9
2.4 Corrosion of reinforcement	10
2.4.1 Principles of reinforcement corrosion	10
2.4.2 Time to corrosion initiation	11
2.4.3 Reduction of the reinforcement cross-section caused by corrosion	12
2.4.4 Corrosion rate	14
2.5 Concrete cracking	15
2.6 Corrosion-fatigue of reinforcing bars	19
2.6.1 Basics of fatigue	19
2.6.2 Principles of corrosion-fatigue	23
2.6.3 Corrosion-fatigue in RC structures	25
2.7 Summary and Discussion	26
2.8 Conclusions	28

3	Proposed model of corrosion and fatigue	29
3.1	Introduction	29
3.2	Model of time to corrosion initiation	29
3.2.1	Chloride flow in unsaturated conditions	30
3.2.2	Numerical solution of the governing equations	36
3.2.3	Model verification	38
3.3	Interaction between corrosion and concrete cracking	40
3.3.1	Model of corrosion rate	41
3.3.2	Concrete cracking	42
3.3.3	Coupling between concrete cracking and corrosion rate	45
3.4	Proposed model of corrosion, concrete cracking and fatigue	45
3.4.1	Corrosion initiation and pit nucleation, t_{cp}	47
3.4.2	Pit-to-crack transition, t_{pt}	48
3.4.3	Crack growth, t_{cg}	51
3.5	Summary and conclusions	51
4	Stochastic corrosion-fatigue model	53
4.1	Introduction	53
4.2	Probabilistic framework for reliability analysis	54
4.2.1	Probability of corrosion initiation	55
4.2.2	Probability of failure	55
4.3	Time-invariant random variables	57
4.3.1	Basic concepts of random variables	58
4.3.2	Random variables related to chloride penetration	59
4.3.3	Random variables after corrosion initiation	59
4.4	Stochastic model for humidity and temperature	60
4.4.1	Karhunen-Loève discretization of humidity and temperature	61
4.4.2	Effect of global warming on weather	64
4.5	Stochastic model for environmental chloride concentration	65
4.5.1	Exposure to chlorides from sea water	65
4.5.2	Exposure to chlorides from de-icing salts	66
4.6	Fuzzy corrosion rate model	67
4.7	Summary and conclusions	69
5	Numerical applications	71
5.1	Introduction	71
5.2	Case study 1: Deterministic assessment of chloride ingress	71
5.2.1	Problem description	71
5.2.2	Results	73
5.3	Case study 2: Probabilistic analysis of the time to corrosion initiation	74
5.3.1	Problem description	74
5.3.2	Results	74

5.4	Case study 3: Influence of global warming on corrosion initiation time	77
5.4.1	Problem description	77
5.4.2	Results	78
5.5	Case study 4: Corrosion-fatigue action in saturated environments	83
5.5.1	RC girder and basic considerations	83
5.5.2	Results	86
5.5.3	Effects of corrosion-fatigue on total lifetime	90
5.6	Case study 5: Corrosion-fatigue under realistic environmental conditions	92
5.6.1	Problem description	92
5.6.2	Results	94
5.7	Summary and conclusions	97
6	Closure	99
6.1	Conclusions	99
6.2	Recommendations for future research	102
A	Reliability analysis	105
A.1	Time-invariant reliability analysis	105
A.2	Time-dependent reliability analysis	105
A.3	Methods for reliability assessment	106
A.3.1	Monte Carlo simulation	107
A.3.2	Latin Hypercube sampling	108
B	Basics of fuzzy logic	109
B.1	Fuzzy Sets	109
B.1.1	Characteristics of fuzzy sets	109
B.1.2	Set theoretical operations	110
B.2	Fuzzy inference systems	111
B.2.1	Sugeno fuzzy models	111
	Bibliography	115

NOTATION

Latin letters

a	crack size;
a_c	crack size at which the RC member reaches a limit state of resistance;
A_a	corrosion surface area of steel in concrete at time t ;
A_u^{st}	remaining area of steel for uniform corrosion;
A_p^{st}	remaining area of steel for pitting corrosion;
b_e	correlation length;
B_c	surface chloride transfer coefficient;
B_h	surface humidity transfer coefficient;
B_T	heat transfer coefficient;
c_t	cover thickness;
c_w	width of crack in concrete induced by corrosion;
$c_{w_{lim}}$	critical width of crack in concrete induced by corrosion;
C_{bc}	concentration of bound chlorides;
C_{env}	environmental chloride concentration;
C_{fc}	concentration of chlorides dissolved in the pore solution;
C_{O_2}	oxygen concentration at the concrete surface;
C_{nO_2}	oxygen concentration at the steel surface;
C_s	surface chloride concentration;
C_{tc}	total chloride concentration;
C_{th}	chloride concentration at which corrosion reaction begins;
d	proximity to the sea;
d_0	initial diameter of the reinforcing bar;
d_u	diameter reduction for uniform corrosion;
da/dt	crack growth rate;
dp/dt	pit growth rate;
D_c	effective chloride diffusion coefficient;
D_c^*	apparent chloride diffusion coefficient;
$D_{c,ref}$	reference apparent chloride diffusion coefficient;
D_h	effective humidity diffusion coefficient;
D_h^*	apparent humidity diffusion coefficient;
$D_{h,ref}$	reference apparent humidity diffusion coefficient;
D_o	chloride migration coefficient for the Duracrete model;

D_{O_2}	diffusion coefficient of the oxygen in concrete;
D_{nO_2}	diffusion coefficient of the oxygen at time t_n ;
D_{mO_2}	diffusion coefficient of oxygen in the concrete at time t ;
E_c	elastic modulus of concrete;
E_{st}	elastic modulus of steel;
f	frequency of the cyclic load;
f_{ct}	tensile strength of the concrete;
f_y	yield stress of reinforcement;
f_{yk}	characteristic yield stress of reinforcement;
f'_c	compressive strength of the concrete;
f'_{ck}	characteristic cylinder compressive strength of the concrete;
f'_{cu}	concrete compressive strength over a concrete cube sample;
F	Faraday's constant;
h	relative humidity;
h_c	humidity at which D_c or D_h drops halfway between its maximum and minimum values;
i_{corr}	corrosion rate;
K	stress-intensity factor;
K_c	critical stress-intensity factor;
m_c	factor to account for the reduction of the concrete chloride diffusivity in time;
M	molecular weight of iron;
n	parameter that characterizes the spread of the drop in D_h ;
n_a	electric charge of iron ion;
n_{Fe}	valence of iron;
n_{O_2}	number of O_2 molecule participating in the chemical reaction;
N	number of cycles;
p	pit depth at time t ;
p_0	threshold pit depth to determine the time to pit nucleation;
p_{corr}	probability of corrosion initiation;
p_f	probability of failure;
P_k	characteristic punctual design load;
t	time;
t_{cr}	time to crack initiation in concrete;
t_{cg}	time to crack growth until failure;
t_{cp}	time to corrosion initiation and pit nucleation;
t_e	equivalent hydration (curing) period;
t_{ini}	time to corrosion initiation;
t_n	time at which C_{nO_2} is closer to C_{O_2} ;
t_{pr}	time of crack propagation in concrete;
t_{pt}	time of transition from pit to crack;
t_{ref}	time of exposure at which $D_{c,ref}$ has been evaluated;
t_{sc}	time to severe cracking in steel;

t_{sp}	time to severe cracking in concrete;
T	temperature;
T_{ref}	reference temperature at which the reference diffusion coefficient has been evaluated;
U_c	activation energy of the chloride diffusion process;
w/c	water to cement ratio;
w_e	evaporable water content;
W	amount of corrosion products.

Greek letters

α	ratio between pitting and uniform corrosion depths;
α_0	parameter that represents the ratio of $D_{h,min}/D_{h,max}$;
α_F	binding constant for the Freundlich isotherm;
α_L	binding constant for the Langmuir isotherm;
β_F	binding constant for the Freundlich isotherm;
β_L	binding constant for the Langmuir isotherm;
β	reliability index;
ΔH	activation enthalpy;
ΔK	stress intensity range;
ΔK_{pit}	equivalent stress intensity factor for the pit;
$\Delta\sigma$	stress range;
γ_c	specific weight of concrete;
γ_p	specific weight of pavement;
κ_ϕ	stochastic process describing the humidity or temperature ϕ ;
ν_c	Poisson's ratio of concrete;
$\tilde{\mu}_{ini}$	membership function representing the age for the initial corrosion rate;
$\tilde{\mu}_{max}$	membership function representing the age for the maximum corrosion rate;
ρ_a	density of aggregate;
ρ_c	density of cement;
ρ_{Fe}	density of iron;
ρ_{rust}	density of corrosion products;
ρ_{st}	density of steel;
τ_{crit}	equivalent thickness of corrosion products to produce concrete cracking;
τ_{por}	thickness of porous band around the steel concrete interface.

CHAPTER 1

INTRODUCTION

1.1 Background

Civil infrastructure systems are critical assets for the socioeconomic development of any country. Designing and maintaining these systems for a particular service lifetime have been recognized as critical issues worldwide. The lifetime of a structure can be thought of as the time during which the structure is able to meet specific technical requirements with an acceptable level of safety. Reinforced concrete (RC) structures are characterized by high durability; however, during their operational life, they are subjected to internal and external actions that affect performance, serviceability and safety (Husni, 2003). There are two sources for these actions: operational and environmental. Operational deterioration results from the existence and use of the structure (e.g., service loading, storage of chemical or biological products, etc.). On the other hand, environmental deterioration is caused by aspects such as: temperature, humidity, carbonation, chloride ingress, biodeterioration, etc.

Long-term performance of infrastructures is governed by structural deterioration, which is defined as the loss of capacity due to physical, chemical, mechanical or biological actions. The damage to RC structures resulting from the corrosion of reinforcement is exhibited in the form of steel cross-section reduction, loss of bond between concrete and steel, cracking, and spalling of concrete cover (Clifton, 1993; Fang et al., 2004). Corrosion of steel reinforcement becomes a critical issue for many RC structures, in particular, when they are located in chloride-contaminated environments –e.g., exposure to sea or de-icing salts. Figure 1.1 shows typical examples of corrosion-induced damage. In this case the RC slab presents: (1) some cracks parallel to the direction of reinforcement (Figure 1.1a) and (2) spalling of the concrete cover in some areas (Figure 1.1b).

Corrosion induced by chloride ingress and fatigue produced by cyclic loading are important factors affecting the service life of RC structures. Examples of structures that experience this type of damage are offshore platforms, bridges, chimneys and towers exposed to chlorides and cyclic loading. Nowadays, many deteriorated structures are evaluated for possible repair and continued service because they are situated where their replacement would be economically unfeasible. Bhide (1999) reports that about 173,000 bridges in the United States are structurally deficient or functionally obsolete due in part to corrosion. Thus, developing robust models for prediction and strategies for periodic inspection and maintenance plays a significant role in enabling target reliabilities to be met over a period of continued service (Clifton, 1993; Mori and Ellingwood, 1995).

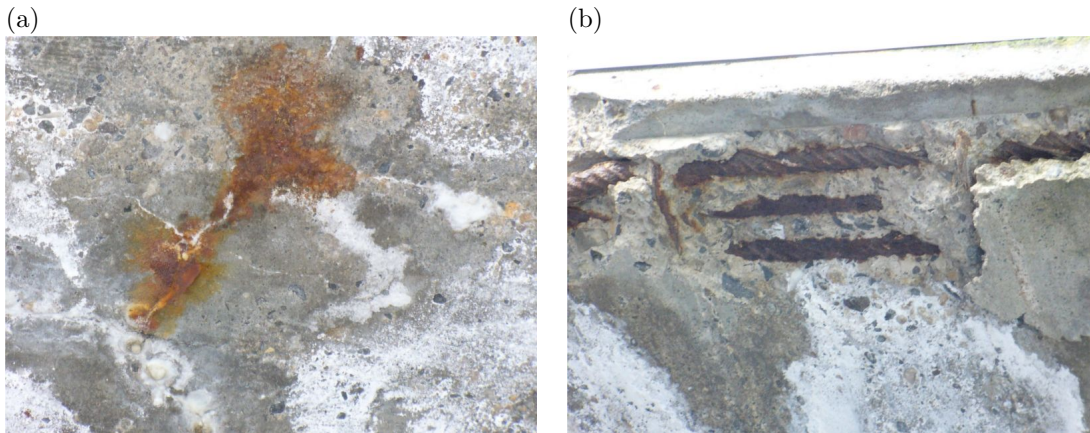


Figure 1.1: Examples of damage induced by corrosion (a) concrete cracking and (b) concrete spalling.

Although corrosion damage rarely leads to sudden structural collapse, there are some examples of structural failure induced by corrosion in RC structures. One example is the collapse of a concrete pedestrian bridge in the year 2000 on the Motor Speedway in Charlotte, North Carolina (USA) injuring more than 100 people; the bridge have been built in 1995 and its collapse was attributed to pitting corrosion on the steel strands encased inside the concrete slabs. Another example is the case on Interstate 70 in Washington County, Pennsylvania (USA), which suffered a disruption of traffic produced by the collapse of a zone on the overpass in 2005 (Grata, 2005). The overpass, opened in 1960, serves now about 40,000 vehicles a day. Besides corrosion induced by de-icing salts, the collapse was induced by a history of being hit by trucks. Five people experienced minor injuries related to the incident. There are many examples where corrosion may also cause aesthetic and serviceability problems.

Regarding corrosion costs, in a study conducted by CC Technologies Laboratories Inc. (2001), it was found that the total direct cost of corrosion in the USA is close to US\$137.9 billion/yr. The industrial and infrastructure sectors which are most likely to suffer corrosion damage are shown in Table 1.1. These values, however, do not include indirect costs to users (delays, inconvenience, lost productivity) which can increase the total costs significantly. Note that transportation infrastructure and highway bridges produce about 27% of the total direct costs (US\$38 billion/yr). Given the size and importance of transportation infrastructures, damage costs reported (Table 1.1) justify research in RC corrosion-related damage process to ensure an optimal level of safety. In summary, corrosion damage is highly related to economical losses, travel delays and personal injuries in transportation infrastructure.

1.2 RC deterioration due to corrosion and fatigue

Chloride penetration results from a complex interaction between physical and chemical processes. However, this phenomenon is commonly simplified when interpreted as a diffusion/convection problem governed by Fick's diffusion law (Tuutti, 1982). However, the following factors should be included in a comprehensive model of chloride penetration (Saetta et al., 1993):

Table 1.1: Cost of corrosion in several industrial and infrastructure sectors.

Industrial sector	Cost US\$ billion/yr
Gas and liquid transmission pipelines	7.0
Hazardous materials storage	7.0
Highway bridges	8.3
Waterways and ports	0.3
Drinking water and sewer systems	36.0
Transportation	29.7
Defense and nuclear waste storage	20.1
Production and manufacturing	17.6
Others	11.9
Total	137.9

- the chloride binding capacity of the cementitious system;
- the time-variant nature and the effects of temperature, humidity and chloride concentration in the surrounding environment;
- the decrease of the chloride diffusivity with concrete age; and
- the one- and two-dimensional flow of chlorides in unsaturated concrete.

Corrosion is the most common form of steel deterioration and consists of material disintegration as a result of chemical or electrochemical actions. Most metals corrode on contact with water (or moisture in the air), acids, bases, salts, and other solid and liquid chemicals. Metals also corrode when exposed to gaseous materials like acid vapors, formaldehyde gas, ammonia gas, and sulfur containing gases (Jones, 1992). Depending on the case, concentrated corrosion can form a pit, or it can spread across a wide area to produce general wastage.

Fatigue is the damage of a material resulting from repeated stress applications (e.g. cyclic loading). Fatigue is conditioned by many factors such as high temperature, i.e. creep-fatigue, and presence of aggressive environments, i.e. corrosion-fatigue (Schijve, 2004; Suresh, 1998). In RC structures, the combined effect of corrosion and fatigue has not been studied in as much detail as their separate effects. Coupled corrosion-fatigue deterioration results from the action of cycling stresses in corrosive environments. Localized corrosion leading to pitting may provide sites for fatigue crack initiation. Several experimental studies have shown that pitting corrosion has been responsible for the nucleation of fatigue cracks in a wide range of steels and aluminum alloys (Kondo, 1989; Ahn et al., 1992; Chen and Duquette, 1992). In such studies, pits are usually found at the origin of the fracture surface. Corrosive agents (e.g., seawater) increase the fatigue crack growth rate (Gangloff, 2005), whereas the morphology of metals/alloys at micro-level governs the pit nucleation sites (Rajasankar and Iyer, 2006). Under these conditions, the formation and growth of pits is influenced by both a corrosive environment and cyclic loads and become a combined damage mechanism.

On the other hand, given that substantial uncertainties are present in all the stages of this process, a probabilistic framework becomes paramount for a realistic assessment of the deterioration process. There are three sources of uncertainties in this problem. The first is related to the randomness of the material properties, the second encompasses the uncertainties in the model and their parameters, and

the third is concerned with the random nature of the environmental actions. Therefore, the lifetime assessment of deteriorating RC structures should be based on probabilistic methods and a comprehensive model that combines the effects of various deterioration processes (e.g., corrosion, fatigue, creep, etc.).

1.3 Research objectives

The overall purpose of this study is to develop a probabilistic lifetime prediction model for RC structures under the combined effect of corrosion and fatigue.

The specific objectives are:

1. To review critically the state-of-the-art approaches to lifetime modeling of RC structures subjected to corrosion and fatigue and to provide a discussion on the advantages and shortcomings of each one.
2. To build a mechanical model to estimate the lifetime of RC structures under the combined effect of corrosion and fatigue.
3. To propose a stochastic mechanical model that considers the inherent uncertainties of the combined deterioration process.
4. To carry out sensitivity analyses of the governing parameters of the phenomena including the influence of weather conditions.

1.4 Thesis organization

This manuscript is divided into six chapters. Chapter 2 presents a critical review of the state-of-the-art of corrosion-fatigue in RC structures. This literature survey presents the recent advances on modeling of the main stages of the deterioration process: chloride ingress, reinforcement corrosion, concrete cracking and fatigue-corrosion of reinforcing bars.

Based on the literature review, chapter 3 describes the proposed model that considers corrosion and fatigue. The beginning of the chapter presents the interaction of chloride ingress with environmental factors. Afterwards, the study focuses on the interaction between corrosion and concrete cracking. Finally, it describes the effect of cyclic loading on deterioration.

Chapter 4 outlines the stochastic approach. This chapter starts with a revision of the principles of uncertainty modeling. It then defines the methods and the limit state functions used in reliability analysis. It concludes with the description of the proposed models for the random/fuzzy variables.

Taking into account the proposed deterioration model and the probabilistic framework presented in chapter 4, chapter 5 integrates all aspects of the thesis by carrying out various numerical examples. The first part of the chapter investigates the kinematics of chloride penetration under real environmental exposure conditions, including global warming. The second part studies the combined effect of corrosion and fatigue under actual environmental conditions evaluating the impact on the reliability of RC structures.

Chapter 6 contains the conclusions of this study including recommendations for future research.

CHAPTER 2

EFFECT OF CORROSION-FATIGUE ON THE DETERIORATION OF REINFORCED CONCRETE

2.1 Introduction

Reinforced concrete (RC) structures are subjected to external actions that affect performance, serviceability and safety during their operational lives (Husni, 2003). Depending on their origin, these actions can be external or internal and produce physical, chemical, biological and mechanical damage (Table 2.1). External actions are divided into operational and environmental actions. While operational actions result from the existence and the use of the structure (e.g., service loading, storage of chemical or biological products, etc.), environmental actions are induced by exposure to the surrounding environment (e.g., temperature, humidity, carbonation, chloride ingress, biodeterioration, etc.). On the other hand, internal actions are divided into intrinsic and induced. Intrinsic actions are related to volumetric changes that depend on material properties, construction procedures and other factors such as drying or thermal shrinkages. Induced actions are produced by changes made to improve the strength of RC or are the result of RC behavior under constant loading (i.e. prestressed or post-tensioned concrete and creep).

Under optimal conditions, the durability of RC structures is high and the variation of the structural reliability over time is not significant. However, for structures located in aggressive environments this might not be the case. Some examples of aggressive environments are those in which there is:

1. high relative humidity (i.e., between 60% and 98%);
2. cycles of humidification and drying, of freezing and defrosting;
3. high carbon dioxide concentrations (e.g., carbonation in urban atmospheres);
4. high concentration of chlorides or other salts (e.g., marine environments); or
5. high concentration of sulfates and small amounts of acids (e.g., sewer pipes or residual water treatment plants).

There is a larger number of RC structures subjected to the action of chloride-induced corrosion. According to Bhide (1999), about 173,000 bridges of the interstate highway system in the United States are structurally deficient or functionally obsolete, due in part to corrosion. Other examples of

Table 2.1: Actions affecting the performance of RC structures

Origin	Actions	Related damage
External	Operational	Physical, chemical and biological
	Environmental	Physical, chemical and biological
Internal	Intrinsical	Physical and mechanical
	Induced	Mechanical

structures exposed to this type of damage are ports, quays, offshore platforms, chimneys and towers situated close to the sea or exposed to the application of de-icing salts.

In addition to corrosion, another major cause of RC deterioration is fatigue produced when structures are subjected to cyclic loading. Chloride penetration in RC structures leading to reinforcement corrosion has been widely studied. However, further research is still required in order to couple corrosion with other deterioration mechanisms (e.g., fatigue, creep, biodeterioration, etc.). Thus, this study focuses on modeling the time-dependent reliability problem of the interaction between corrosion and fatigue.

The main objectives of this chapter are:

1. to describe the basic principles and existing models of chloride ingress, corrosion and fatigue;
2. to identify the phenomena that produce deterioration in RC structures subjected to corrosion and fatigue; and
3. to establish the research targets for modeling RC deterioration.

Section 2.2 covers the stages of the life-cycle of RC structures subjected to corrosion and fatigue. Since the principles for the models controlling the kinematics at each stage are different (e.g., diffusion, electrochemical, mechanical), this chapter discusses the following phenomena separately:

- chloride ingress into concrete (section 2.3),
- reinforcement corrosion (section 2.4),
- concrete cracking (section 2.5), and
- corrosion-fatigue of reinforcing bars (section 2.6).

The final section 2.7 summarizes the studied phenomena and discusses the models presented.

2.2 Life-cycle of RC structures subjected to corrosion and fatigue

In any deterioration process, structural reliability is time-dependent. For RC structures bearing the combined action of corrosion and fatigue, the structure's life-cycle can be divided into four stages (Figure 2.1):

Stage 1: Immediately after construction, initial structural reliability, β_{ini} , is maximum; then, deterioration is initiated as a result of environmental actions such as: chloride ingress, carbonation, sulfate attack, biodeterioration, erosion, etc. Nevertheless, the consequences of these actions do

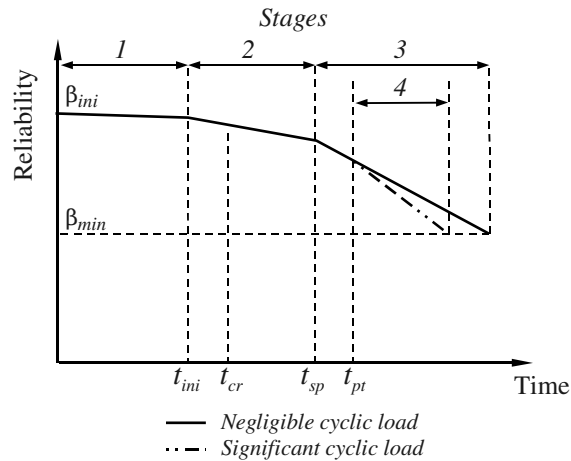


Figure 2.1: Reliability profile for RC structures subjected to corrosion and fatigue.

not have significant impact on reliability until their individual or joint actions create the necessary conditions to depassivate the protective layer of the steel, e.g., low pH of concrete, specific combination of temperature and water, and oxygen availability. As a result of this new state, the reinforcement bars start to be actively corroded; the time at which this happens is called *time of corrosion initiation* (t_{ini}). If there are no cracks that accelerate the chloride ingress process, the length of this stage depends mainly on the material properties and on the surrounding environmental conditions.

Stage 2: As soon as corrosion starts, corrosion products appear. Since these products have a lower density, they occupy the porous zone of the concrete surrounding the steel. When the total amount of corrosion products exceeds the amount needed to fill the porous zone, expansive pressure is induced on concrete initiating the cracking process (Liu, 1996; Liu and Weyers, 1998). In this stage, two phenomena called *crack initiation* and *crack propagation* are initiated. The former is defined as the condition for which a hairline crack of 0.05mm width appears (Vu et al., 2005). The time required to reach this point is called *time to crack initiation* (t_{cr}). The latter is measured in terms of the crack width, c_w . The time required to reach the threshold crack size, $c_{w_{lim}}$ (e.g., $c_{w_{lim}} = 0.5\text{mm}$) is called *time to severe cracking*, (t_{sp}). This stage also depends on the interaction of corrosion with other deterioration processes. For example, when the structure is subjected to cyclic loading, corrosion can nucleate cracks in the reinforcement, which are in turn propagated by the loading process. This stage plays an important role in structural safety.

Stage 3: When crack width reaches a specific threshold value, there is significant increment in the corrosion rate as a result of the increase in water and oxygen availability as well as in concrete electrical conductivity (i.e. Schiessl and Raupach (1997)). This increment in the corrosion rate causes a significant decay in reliability. During this stage, the structure is more sensitive to the actions of other deterioration processes. This stage ends when reliability reaches a minimum level β_{min} after which time the serviceability and/or the safety of the structure are seriously compromised.

Stage 4: The existence of this stage depends on the magnitude and frequency of cyclic loading. If cyclic loading is negligible, the deterioration mechanism leading to failure is the reduction of the cross-section of steel reinforcement caused by corrosion (stage 3). However, when the structure is subjected to significant cyclic loading, the corrosion pits can nucleate a crack in the reinforcing bars. The time after which the crack is nucleated is called *time to transition from pit to crack*, t_{pt} . After t_{pt} , the decrease in reliability is controlled by crack propagation in the bars. This stage ends when the crack size reaches a threshold value that defines structural failure.

2.3 Chloride ingress into concrete

2.3.1 Chloride penetration in saturated concrete

Fick's second law of diffusion is usually used to study the flow of chlorides into concrete (Tuutti, 1982); then for the unidirectional case (flow in x -direction):

$$\frac{\partial C_{fc}}{\partial t} = D_c \frac{\partial^2 C_{fc}}{\partial x^2} \quad (2.1)$$

where C_{fc} is the concentration of chlorides dissolved in the pore solution, t is the time and D_c is the effective chloride diffusion coefficient. Assuming that concrete is an homogeneous and isotropic material with the following initial conditions: (1) the concentration is zero at $t = 0$ and (2) the chloride surface concentration is constant; the free chloride ion concentration $C(x, t)$ at depth x after time t for a semi-infinite medium is:

$$C(x, t) = C_s \left[1 - \operatorname{erf} \left(\frac{x}{2\sqrt{D_c t}} \right) \right] \quad (2.2)$$

where C_s is chloride surface concentration and $\operatorname{erf}()$ is the error function.

The closed-form solution of Fick's diffusion law can be easily used to predict the time to corrosion initiation. However, equation 2.2 is valid only when RC structures are saturated and subjected to constant concentration of chlorides on the exposed surfaces. These conditions are rarely present for real structures because concrete is a heterogeneous material that is frequently exposed to time-variant surface chloride concentrations. Besides, this solution does not consider chloride binding capacity, concrete aging and other environmental factors such as temperature and humidity (Saetta et al., 1993).

The European Union project, Duracrete (2000), proposes an expression similar to equation 2.2 which considers the influence of material properties, environment, concrete aging and concrete curing on the chloride diffusion coefficient:

$$C(x, t) = C_s \left[1 - \operatorname{erf} \left(\frac{x}{2\sqrt{k_e k_t k_c D_o \left(\frac{t_o}{t}\right)^{n_D} t}} \right) \right] \quad (2.3)$$

where k_e is an environmental factor, k_t is a factor which considers the influence of the test method to measure the diffusion coefficient D_o , k_c is an influence factor for concrete curing, D_o is the chloride migration coefficient measured at defined compaction, curing and environmental conditions, t_o is the

reference period to measure D_o and n_D is the age factor. The lifetime assessment resulting from this approach is better than the one provided by equation 2.2 because it accounts for type of concrete, w/c ratio, environmental exposure (submerged, tidal, splash and atmospheric), aging and concrete curing. In addition, the strength of the Duracrete approach lies in considering the randomness related to chloride penetration. However, this method does not take into consideration: (1) chloride flow in unsaturated conditions, (2) time-variant nature and the influence of surface chloride concentration, environmental humidity and temperature; (3) chloride binding capacity; and (4) the flow of chlorides in two-dimensions. Since corrosion rates are higher in unsaturated conditions where the availability of both oxygen and water are large, a comprehensive model should include these phenomena.

2.3.2 Chloride penetration in unsaturated concrete

For chloride diffusion in unsaturated environments, Saetta et al. (1993) proposed a model that takes into account the effects of temperature and humidity on chloride diffusivity. This approach establishes a partial differential equation (PDE) for each physical problem (chloride transport, humidity diffusion and heat transfer) and solves the system of PDEs numerically. The model of Saetta et al. (1993) has been revised and updated by Martín-Pérez et al. (2001). The study of Martín-Pérez et al. (2001) focuses on the numerical solution and includes a corrosion rate model that takes into account the availability of oxygen at the corrosion cell. This approach allows modeling chloride ingress in one or two dimensions (Figure 2.2a). From these results, Martín-Pérez et al. (2001) highlighted the importance of including the “corner” effects in the assessment of the time to corrosion initiation for small RC members (e.g., beams, columns). This model provides a realistic prediction of chloride penetration into concrete. However, the solution of the governing equations can only be obtained numerically and requires a larger number of parameters to find the solution.

The problem of chloride ingress into unsaturated concrete has also been addressed by Ababneh et al. (2003) who considered the interaction between the governing equations of chloride and humidity diffusion. In contrast to the model of Saetta et al. (1993), the chloride diffusion coefficient includes a factor to account for the influence of the aggregates and the cement paste. The moisture and chloride profiles were also obtained numerically by implementing an alternating-direction implicit finite-difference method. The numerical solution was compared with experimental results which in large part coincided with experimental data (Figure 2.2b). Although including a new factor to account for the effect of concrete composition may lead to a better prediction, this improvement adds more parameters which are difficult to obtain from standard laboratory tests. Furthermore, the chloride diffusion coefficient does not take into account the effect of temperature.

There are other models which, in addition to diffusion, the chloride penetration assessment includes the interaction with other mechanisms such as electrical coupling between ions, chemical activity effects and advection caused by capillarity suction flow –i.e., Samson and Marchand (2007). The multi-ionic transport model is based on the extended Nernst-Planck equation with a convective term and is valid for saturated or unsaturated conditions. Since this model needs an important number of characterizing parameters and the methods suggested by the authors to find them are not yet widely used, it is preferable to use the model of Saetta et al. (1993) for chloride flow in unsaturated conditions.

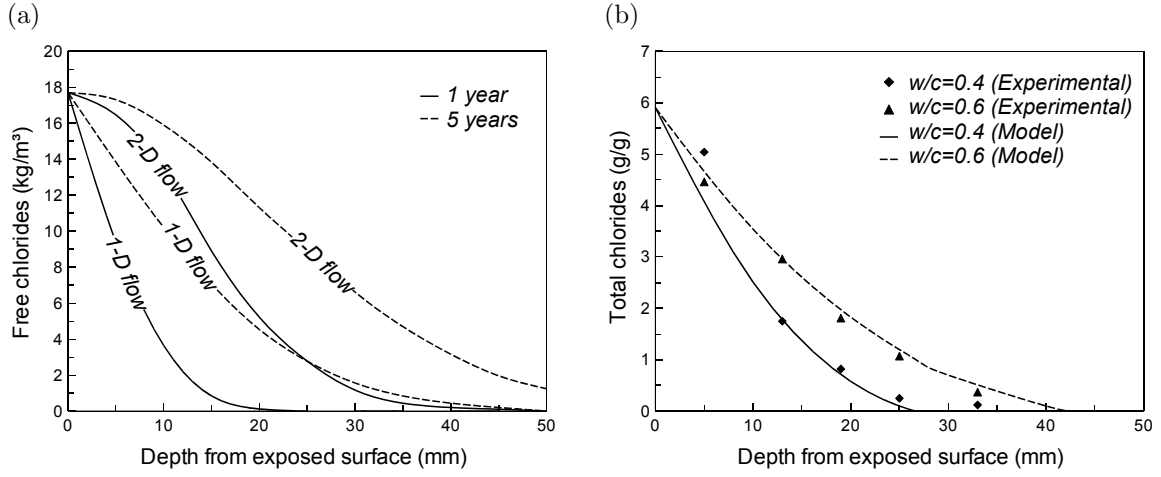


Figure 2.2: Chloride diffusion in unsaturated environments (a) flow in one- and two-dimensions (adapted from Martín-Pérez et al., 2001); (b) comparison with experimental results (adapted from Ababneh et al., 2003).

2.4 Corrosion of reinforcement

2.4.1 Principles of reinforcement corrosion

The reinforcement in RC structures is physically protected from corrosion by concrete and by a protective passive layer of corrosion products placed around bars. Under normal conditions, the protection provided by the concrete inhibits corrosion initiation because: (1) the pH of concrete is very high (pH up to 13) and (2) the electrical conductivity is low. Nevertheless, during the life-cycle of the structure external actions favor electrochemical corrosion. Corrosion initiation also requires the presence of water and oxygen at the corrosion cell (Figure 2.3). The corroding cell of steel in concrete consists of an anode, a cathode, an electrical conductor, and an electrolyte (concrete pore solution). The driving electrical force for steel corrosion is induced by the potential difference between the anode and the cathode. Usually, the process can be divided into primary and secondary electrochemical processes. The primary electrochemical processes start when the concentration of chlorides at the corrosion cell reaches a threshold value destroying the protective passive film. At this point, the iron Fe at the anode is oxidized forming ferrous ions Fe^{2+} :



At the surface of the cathodic region, the released electrons e^{-} flow through the steel to react with both oxygen and water to form hydroxyl ions OH^{-} (see Figure 2.3):



The anodic product Fe^{2+} reacts with the hydroxyl ions to produce a white precipitate of ferrous

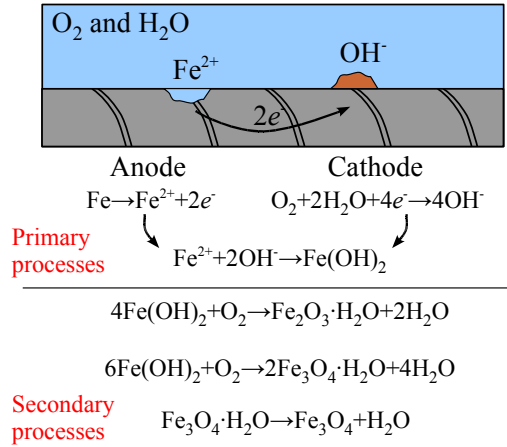


Figure 2.3: Corrosion processes.

hydroxide $Fe(OH)_2$:



The corrosion products are generated during the secondary electrochemical processes. Various corrosion products can be produced depending mainly on the pH of the solution, oxygen supply and moisture content. The ferrous hydroxide can be converted to hydrated ferric oxide $Fe_2O_3 \cdot H_2O$, commonly called ordinary red-brown rust:



Corrosion products can become black magnetite, i.e., Fe_3O_4 , which is preceded by the formation of green magnetite $Fe_3O_4 \cdot H_2O$:



2.4.2 Time to corrosion initiation

The threshold chloride concentration C_{th} is defined as the chloride concentration at which the rust passive layer of steel is destroyed and the corrosion reaction begins. The value of the chloride threshold concentration is based on the definition of the threshold concentration level. Duracrete (2000) proposes two definitions for this parameter:

Definition 1 threshold chloride content leading to depassivation of the steel surface and to visible corrosion damage on the concrete surface (it does not consider the effect of weather).

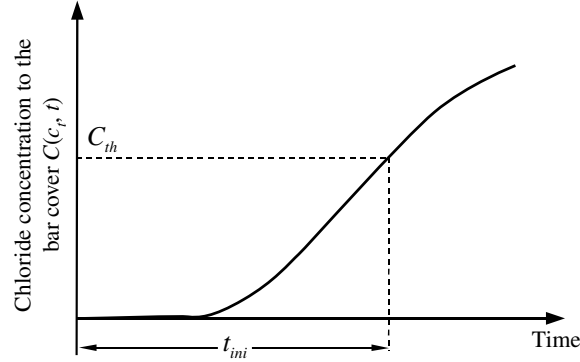


Figure 2.4: Computation of the time to corrosion initiation.

Definition 2 threshold chloride content leading to deterioration or damage of the concrete structure.

The chloride threshold concentration obtained from this definition corresponds to the appearance of a concrete crack width of 0.1 mm and is valid for concrete cover thicknesses higher than 25 mm.

The time to corrosion initiation, t_{ini} , is computed by comparing the chloride concentration in the concrete depth $C(c_t, t)$ with the threshold concentration C_{th} (Figure 2.4). Then t_{ini} is obtained when the chloride concentration at the bar cover reaches the threshold concentration C_{th} . Closed-form solutions to compute t_{ini} have been proposed based on the solution of Fick's law and on the Duracrete model. For instance, for the conventional solution of Fick's law (equation 2.2) t_{ini} is obtained when $C(x, t)$ is equal to C_{th} and x is equal to the concrete cover thickness c_t as follows:

$$t_{ini} = \frac{c_t^2 \left[\operatorname{erf}^{-1} \left(1 - \frac{C_{th}}{C_s} \right) \right]^{-2}}{4D_c} \quad (2.10)$$

On the other hand, for unsaturated conditions, the time to corrosion initiation has to be determined numerically.

2.4.3 Reduction of the reinforcement cross-section caused by corrosion

The reduction of the reinforcement cross-section produced by corrosion can take two basic forms: uniform or pitting (Figure 2.5). Uniform corrosion is usually found in structures subjected to carbonation while pitting corrosion is typical of chloride-induced corrosion. This section presents some models to estimate the remaining area of steel in both cases.

In the case of uniform corrosion (Figure 2.5a), the bar diameter reduction at time t , $d_u(t)$, in mm is computed as:

$$d_u(t) = d_0 - 0.0232 \int_{t_{ini}}^t i_{corr}(t) dt \quad (2.11)$$

where d_0 , is the initial diameter of the bar (in mm) and $i_{corr}(t)$ is the corrosion rate; $i_{corr}(t)$ is given

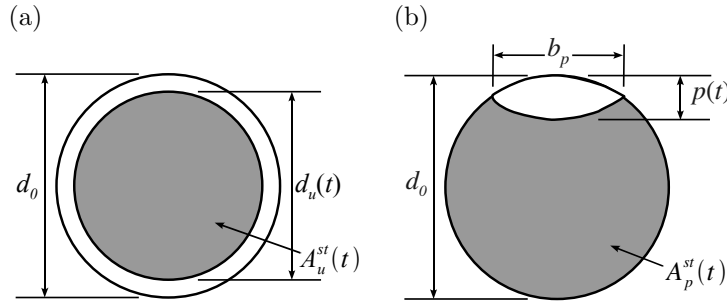


Figure 2.5: (a) Uniform corrosion; (b) Pitting corrosion.

in $\mu\text{A}/\text{cm}^2$. Then, the remaining area of steel at time t , A_u^{st} , becomes:

$$A_u^{st}(t) = \pi \frac{d_u(t)^2}{4} \quad (2.12)$$

On the other hand, chloride-induced corrosion is typically characterized by highly localized corrosion (i.e. pitting corrosion). According to González et al. (1995), the maximum penetration of pitting corrosion is about four to eight times that of uniform corrosion. If the ratio between pitting and uniform corrosion depth is related by a pitting factor α , the pit depth at time t , is computed from (Figure 2.5b):

$$p(t) = 0.0116\alpha \int_{t_{ini}}^t i_{corr}(t) dt \quad (2.13)$$

Based on the configuration presented in Figure 2.5b, Val and Melchers (1997) proposed the following relationships to compute the cross-sectional area of the pit:

$$A_{pit}(t) = \begin{cases} A_1 + A_2 & \text{for } p(t) \leq \frac{d_0}{\sqrt{2}} \\ \frac{\pi d_0^2}{4} - A_1 + A_2 & \text{for } \frac{d_0}{\sqrt{2}} < p(t) \leq d_0 \\ \frac{\pi d_0^2}{4} & \text{for } p(t) > d_0 \end{cases} \quad (2.14)$$

where

$$A_1 = 0.5 \left[\theta_1 \left(\frac{d_0}{2} \right)^2 - b_p \left| \frac{d_0}{2} - \frac{p(t)^2}{d_0} \right| \right] \quad (2.15)$$

$$A_2 = 0.5 \left[\theta_2 p(t)^2 - b_p \frac{p(t)^2}{d_0} \right] \quad (2.16)$$

$$\theta_1 = 2 \arcsin \left(\frac{b_p}{d_0} \right) \quad (2.17)$$

Table 2.2: Ranges of i_{corr} suggested for exposure classes of EN206.

Exposure Classes	Corrosion rate ($\mu\text{A}/\text{cm}^2$)
D1 Moderate humidity	0.1–0.2
D2 Wet - rarely - dry	0.1–0.5
D3 Cyclic wet - dry	0.5–5.0
S1 Airborne sea water	0.5–5.0
S2 Submerged	0.1–1.0
S3 Tidal zone	1.0–10

$$\theta_2 = 2 \arcsin \left(\frac{b_p}{2p(t)} \right) \quad (2.18)$$

$$b_p = 2p(t) \sqrt{1 - \left(\frac{p(t)}{d_0} \right)^2} \quad (2.19)$$

Thus, the remaining area of steel at time t for the case of pitting corrosion, A_p^{st} , is:

$$A_p^{st}(t) = \pi \frac{d_0^2}{4} - A_{pit}(t) \quad (2.20)$$

2.4.4 Corrosion rate

In RC structures, the corrosion rate, i_{corr} , controls the reduction of the diameter of reinforcing bars after corrosion initiation. It can be expressed either as a corrosion current density (in $\mu\text{A}/\text{cm}^2$) or as the loss of metal per unit surface area, per unit of time (in $\mu\text{m}/\text{year}$). The relationship between both units can be obtained by using Faraday's law for general corrosion –i.e., $1\mu\text{A}/\text{cm}^2 = 11.6\mu\text{m}/\text{year}$ (Jones, 1992).

The experience on RC structures indicates that values of corrosion rates higher than $1 \mu\text{A}/\text{cm}^2$ are seldom measured while values between 0.1 and $1 \mu\text{A}/\text{cm}^2$ are the most frequent (Geocisa and the Torroja Institute, 2002). Corrosion rates lower than 0.05 – $0.1 \mu\text{A}/\text{cm}^2$ indicate that the steel is passive. For RC structures located in chloride-contaminated environments, the European norm 206 (EN206) (Geocisa and the Torroja Institute, 2002) suggests the corrosion rates presented in Table 2.2. Note that the higher corrosion rates correspond to unsaturated conditions where the availability of oxygen and water provide optimal conditions to increase i_{corr} .

Some approaches for modeling corrosion rate consider that corrosion is controlled by the availability of oxygen at the corrosion cell –i.e., Yokozeki et al. (1997) and Liang et al. (2005). Both models estimate the concentration of oxygen at the corrosion cell by mean of Fick's diffusion law and the corrosion rate is obtained from Faraday's law by considering the electric number oxygen molecule participating in the chemical reaction. The estimated values of corrosion rate agree with the ranges reported in the literature. Nonetheless, after corrosion initiation, the model does not account for (1) the time-dependence of i_{corr} reported by Liu and Weyers (1998) and (2) the availability of water at the surface of the reinforcing bar.

On the basis of least square regression of the data from 44 chloride contaminated slab specimens over a 5-year period, Liu and Weyers (1998) proposed a time-variant model of corrosion rate. The governing parameters of this model are chloride content, temperature at the depth of the steel surface and ohmic resistance of concrete. Although the model was developed based on a comprehensive experimental analysis, the technique used to measure i_{corr} does not consider the effect of concrete cover which has been established as a critical parameter by Vu (2003).

Vu (2003) concluded that the kinematics of the corrosion rate is dominated by different physical factors that depend on the relative humidity (RH) and also suggested three different cases that relate the concrete electrical resistivity and availability of oxygen with the corrosion rate:

1. $50\% < RH \leq 75\%$: the corrosion rate is controlled by the concrete electrical resistivity.
2. $75\% < RH \leq 90\%$ (transition area): the corrosion rate depends on both the concrete electrical resistivity and oxygen availability.
3. $RH > 90\%$: the corrosion rate is dominated by the availability of oxygen.

On the basis of the experimental data reported by Liu (1996), Vu and Stewart (2000) and Vu (2003) also proposed a time-dependent corrosion rate model. However, the applicability of this model is limited to RC structures in environments having 80% RH. The model uses the approach of Yokozeki et al. (1997) to account for the effects of concrete cover c_t and w/c ratio as:

$$i_{corr}(t) = \begin{cases} \frac{37.8(1-w/c)^{-1.64}}{c_t} & \text{for } t_{ini} + 1 \text{ year} \geq t > t_{ini} \\ \frac{32.13(1-w/c)^{-1.64}}{c_t} (t - t_{ini})^{-0.3} & \text{for } t > t_{ini} + 1 \text{ year} \end{cases} \quad (2.21)$$

where c_t is expressed in mm and t is given in years. Figure 2.6 presents some examples of corrosion rates determined with this model. In all cases the corrosion rate is constant during the first year and decreases with time after corrosion initiation. Vu and Stewart (2000) stated that the formation of corrosion products on the steel surface affects i_{corr} by the reduction of:

1. the diffusion of the iron ions away from the steel surface, and
2. the area ratio between the anode and cathode.

Figure 2.6a shows the effect of w/c ratio on corrosion rate for $c_t = 40\text{mm}$ and Figure 2.6b describes the impact of concrete cover for $w/c = 0.5$. The corrosion rates are higher for concretes with higher w/c ratios and lower concrete cover thicknesses.

2.5 Concrete cracking

Concrete cracking is produced by the accumulation of corrosion products at the steel/concrete interface. As can be observed in Figure 2.7, the time to crack initiation depends mainly on corrosion rate, concrete cover, tensile strength of concrete and type of corrosion products (Liu and Weyers, 1998; Alonso et al., 1998). As discussed in section 2.4, the rate of production of rust products is highly dependent on environmental conditions. Both analytical and numerical approaches to simulate concrete cracking aim at computing the stresses generated by the accumulation of corrosion products. Some

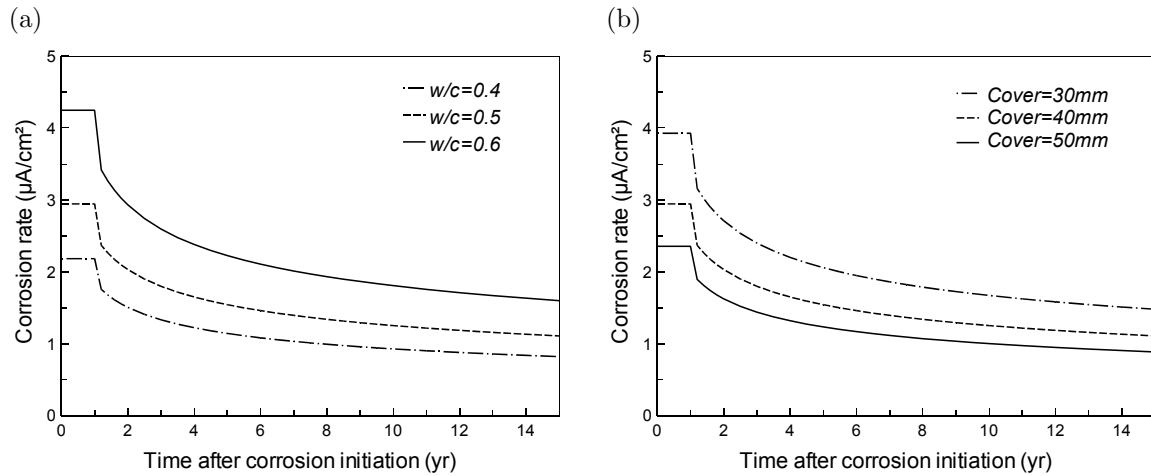


Figure 2.6: Corrosion rate after corrosion initiation: (a) influence of w/c , (b) effect of cover.

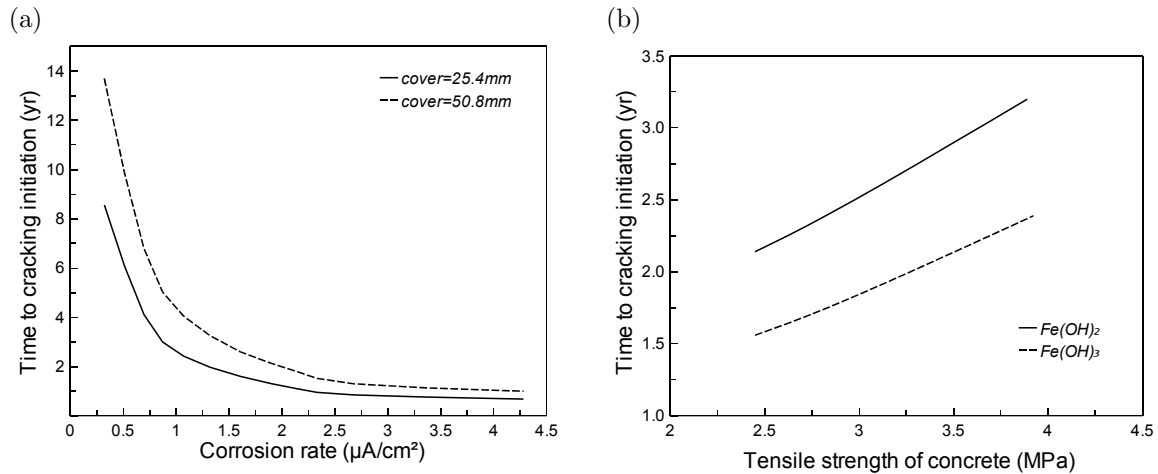


Figure 2.7: Effects on time to cracking initiation (adapted from Liu and Weyers, 1998): (a) corrosion rate and cover depth; (b) tensile strength of concrete and type of corrosion products.

analytical approaches simplify the geometry and assume that cracking starts when the stress level inside the concrete reaches its tensile strength; while others fit experimental tests to compute the time to concrete cracking directly. Numerical approaches use finite or boundary elements to predict both crack initiation and growth and require an important computational effort. Although sophisticated numerical models may lead to more accurate results, analytical solutions have shown considerable agreement with experimental observations. This section presents some analytical models.

Bazant (1979) proposed a model that assumes that the accumulation of corrosion products induces uniform radial pressure which produces cracking. Depending on both reinforcing bar spacing and diameter, he defined two modes of cracking. The first corrosion mode generates planar cracks of 45° inclination emanating from opposite points on the surface of the reinforcing bar. In the second mode the crack produced by corrosion runs parallel to the surface from one bar to another. Bazant's results indicate that the time to crack initiation depends on the type and density of corrosion products,

Table 2.3: Model-predicted times to cracking for outdoor specimens (Liu and Weyers, 1998)

Series	Steel diameter	Cover depth	Corrosion rate	Predicted time to cracking	Observed time to cracking
OA2859.6	16 mm	48 mm	2.41 $\mu\text{A}/\text{cm}^2$	1.53–2.06 yr	1.84 yr
OB3859.6	16 mm	70 mm	1.79 $\mu\text{A}/\text{cm}^2$	3.34–4.49 yr	3.54 yr
OE(F)18512.0	27 mm	27 mm	3.75 $\mu\text{A}/\text{cm}^2$	0.56–0.75 yr	0.72 yr

corrosion rate, concrete cover, reinforcing bar diameter and concrete properties. However, Vu (2003) stated that there are two problems with this model:

1. the assumption that all corrosion products contribute to build up of tensile stress is not realistic since it is likely that some rust products will diffuse within the concrete pore structures and consequently relieve tensile stresses in the concrete; and
2. the assumption of a constant rate of rust production might lead to an underestimation of the time to crack initiation.

The model proposed by Bažant (1979) has been revised by Liang et al. (2002) to change the condition of concrete cracking initiation. A comparative analysis found that the modified version proposed by Liang et al. (2002) results in an increase in the critical value for concrete cracking initiation ranging from 11 to 38%. Although this modification improves the prediction, the problems pointed out by Vu (2003) are not solved.

On the basis of a 5-year experimental study on RC slabs, Liu and Weyers (1998) developed a time to corrosion cracking model based on the amount of corrosion products. This model suggests that concrete cracking starts when the amount of corrosion products fills the interconnected void space around the reinforcing bar, increasing tensile stresses to the maximum for concrete. This study considered the influence of the following factors: corrosion rate, concrete cover depth, reinforcing steel bar spacing, and size. The prediction of the time to crack initiation uses the same principles proposed by Bažant (1979); however, Liu and Weyers model improves the prediction by introducing:

- a time-dependent rate of rust production; and
- a new parameter to account for the thickness of a porous zone around the steel/concrete interface.

Table 2.3 presents a comparison between both observed and predicted times to cracking initiation for the model of Liu and Weyers (1998). It can be observed that times to cracking are within the predicted values by the model.

Andrade et al. (1993) performed accelerated concrete cracking tests where the RC beams were artificially corroded by an imposed current. They monitored both the amount of current (and loss of bar cross-section) needed to induce the crack at the surface and the evolution of crack width. The authors found that visible cover cracking (crack width less than 0.1mm) is produced when a cross section loss of $20\mu\text{m}$ is reached. Two equations to estimate (1) the time cracking initiation (visible cover cracking) and (2) the time to a crack growth to a crack width of 0.3mm were developed based on these experimental observations. These equations are function of bar diameter and corrosion rate.

The problem of crack growth after cracking initiation was also addressed by Vu et al. (2005) who developed a model on the basis of accelerated corrosion tests. Figure 2.8 presents the time to cracking

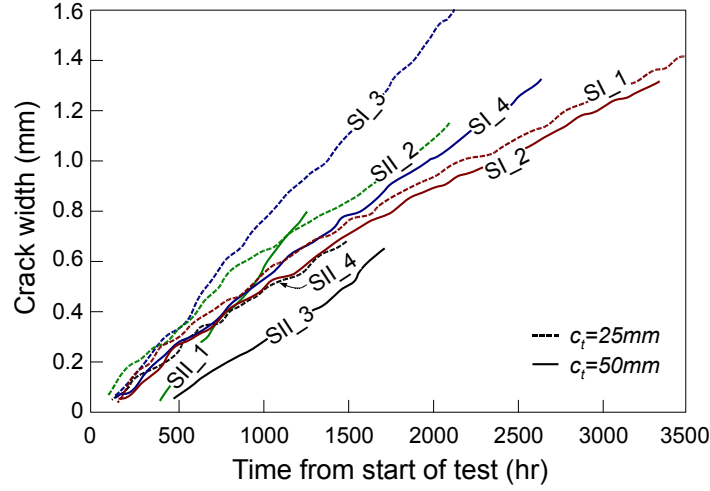


Figure 2.8: Results from crack initiation and propagation models (adapted from Vu et al., 2005).

Table 2.4: Comparison of experimental results with crack initiation prediction models (Vu et al., 2005)

Specimen	w/c	f'_c	f_{ct}	c_t	Time to crack initiation (hours)		
					Test result	Liu and Weyers (1998)	Andrade et al. (1993)
SI.1	0.50	20	3.06	25	134.0	123.0 (-8.0%)	325.0
SI.2	0.50	20	3.06	50	194.7	247.0 (32.0%)	325.0
SI.3	0.50	43	4.16	25	116.0	83.0 (-28.0%)	325.0
SI.4	0.50	43	4.16	50	155.7	154.0 (-1.0%)	325.0
SII.1	0.58	42	3.94	50	402.8	146.0 (-64.0%)	325.0
SII.2	0.58	42	3.94	25	136.1	81.0 (-40.0%)	325.0
SII.3	0.45	53	4.55	50	490.7	143.0 (-70.9%)	325.0
SII.4	0.45	53	4.55	25	223.1	79.0 (-65.0%)	325.0

initiation (beginning of the lines) and the measured crack sizes for eight RC specimens. Each specimen is characterized by different w/c ratio, cover thickness and concrete compressive and tensile strengths (Table 2.4). If the time to concrete crack propagation t_{pr} is defined as the time to reach a critical crack size (i.e., 0.5 mm), Vu et al. (2005) propose to estimate t_{pr} as a function of concrete cover, corrosion rate and w/c ratio.

Concerning the time to crack initiation, Vu et al. (2005) compared the predictions made with the models of Liu and Weyers (1998) and Andrade et al. (1993) with experimental data (Table 2.4). Although the Liu and Weyers model predicted values closer to the experimental results, there are important differences between the predicted and observed values. Nevertheless, given that the crack initiation time is quite short compared with the time to excessive cracking, the accuracy of the Liu and Weyers model for crack initiation will not significantly influence the assessment of time to excessive cracking.

2.6 Corrosion-fatigue of reinforcing bars

2.6.1 Basics of fatigue

Fatigue is defined as the progressive and localized damage produced when a material is subjected to repeated stresses. Fatigue failure is characterized by fracture after application of a large number of load cycles with amplitude lower than the instantaneous strength of material. The process of fatigue damage can be divided into the following stages (Suresh, 1998):

1. sub-structural and micro-structural changes in the material which cause nucleation and permanent damage,
2. creation of microscopic cracks,
3. growth and coalescence of microscopic flaws to form *dominant* cracks, which may lead to catastrophic failure (from a practical stand-point, this stage of fatigue generally constitutes the demarcation between crack initiation and propagation),
4. stable propagation of macro-cracks, and
5. structural instability or complete fracture.

Commonly the total fatigue life (expressed as a number of cycles), N_t , can be computed as the sum of two stages:

$$N_t = N_i + N_p \quad (2.22)$$

where N_i is the number of cycles required to initiate a fatigue crack and N_p is the number of cycles required to propagate a fatigue crack to a critical size. There is no a clear limit between N_i and N_p ; sometimes, preexisting cracks in structural members can reduce or eliminate N_i .

Classical approaches to model fatigue are:

1. Wöhler curve or total fatigue life approach; and
2. Linear Elastic Fracture Mechanics (LEFM).

The Wöhler approach estimates total fatigue life without distinction between N_i and N_p . LEFM focuses on estimation of N_p from an existing crack. Both approaches will be briefly discussed in following sections.

2.6.1.1 Total fatigue life approach

The fatigue test consists of subjecting a specimen to repeated loading cycles at fixed amplitude in order to calculate the number of cycles to failure N_t . The results of these tests are represented as a fatigue curve; know as Wöhler's curve (Figure 2.9a). For Wöhler's curve, the horizontal axis represents the number of cycles –i.e., N , and the vertical axis corresponds to the cyclic stress range S . Based on experimental results, Wöhler's curve is described as:

$$S = A_w N^{-B_w} \quad (2.23)$$

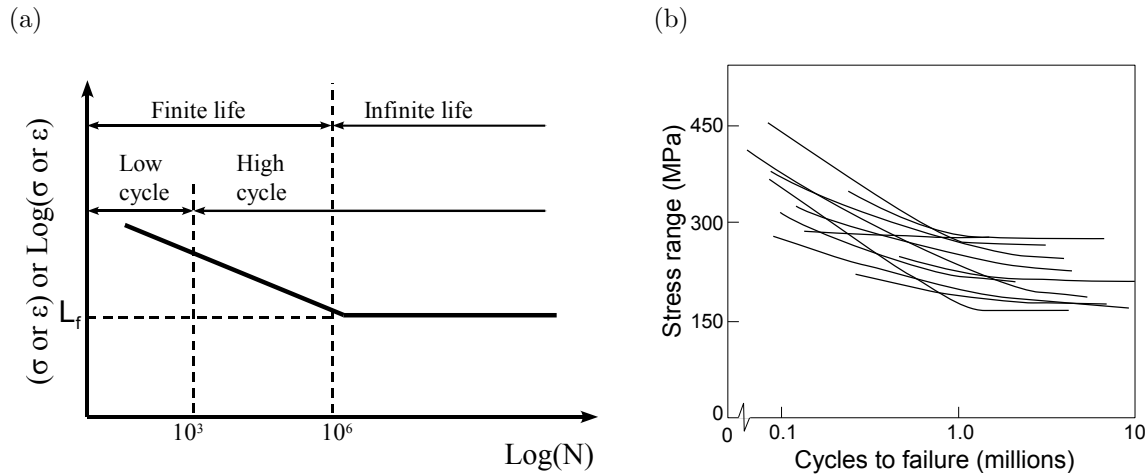


Figure 2.9: (a) Wöhler's curve. (b) Wöhler's curves for reinforcing bars (adapted from ACI Committee 215, 1993).

or

$$\log(S) = \log(A_w) - B_w \log(N) \quad (2.24)$$

where S is the magnitude of the cyclic stress, N is the corresponding fatigue life in number of cycles and A_w and B_w are material constants. In some materials (e.g., steel) there is a value of stresses or strains under which the material can resist an infinite number of cycles. This value is called *endurance limit* or *fatigue limit*, L_f (Figure 2.9a).

The ACI Committee 215 (1993) relates the fatigue strength of reinforcing bars to the following physical characteristics:

- minimum stress;
- bar size and type of beam;
- geometry of deformations;
- yield and tensile strength;
- bending; and
- welding.

Figure 2.9b shows a set of S-N curves obtained from fatigue tests on concrete beams in North America (ACI Committee 215, 1993). These curves were obtained for bars varying in diameter from 16 to 35 mm with minimum stress levels ranging from -0.10 to 0.43 of their tensile yield strength. It can be noted that there is a transition from a steeper to a flatter slope in the vicinity of one million cycles indicating that there exists an endurance limit at 150 MPa. These results show that reinforcing bars exhibit a practical fatigue limit.

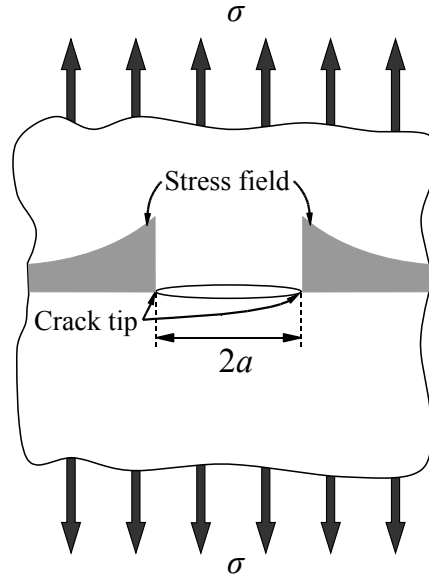


Figure 2.10: Cracked plate subjected to a remote tensile stress.

2.6.1.2 LEFM approach

LEFM is a method used to characterize the fracture behavior of notched elements (e.g., Figure 2.10) based on stress analysis in the vicinity of a crack. This method studies the growth (propagation) of cracks until it reaches its critical size. There are two alternative approaches for fracture analysis: the energy criterion and the stress intensity approach. In the former, fracture occurs when the available energy is sufficient to overcome the material integrity. In the latter, each stress component generated by crack propagation is proportional to a constant, K , which is commonly called *stress intensity factor*. Therefore, fracture occurs when the value of K reaches a critical stress-intensity factor, K_c . The stress intensity factor is used in LEFM to characterize the stress field at the crack tip and depends on material properties, element geometry, environmental conditions, loading rate and constraints. This parameter is employed to relate both, the stress level σ , and the crack size a as (Figure 2.10):

$$K = \sigma\sqrt{a}f(g) \quad (2.25)$$

where $f(g)$ is a function that depends on the geometry of the member and the crack size. This function has been determined for various geometrical configurations, crack sizes, orientations, shapes and load conditions (Suresh, 1998; Barsom and Rolfe, 1999).

Experimental evidence has shown that there are three stages of crack growth (Schijve, 2004). These stages are easily observable from a double log plot between the crack growth rate da/dN and the stress intensity range ΔK (Figure 2.11). The first, called *threshold ΔK region*, is associated with a threshold value, ΔK_{th} , which indicates that ΔK -values below this threshold are too low to cause crack growth. The second, also known as *Paris ΔK region*, is essentially linear. Since many structures operate in this region, most research efforts have been directed to study crack growth inside this region. Finally,

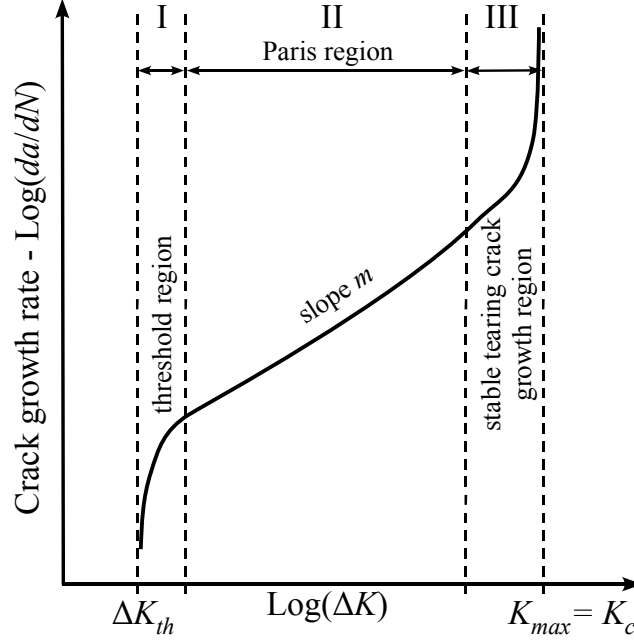


Figure 2.11: Regions of the crack growth rate as a function of ΔK

at the *stable tearing crack growth region* crack growth rates are extremely high and little fatigue life is involved. A complete failure of the specimen is reached when $K_{max} = K_c$.

Figure 2.11 indicates that there is linear behavior in region II. Although many curve fits to this region have been suggested, the Paris-Erdogan law proposed in the early 1960s, is widely accepted:

$$\frac{da}{dN} = C_p(\Delta K)^{m_p} \quad (2.26)$$

where a is the crack size, N is the number of cycles, and C_p and m_p are material constants. The fatigue-crack-propagation life, N_p may be calculated by integrating equation 2.26, as follows:

$$N_p = \int_{a_0}^{a_c} \frac{da}{C_p(\Delta K)^{m_p}} \quad (2.27)$$

where a_0 is the initial crack length and a_c is the critical (final) crack length leading to failure.

Salah el Din and Lovegrove (1982) experimentally determined the parameters C_p and m_p for reinforcing bars. On the basis of their results, they divided fatigue-crack-propagation life into two stages (1) early growth life N_{p1} and (2) intermediate growth life N_{p2} -i.e., $N_p = N_{p1} + N_{p2}$. Then equation 2.27 becomes:

$$N_p = \int_{a_0}^{a_1} \frac{da}{C_{p1}(\Delta K)^{m_{p1}}} + \int_{a_1}^{a_c} \frac{da}{C_{p2}(\Delta K)^{m_{p2}}} \quad (2.28)$$

where a_1 is the crack depth at the transition from early growth to intermediate growth. This transition occurs when the crack size induces a stress intensity factor equal to $\Delta K = 9\text{MPa}\sqrt{m}$. The material constants reported by Salah el Din and Lovegrove (1982) are: $C_{p1} = 3.83 \times 10^{-29}$, $m_{p1} = 20.863$,

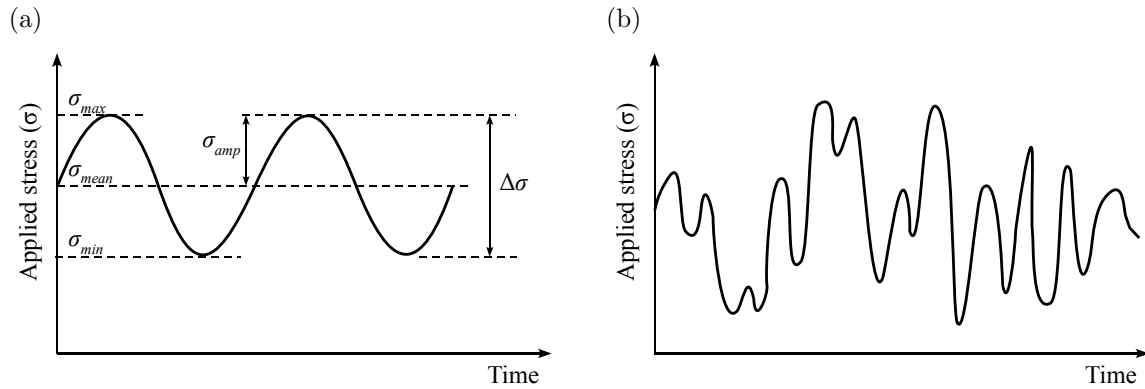


Figure 2.12: Fatigue loading. (a) Simple constant-amplitude cyclic-stress fluctuation. (b) Random-stress loading.

$$C_{p2} = 3.16 \times 10^{-12} \text{ and } m_{p2} = 3.143.$$

2.6.1.3 Fatigue loading

Figure 2.12 illustrates two typical cyclic loading processes: *constant-amplitude loading* (Figure 2.12a) and *random-stress loading* (Figure 2.12b). The constant-amplitude loading is represented by various parameters (See Figure 2.12a):

- a constant stress range $\Delta\sigma$, that is the algebraic difference between the maximum stress, σ_{max} , and the minimum stress, σ_{min} , within the cycle –i.e., $\Delta\sigma = \sigma_{max} - \sigma_{min}$;
- a mean stress, σ_{mean} , that is the algebraic mean of σ_{max} and σ_{min} in the cycle –i.e., $\sigma_{mean} = (\sigma_{max} + \sigma_{min})/2$;
- an alternating stress or stress amplitude, σ_{amp} , that is half of the stress range in a cycle –i.e., $\sigma_{amp} = \Delta\sigma/2 = (\sigma_{max} - \sigma_{min})/2$; and finally,
- a stress ratio, R , that represents the relative magnitude of the minimum and maximum stresses in each cycle –i.e., $R = \sigma_{min}/\sigma_{max}$.

2.6.2 Principles of corrosion-fatigue

Localized corrosion leading to pitting may provide sites for fatigue crack initiation. Several experimental studies have shown that pitting corrosion has been responsible for the nucleation of fatigue cracks in a wide range of steels and aluminum alloys (Kondo, 1989; Ahn et al., 1992; Chen and Duquette, 1992). Corrosive agents (e.g., seawater) increase the fatigue crack growth rate (Gangloff, 2005), whereas the morphology of metals/alloys at micro-level governs the pit nucleation sites (Rajasankar and Iyer, 2006). Consequently, the formation and growth of pits is influenced by both a corrosive environment and cyclic loads which form a combined damage mechanism.

Goswami and Hoepfner (1995) proposed a seven-stage conceptual model to assess this phenomenon in which the electrochemical effects in pit formation and the role of pitting in fatigue crack nucleation

are considered; they are:

1. electrochemical stage and pit nucleation,
2. pit growth,
3. competitive mechanisms between pit growth and fatigue crack nucleation,
4. chemically, “short” crack growth,
5. transition from “short crack” to “long crack”,
6. long crack growth, and
7. corrosion-fatigue crack growth until instability.

Pitting nucleation and growth rates (stages 1 and 2) are highly influenced by electrochemical parameters and external factors such as surface conditions, time of exposure, stress-strain conditions, environmental factors and thermal history among others (Goswami and Hoepfner, 1995). During the deterioration process two mechanisms called pit growth and fatigue damage interact until pit growth nucleates a crack (stage 3). This transition is reached when the pit growth rate is lower than the damage produced under fatigue. The nucleated fatigue cracks are propagated towards the region pre-damaged by corrosion (stage 4). The transition from “short crack” to “long crack” is produced when the crack reaches a critical size (stage 5). After the transition, the cracks grow towards the un-damaged region causing failure (stages 6 and 7).

Other research studies focus on particular stages of the process. For instance, Kondo (1989) proposed a transition model from pit to crack based on two criteria: fatigue threshold and rate competition, which is further discussed by Chen et al. (1996). Figure 2.13 depicts a conceptual framework for delineating the damaging process of corrosion-fatigue on the basis of the transition criteria. It is observed that the pit size is dominated by pitting corrosion in the early stage of the process. However, there are two possibilities for the transition:

1. *Fatigue threshold criterion:* the transition is produced if the stress intensity factor of the equivalent surface crack growth for the pit ΔK_{eq} is equal to the threshold intensity factor for transition ΔK_{th} . Since the threshold condition ΔK_{th} is defined by the pit size, the transition is independent of frequency. For instance, point *a* in Figure 2.13 shows a transition estimated from this criterion for two different frequencies f_1 and f_2 . Note that transition point *a* is the same for both frequencies and that frequency controls crack growth after *a*.
2. *Rate competition criterion:* the transition occurs when the crack growth rate is equal to the pit growth rate. The points *b* and *c* in Figure 2.13 illustrate the transition estimated with this criterion. It is observed that, in contrast to the fatigue threshold criterion, the transitions depend on frequency.

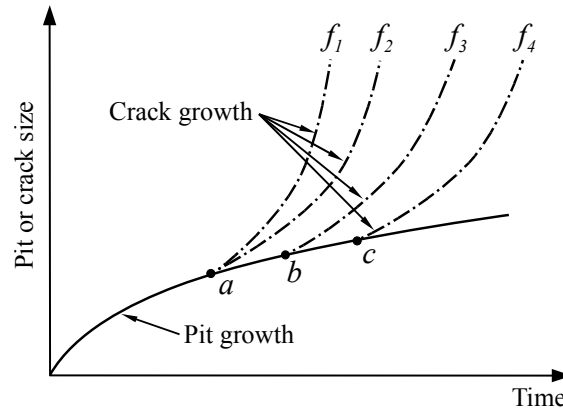


Figure 2.13: Conceptual framework for the damaging process of corrosion fatigue (adapted from Chen et al., 1996).

Table 2.5: Ultimate strength for RC beams under static and cyclic loading (Ahn and Reddy, 2001).

Beam size m	w/c	Ultimate strength	
		Static (MPa)	Cyclic (MPa)
$0.30 \times 0.30 \times 2.36$	0.3	25.1	23.7
$0.30 \times 0.30 \times 2.36$	0.4	23.6	22.5
$0.15 \times 0.15 \times 1.18$	0.4	31.4	29.7
$0.15 \times 0.15 \times 1.18$	0.6	28.8	28.1

2.6.3 Corrosion-fatigue in RC structures

In RC structures, the combined effect of corrosion and fatigue has not been studied in much detail. It is generally accepted that plain concrete has low tensile strength, and therefore, a limited fatigue strength. Fatigue strength of plain concrete depends on the range of loading, rate of loading, eccentricity of loading, load history, material properties and environmental conditions (ACI Committee 215, 1993). Since this study focuses on reinforced concrete, the fatigue strength of concrete will be assumed as negligible.

There exists a limited amount of experimental tests on corrosion fatigue in RC structures. Ahn and Reddy (2001) performed an experimental study to evaluate the durability of RC beams subjected to fatigue loading and chloride ingress. The test included 16 beams and accounted for the influence of static and cyclic loading for different water/cement ratios ($w/c = 0.3, 0.4, \text{ and } 0.6$). The marine tidal zone was simulated by alternate filling and draining of a tank, and a galvanostatic corrosion technique was used to accelerate corrosion of the reinforcement. The ultimate strength of the beams was tested after 78,000 cycles by applying four-point flexural loading. Table 2.5 summarizes some of the Ahn and Reddy results. It was observed that beams subjected to cyclic loading during the exposure period showed lower ultimate strength than those subjected to static loading.

Recently, Jaffer and Hansson (2008) carried out an experimental study aimed at determining the influence of the combined effect of concrete cracking on corrosion rate for three loading conditions (unloaded, static and dynamic or cyclic). The experimental procedure included 36 beams made of ordinary Portland cement concrete and high performance concrete with w/c ratios of 0.46 and 0.35,

Table 2.6: Ranges of corrosion rates obtained using LPR measurements.

Region	Range of i_{corr}
Cracked	1–4 $\mu\text{A}/\text{cm}^2$
Non-submerged	0.05–0.3 $\mu\text{A}/\text{cm}^2$
Submerged	0.4–1 $\mu\text{A}/\text{cm}^2$

respectively. All beams (unloaded and loaded) were cracked one day prior to their exposure to chlorides. The same loads of 2.1 kN for 70 h were applied for the loaded beams after exposure to chloride solution. The dynamic load was applied at a frequency of 0.5 Hz. After this period, the loads were reduced to about 0.68 kN to maintain maximum deflection of 3 mm at the top end of the beams. The beams subjected to dynamic loading were subsequently exposed to the new load for 1–2.5 h per day.

The beams were placed upright in a solution with a 3% chloride content which reached above their mid-point level (just above the central crack). Corrosion measurements were carried out at three locations in each beam which are located in: (1) the non-submerged region; (2) the submerged cracked region and (3) the submerged uncracked region. The beams were subjected to cycles of wetting (2 weeks) and drying (2 weeks). The microcell corrosion was monitored by two techniques: potentiostatic linear polarization resistance (LPR) and potentiodynamic (cyclic) polarization. Macrocell corrosion was monitored using electrochemical noise measurements.

Table 2.6 presents the ranges of corrosion rates reported by Jaffer and Hansson (2008) using LPR measurements for ordinary Portland cement. Since these values are determined based on the polarized area, this technique does not reveal accurate corrosion rates. However they are useful when differentiating between actively corroding and passive rebars. In general, the highest corrosion rates correspond to the cracked regions of the beams. According to Geocisa and the Torroja Institute (2002), corrosion rates within this range denote active corrosion. For the non-submerged regions the corrosion rates evidence that steel is passive. Finally, for the submerged regions, the corrosion rates also indicate corrosion activity. The most important findings of this study can be summarized as follows:

- corrosion occurred only at intersections of the reinforcing bar with cracks in the concrete;
- high performance concrete was more protective than ordinary Portland cement concrete and
- the type of loading had less impact on corrosion than the type of concrete and exposure conditions.

Jaffer and Hansson’s study contributed to the understanding of the kinematics among corrosion, fatigue and concrete cracking. However, it seems that the results underestimate the effect of the dynamic/cyclic load because the cyclic loading is interrupted during exposure to chlorides.

2.7 Summary and Discussion

This chapter presented a literature review of the most relevant models used to assess all stages of corrosion-fatigue deterioration of RC (chloride penetration, corrosion of reinforcement, concrete cracking and corrosion-fatigue of reinforcement). The summary and a discussion on the advantages and the shortcomings of these models are presented in this section:

Chloride penetration. Several models to assess chloride ingress into concrete can be found in the literature. The most common approach is based on the analytical solution to Fick's law, which can be easily implemented. However, the assumptions behind the model are difficult to justify under real exposure conditions. The Duracrete model improves the analytical solution by considering the influence of material properties, environmental exposure, aging and concrete curing. Moreover, it includes a probabilistic description of the model's governing parameters. Nevertheless, the solution is only valid for saturated conditions and does not consider the following factors:

- the chloride binding capacity;
- the time-dependence of temperature, humidity and surface chloride concentration; and
- the flow of chlorides in two dimensions.

On the other hand, the models for chloride penetration in unsaturated conditions consider all the factors mentioned above leading to a more realistic assessment. However, the solution can only be obtained numerically and requires a larger number of parameters. Despite the constraints of existing models, both the conventional solution to Fick's law and the Duracrete model are useful for carrying out sensitivity studies focused on deterioration after corrosion initiation.

Reinforcement corrosion. This chapter features a number of issues concerning the corrosion of steel reinforcement induced by chloride ingress. After presenting the basic principles of corrosion of reinforcing bars, it describes the general method used to compute the time to corrosion initiation and the cross-section reduction models. Two approaches to model corrosion rate are also presented and discussed. In general, the corrosion rate models available in the literature show considerable agreement with experimental values. However, further research is required to:

1. properly represent the kinematics of the corrosion rate when the RC member is cracked, and
2. take into account the influence of relative humidity, oxygen availability and concrete electrical resistivity.

Concrete cracking. The literature review shows that concrete cracking depends on concrete quality (expressed as w/c ratio, concrete cover and concrete strength) and corrosion rate. The time to severe cracking is divided into two stages called:

1. time to cracking initiation and
2. time of crack propagation.

The first stage is reached when the pores around the bar are filled and the excess of pressure breaks the concrete. The last stage estimates the time to reach a critical crack width. Since the times obtained for Liu and Weyers (1998) (for the first stage) and for Vu et al. (2005) (for the second stage) agree with experimental data, these models will be used in the present study to integrate the effects of concrete cracking.

Corrosion-fatigue of reinforcement. Experimental studies on fatigue of reinforcing bars evidence that a practical fatigue limit exists that should be considered when the RC structure is subjected to cyclic loading (ACI Committee 215, 1993). There are two methods that can be applied to determine the fatigue life of reinforcing bars: *total fatigue life* approach and *LEFM* approach. While the total fatigue life approach estimates the total number of cycles to failure including crack initiation and propagation, the LEFM approach determines the fatigue crack propagation life. Salah el Din and Lovegrove (1982) established the parameters that characterize crack propagation for the LEFM approach. Such parameters do not consider the interaction between corrosion and fatigue. Although further research in corrosion-fatigue characterization of reinforcing bars is required, these parameters can be implemented for illustrative purposes.

Corrosion-fatigue damage has been frequently observed in aircraft structures made up of aluminum, titanium and steel alloys. At the beginning, the cross-sectional reduction of steel is governed by pitting corrosion. The nucleation of pits induces stress concentrations that may generate a crack under the action of fatigue loading. Finally, when a crack is created, fatigue becomes the main failure mechanism. The combined action of corrosion and fatigue in RC structures has not been studied in detail. Nevertheless, experimental testing evidences the lifetime reduction when corrosion and fatigue interact (Ahn and Reddy, 2001; Jaffer and Hansson, 2008). Therefore, it is necessary to develop a model to estimate the lifetime length of RC structures subjected to this kind of deterioration.

2.8 Conclusions

The following conclusions are drawn from the present chapter:

1. This chapter presented and discussed all the stages of the RC deterioration process and the basic principles that control them. Chloride penetration is modeled by a diffusion/convection process. Reinforcement corrosion is controlled by electrochemical principles. Concrete cracking depends on the corrosion rate and material properties. Corrosion-fatigue of reinforcement is governed by the interaction between corrosion rate and cyclic loading.
2. Chloride-induced RC deterioration is a complex process that depends on factors such as material properties, weather conditions, loading, etc. and is controlled by diffusion, electrochemical and mechanical principles. The RC deterioration process results from the interaction between: (1) chloride penetration, (2) reinforcement corrosion, (3) concrete cracking and (4) corrosion-fatigue of reinforcement.
3. The research needs in this field were established on the basis of the literature survey and its discussion. In general, further research is required in material characterization and the use of stochastic models. The assessment of chloride penetration should be improved by coupling realistic models of weather and chloride concentration at the surface. The corrosion model needs to consider the action of concrete cracking and weather. Although the proposed models for concrete cracking are representative of the phenomenon, they should include the effect of relative humidity. Finally, it is necessary to develop a model to predict the behavior of RC structures subjected to corrosion and fatigue.

CHAPTER 3

PROPOSED MODEL OF CORROSION AND FATIGUE

3.1 Introduction

Chloride-induced RC deterioration results from the interaction between three phenomena: (1) chloride ingress, (2) concrete cracking, and (3) fatigue of the reinforcement. Chloride ingress includes diffusion and convection and it is highly dependent on the concrete properties and the conditions in the surrounding environment. Corrosion induced by chloride penetration generates concrete cracking when the accumulation of rust products reaches a threshold. Concrete cracking is governed by tensile stresses generated by corrosion products. Excessive concrete cracking can accelerate corrosion by increasing the oxygen and water availability in the corrosion cell. As a result, under the presence of cyclic loading, corrosion pits can nucleate cracks in the reinforcement bars. Reinforcement fatigue takes into account the interaction between electrochemical and mechanical principles.

The objectives of this chapter are:

1. to describe the basic principles and the numerical solution of the chloride penetration model;
2. to develop a model to account for the interaction between corrosion and concrete cracking; and
3. to propose a coupled model of corrosion, concrete cracking and fatigue.

The approach used to model chloride ingress including the effects of the surrounding environment is presented in section 3.2. Section 3.3 describes the proposed approach to account for the interaction between reinforcement corrosion and concrete cracking. Section 3.4 depicts the entire coupled model.

3.2 Model of time to corrosion initiation

A comprehensive model of time to corrosion initiation should consider the coupled effect of the following phenomena:

- the chloride binding capacity of the cementitious system;
- the decrease of the chloride diffusivity with concrete age;
- the one- and two-dimensional flow of chlorides in unsaturated concrete; and

- the time-variant nature and the effects of temperature, humidity and chloride concentration in the surrounding environment.

The interaction between these phenomena is rarely considered within a simplified solution based on Fick's law –i.e., equations 2.2 or 2.3, which are only valid for saturated flow. This study implements a numerical solution to the governing equations of chloride penetration which accounts for the above mentioned phenomena.

3.2.1 Chloride flow in unsaturated conditions

The governing equations of chloride ingress consider the interaction between three phenomena (Saetta et al., 1993; Ababneh et al., 2003):

1. chloride transport;
2. moisture diffusion; and
3. heat transfer.

This section focuses on the description of each phenomenon separately. Since each phenomenon is defined by a partial differential equation (PDE), a numerical procedure is implemented to solve the nonlinear set of PDEs. It combines finite element and finite difference methods (section 3.2.2).

3.2.1.1 Chloride transport

Chloride ingress results from a complex interaction between physical and chemical processes. However, under various assumptions, this phenomenon can be simplified to a diffusion problem. Tuutti (1982) proposed modeling chloride penetration in concrete as function of time and depth using Fick's second law of diffusion:

$$\frac{\partial C_{tc}}{\partial t} = \text{div} \left(D_c w_e \vec{\nabla} (C_{fc}) \right) \quad (3.1)$$

where C_{tc} is the total chloride concentration, t is the time, D_c is the effective chloride diffusion coefficient, w_e is the evaporable water content and C_{fc} is the concentration of chlorides dissolved in the pore solution –i.e., free chlorides. Equation 3.1 represents the change of the total chloride concentration as a function of the spatial gradient of free chlorides. The relationship between total and free chloride concentrations is estimated as:

$$C_{tc} = C_{bc} + w_e C_{fc} \quad (3.2)$$

where C_{bc} is the concentration of bound chlorides, i.e., chlorides chemically bound to the hydration products of the cement or physically sorbed on the surfaces of the gel pores (Neville, 1995). Binding isotherms relate free and bound chloride concentrations at equilibrium and are characteristic of each cementitious system. According to Tang and Nilsson (1993) and Glass and Buenfeld (2000), two

common isotherms used to estimate the chloride binding capacity are (1) *Langmuir isotherm*:

$$C_{bc}^L = \frac{\alpha_L C_{fc}}{1 + \beta_L C_{fc}} \quad (3.3)$$

and (2) *Freundlich isotherm*:

$$C_{bc}^F = \alpha_F C_{fc}^{\beta_F} \quad (3.4)$$

where α_L , β_L , α_F and β_F are binding constants obtained empirically from regression analyses. The values of the binding constants depend on the content of tricalcium aluminate C_3A , which affects the binding capacity of the cement. For instance, for a medium content of 8% of C_3A the coefficients for the Langmuir isotherm are $\alpha_L = 0.1185$ and $\beta_L = 0.090$ (Glass and Buenfeld, 2000). For the Freundlich isotherm, Han (2007) computed the constants as functions of the content of tricalcium aluminate of cement as: $\alpha_F = 0.056 + 0.025C_3A$ and $\beta_F = 1/(1.91 + 0.076C_3A)$.

Frequently, diffusion is considered the main transport process of chlorides into concrete. However, under partially-saturated conditions the chloride ingress by capillary sorption or convection becomes an important mechanism. The chloride ingress process is a combination of diffusion and convection. Diffusion denotes the net motion of a substance from an area of high concentration to an area of low concentration. Convection refers to the movement of molecules (e.g., chlorides) within fluids (e.g., water). To account for both mechanisms, a convective term is added to Fick's second law of diffusion (Martín-Pérez et al., 2001):

$$\frac{\partial C_{tc}}{\partial t} = \underbrace{\text{div} \left(D_c w_e \vec{\nabla} (C_{fc}) \right)}_{\text{diffusion}} + \underbrace{\text{div} \left(D_h w_e C_{fc} \vec{\nabla} (h) \right)}_{\text{convection}} \quad (3.5)$$

where D_h is the effective humidity diffusion coefficient and h is the relative humidity. Thus, equation 3.5 can be rewritten in terms of the concentration of free chlorides. For instance, for a bi-dimensional flow of chlorides into x and y directions, equation 3.5 becomes:

$$\frac{\partial C_{fc}}{\partial t} = D_c^* \left(\frac{\partial^2 C_{fc}}{\partial x^2} + \frac{\partial^2 C_{fc}}{\partial y^2} \right) + D_h^* \left[\frac{\partial}{\partial x} \left(C_{fc} \frac{\partial h}{\partial x} \right) + \frac{\partial}{\partial y} \left(C_{fc} \frac{\partial h}{\partial y} \right) \right] \quad (3.6)$$

where D_c^* and D_h^* represent the apparent chloride and humidity diffusion coefficients, respectively:

$$D_c^* = \frac{D_c}{1 + (1/w_e) (\partial C_{bc} / \partial C_{fc})} \quad (3.7)$$

$$D_h^* = \frac{D_h}{1 + (1/w_e) (\partial C_{bc} / \partial C_{fc})} \quad (3.8)$$

where $\partial C_{bc} / \partial C_{fc}$ is the binding capacity of the cementitious system which is given by the slope of the binding isotherm (Nilsson et al., 1994).

On the other hand, experimental evidence has shown that the effective chloride diffusion coefficient

depends mainly on temperature, pore relative humidity, concrete aging, cement type, porosity and curing conditions (Saetta et al., 1993). The effects of temperature, humidity and concrete aging can be estimated by correcting a reference diffusion coefficient, $D_{c,ref}$, which has been measured at standard conditions (Saetta et al., 1993; Martín-Pérez et al., 2001):

$$D_c = D_{c,ref} f_1(T) f_2(t) f_3(h) \quad (3.9)$$

where $f_1(T)$, $f_2(t)$ and $f_3(h)$ are correction expressions for temperature, aging and humidity, respectively.

The correction function for the temperature is:

$$f_1(T) = \exp \left[\frac{U_c}{R} \left(\frac{1}{T_{ref}} - \frac{1}{T} \right) \right] \quad (3.10)$$

where U_c is the activation energy of the chloride diffusion process in kJ/mol, R is the gas constant ($R = 8.314 \text{ J}/(\text{mol} \cdot \text{K})$), T_{ref} is the reference temperature at which the reference diffusion coefficient, $D_{c,ref}$, has been evaluated ($T_{ref} = 296 \text{ K}$) and T is the actual absolute temperature in the concrete in °K. Typical values of U_c range between 32 and 44.6 kJ/mol for ordinary Portland cements (Page et al., 1981). The influence of temperature is shown in Figure 3.1a for the parameter values mentioned. It can be observed that for temperatures lower than T_{ref} chloride diffusivity is reduced. For higher values of the activation energy of the chloride diffusion process, $D_{c,ref}$ becomes more sensitive to temperature changes. In other words, for $T > T_{ref}$ the marginal increment in temperature has more influence on $D_{c,ref}$ when U_c increases.

The correction function for aging is defined as:

$$f_2(t) = \left(\frac{t_{ref}}{t} \right)^{m_c} \quad (3.11)$$

where t_{ref} is the time of exposure at which $D_{c,ref}$ has been evaluated, t is the actual time of exposure in days and m_c is the age reduction factor. Val (2006) reported that this factor varies between 0 and 1. The relationship between $D_{c,ref}$ and f_2 for various m_c is depicted in Figure 3.1b. It can be noted that the decay of chloride diffusivity with time is slow for lower values of m_c .

The correction function for humidity is:

$$f_3(h) = \left[1 + \frac{(1-h)^4}{(1-h_c)^4} \right]^{-1} \quad (3.12)$$

where h_c is the humidity at which D_c drops halfway between its maximum and minimum values (i.e., $h_c = 0.75$ (Bažant and Najjar, 1971)) and h is the actual pore relative humidity. Figure 3.1c depicts the effect of f_3 on the chloride diffusion coefficient. Since chloride diffusion depends on the amount of water in the capillary pores, the chloride diffusion coefficient is reduced for humidities lower than h_c (Bažant and Najjar, 1971).

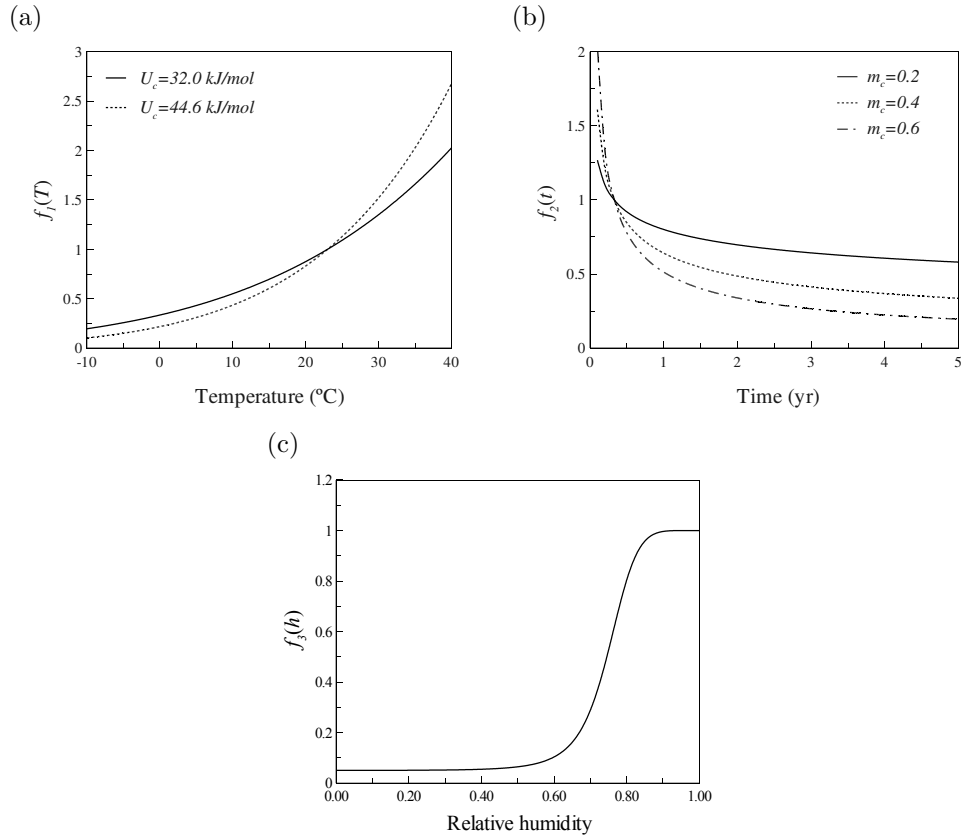


Figure 3.1: Dependence of D_c on (a) temperature; (b) age for $t_{ref} = 120$ days; and (c) humidity for $h_c = 0.75$.

3.2.1.2 Moisture diffusion

Moisture flow in concrete is also modeled by Fick's law and can be expressed in terms of the pore relative humidity, h , as follows (Bažant and Najjar, 1972):

$$\frac{\partial w_e}{\partial t} = \frac{\partial w_e}{\partial h} \frac{\partial h}{\partial t} = \text{div} \left(D_h \vec{\nabla} (h) \right) \quad (3.13)$$

As well as the chloride diffusion coefficient, the humidity diffusion coefficient depends on many factors and can be estimated in terms of a reference humidity diffusion coefficient, $D_{h,ref}$ (Saetta et al., 1993):

$$D_h = D_{h,ref} g_1(h) g_2(T) g_3(t_e) \quad (3.14)$$

The function $g_1(h)$ takes into consideration the dependence on the pore relative humidity of the concrete:

$$g_1(h) = \alpha_0 + \frac{1 - \alpha_0}{1 + [(1 - h)/(1 - h_c)]^n} \quad (3.15)$$

where α_0 is a parameter that represents the ratio of $D_{h,min}/D_{h,max}$, h_c is the value of pore relative humidity at which D_h drops halfway between its maximum and minimum values ($h_c = 0.75$) and n is a parameter that characterizes the spread of the drop in D_h . Bažant and Najjar (1971, 1972) found that the ranges for α_0 and n are $[0.025, 0.1]$ and $[6, 16]$, respectively. Figure 3.2a illustrates the influence of these parameters. It is noted that g_1 tends to α_0 for lower relative humidities. The parameter n controls the transition between $g_1 = \alpha_0$ and $g_1 = 1$; this transition is sudden for high values of n .

The correction function $g_2(T)$ accounts for the influence of temperature on D_h :

$$g_2(T) = \exp \left[\frac{U}{R} \left(\frac{1}{T_{ref}} - \frac{1}{T} \right) \right] \quad (3.16)$$

where U is the activation energy of the moisture diffusion process in kJ/mol and T_{ref} is the reference temperature at which $D_{h,ref}$ was measured ($T_{ref} = 276^\circ\text{K}$). Bažant and Thonguthai (1978) and Saetta et al. (1993) found that U ranges between 22.5 and 39 kJ/mol. The influence of temperature on D_c is presented in Figure 3.2b. As for equation 3.10, for higher values of the activation energy of the chloride diffusion process, $D_{c,ref}$ becomes more sensitive to temperature changes.

Finally, $g_3(t_e)$ considers the dependency on the degree of hydration attained in concrete:

$$g_3(t_e) = 0.3 + \sqrt{\frac{13}{t_e}} \quad (3.17)$$

where t_e represents the equivalent hydration (curing) period in days. Figure 3.2c describes the influence of t_e on chloride diffusivity. Note that for $t_e < 28$ days the correction factor g_3 increases the chloride diffusion coefficient while for $t_e > 28$ days it tends to be constant.

The moisture capacity of concrete $\partial w_e / \partial h$ should also be determined to solve equation 3.13. For constant temperature, the amount of free water, w_e , and pore relative humidity, h , are related by adsorption isotherms. According to the Brunauer-Skalny-Bodor (BSB) model, the adsorption isotherm can be estimated as (Brunauer et al., 1969):

$$w_e = \frac{CkV_m h}{(1 - kh)[1 + (C - 1)kh]} \quad (3.18)$$

where the parameters C , k and V_m are parameters depending on temperature, water/cement ratio, w/c , and the degree of hydration attained in the concrete t_e . Xi et al. (1994) developed experimental expressions for such parameters; for $t_e \geq 5$ days and $0.3 < w/c \leq 0.7$:

$$C = \exp \left(\frac{855}{T} \right) \quad (3.19)$$

$$k = \frac{(1 - 1/n_w)C - 1}{C - 1} \quad (3.20)$$

$$n_w = \left(2.5 + \frac{15}{t_e} \right) (0.33 + 2.2w/c) N_{ct} \quad (3.21)$$

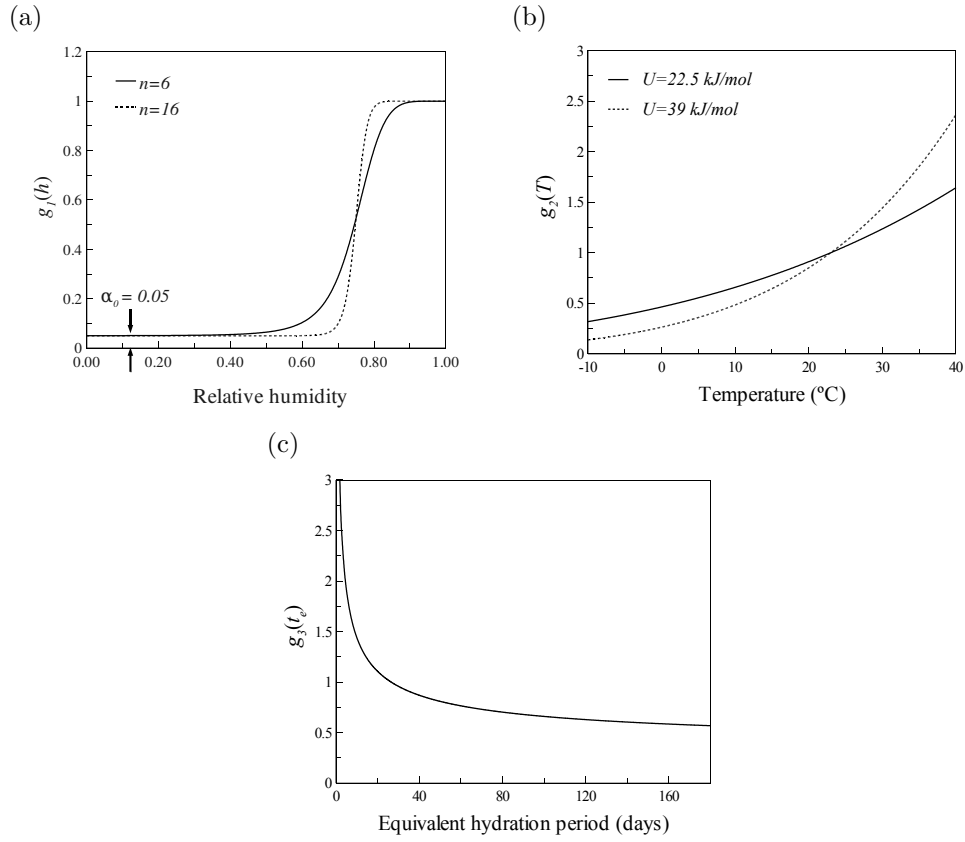


Figure 3.2: Dependence of D_h on (a) humidity for $h_c = 0.75$ and $\alpha_0 = 0.05$; (b) temperature; and (c) equivalent hydration period.

$$V_m = \left(0.068 - \frac{0.22}{t_e} \right) (0.85 + 0.45w/c) V_{ct} \quad (3.22)$$

where N_{ct} and V_{ct} depend on the type of cement; e.g. for ordinary Portland cement $N_{ct} = V_{ct} = 1$. The implemented model of moisture diffusion can be used to consider several weather conditions such as drying and wetting cycles or rain. These conditions are simulated by assuming that the exposed boundaries are saturated or unsaturated.

3.2.1.3 Heat transfer

Heat flow throughout concrete is determined by applying the energy conservation requirement to Fourier's heat conduction law (Bažant and Najjar, 1972):

$$\rho_c c_q \frac{\partial T}{\partial t} = \text{div} \left(\lambda \vec{\nabla} (T) \right) \quad (3.23)$$

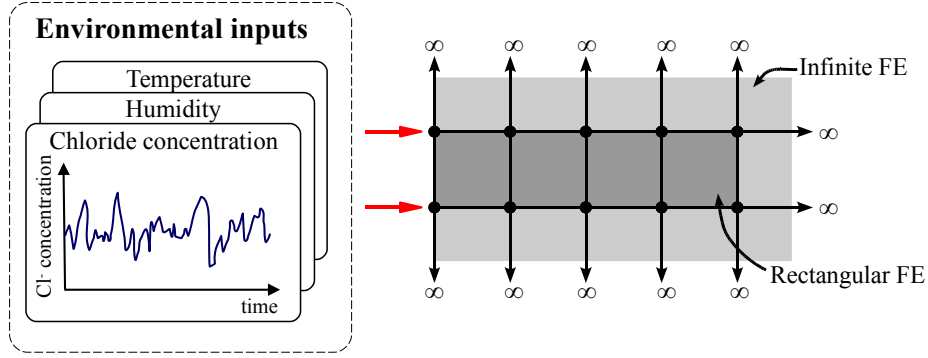


Figure 3.3: FE mesh in one dimension.

where ρ_c is the density of the concrete, c_q is the concrete specific heat capacity, λ is the thermal conductivity of concrete and T is the temperature inside the concrete matrix after time t . According to Neville (1981), the specific heat capacity for ordinary concrete ranges from 840 to 170 J/(kg °C). The thermal conductivity of concrete can be affected by variations in temperature and humidity. However, Bažant and Thonguthai (1978) reported that these variations are small and that λ can be assumed constant. The common range of values for thermal conductivity of concrete varies between 1.4 and 3.6 W/(m °C) (Neville, 1981). Although sun radiation can affect the temperature inside concrete, this study does not account for this effect.

3.2.2 Numerical solution of the governing equations

In order to study the evolution of chloride ingress into concrete, it is necessary to simultaneously solve the system of PDEs represented by equations 3.5, 3.13 and 3.23. The variation of the concentration of free chlorides, C_{fc} , humidity, h and temperature, T throughout space for a given time t is computed by using the finite element method. The evolution of spatial distribution is integrated in time by using the Crank-Nicolson method which is based on finite differences. The methodology developed by Martín-Pérez et al. (2001) to solve the system of PDEs is implemented in this study in Fortran 95. Such methodology uses linear rectangular elements and bilinear singly and doubly infinite elements to mesh the domain –i.e., Figure 3.3. Infinite elements are used to simulate the existence of material beyond the unexposed boundaries.

Fluxes of chlorides, relative humidity or heat crossing the surface define the conditions at the exposed boundaries (Robin boundary condition, Figure 3.3). The chloride flux normal to the concrete surface, J_c^s , is:

$$J_c^s = \underbrace{B_c (C_{fc}^s - C_{env})}_{\text{diffusion}} + \underbrace{C_{env} J_h^s}_{\text{convection}} \quad (3.24)$$

where B_c is the surface chloride transfer coefficient, C_{fc}^s is the concentration of free chlorides at the concrete surface, C_{env} is the concentration of chlorides in the surrounding environment and J_h^s is the

humidity flux normal to the concrete surface which is defined by:

$$J_h^s = B_h (h^s - h_{env}) \quad (3.25)$$

where B_h is the surface humidity transfer coefficient, h^s is the pore relative humidity at the concrete surface and h_{env} is the relative humidity in the environment. For heat transfer, the boundary condition is given by the heat flux across the concrete surface, q^s :

$$q^s = B_T (T^s - T_{env}) \quad (3.26)$$

where B_T is the heat transfer coefficient, T^s is the temperature at the concrete surface and T_{env} is the temperature in the surrounding environment. By fitting experimental data, Saetta et al. (1993) reported that B_c varies between 1 and 6 m/s. Typical values of B_h are in the range of $2.43 - 4.17 \times 10^{-7}$ m/s (Akita et al., 1997). Finally, Khan et al. (1998) observed that B_T fluctuates between 6.2 and 9.3 W/(m²°C).

Figure 3.4 depicts the algorithm used to determine the time-dependent variation of the profiles of temperature, humidity and chlorides for one dimension –e.g., x . In the first iteration ($i = 1$), the initial values of temperature, humidity and concentration of free chlorides can be supposed constant in all points inside the mesh –e.g. T_{ini} , h_{ini} and $C_{fc,ini}$. Commonly the concentration of free chlorides is set at zero at the beginning of the assessment. However, a given profile of chlorides can be used for existing structures. The algorithm to determine the profiles for a given time t_i can be summarized as follows:

1. the actual temperature profile is determined from equation 3.23 by considering the initial temperature profile $T(x; t = t_{i-1})$;
2. with the temperature profile estimated in the previous step $T(x; t = t_i)$ and the initial humidity profile $h(x; t = t_{i-1})$, the actual humidity profile is determined from equation 3.13; and finally;
3. equation 3.5 is solved by accounting for the actual profiles of temperature and humidity throughout the concrete and the initial values of free chlorides $C_{fc}(x; t = t_{i-1})$.

The procedure is repeated for the next step ($t_i = t_{i-1} + \Delta t$) by considering the previous profiles as initial values. The major difficulty in estimating the profiles of humidity and chlorides lies in the fact that equations 3.5 and 3.13 are nonlinear because the diffusion coefficients and the isotherms depend on the actual profiles of humidity and chlorides; therefore, an iterative procedure is implemented. This procedure uses the profiles of h and C_{fc} obtained from the previous iteration, as the initial values and iterates until a given convergence criterion is reached. For example, for the profile of humidity in one dimension (i.e., x), the convergence criterion considered is:

$$\left| \frac{h(x; t_i)^{k+1} - h(x; t_i)^k}{h(x; t_i)^k} \right| \leq \varepsilon \quad (3.27)$$

where k represents the iterations to find $h(x; t_i)$, $h(x; t_i)^k$ is the humidity profile for the previous iteration, $h(x; t_i)^{k+1}$ is the humidity profile for the actual iteration and ε denotes a specified convergence

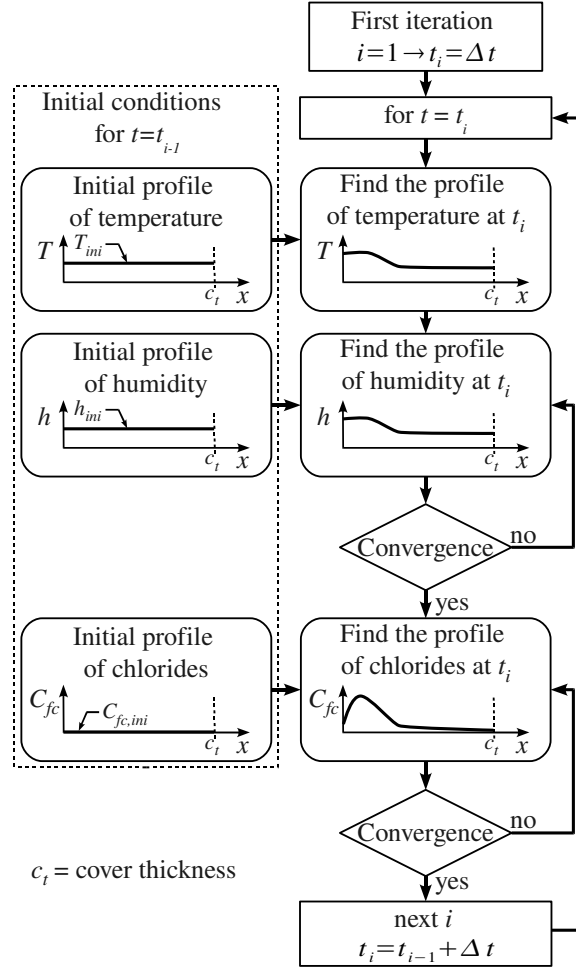


Figure 3.4: Algorithm for estimating the profiles of temperature, humidity and chlorides.

parameter. A successive under-relaxation method is also implemented to increase the convergence rate. This method estimates a new humidity profile, $h^*(x; t_i)^{k+1}$, that is used as initial value for the next iteration:

$$h^*(x; t_i)^{k+1} = \omega h(x; t_i)^{k+1} + (1 - \omega) h(x; t_i)^k \quad (3.28)$$

where ω is the relaxation factor chosen in the range $[0, 1]$.

3.2.3 Model verification

There are various commercial programs to model diffusion/convection problems (e.g., ANSYS, Abaqus, etc.). However a computer code was developed to:

- solve the non-linear PDEs –i.e., equations 3.5 and 3.13;
- implement Robin boundary conditions –i.e., equations 3.24, 3.25 and 3.26;

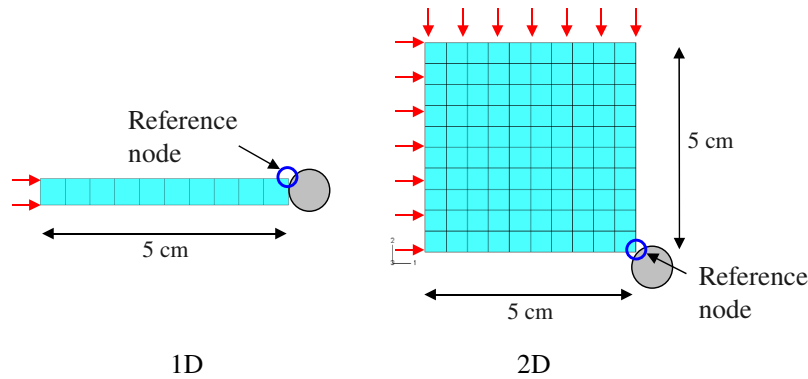


Figure 3.5: Configuration of the calibration models.

- use time-variant and stochastic inputs for environmental humidity, temperature, and chloride concentration; and
- consider the uncertainties involved in the problem.

This section presents a comparative study of the results obtained with: (1) the code developed, (2) commercial software (Abaqus) and (3) the analytical solution to the problem. The objective of this comparison is to validate the results.

Taking into account the limitations of both Abaqus and the analytical solution, the following assumptions were made:

- the effective chloride diffusion coefficient is defined as constant: $D_c = 10^{-12} \text{ m}^2/\text{s}$;
- the chloride surface concentration is also constant: $C_s = 17 \text{ kg}/\text{m}^3$; and
- the chloride flow in one and two dimensions.

Figure 3.5 depicts the configuration of the cases studied. The results of this analysis will focus on the reference node located at a depth of 5 cm. Figure 3.6 shows the chloride concentration at the reference node for one- and two-dimensional flow of chlorides. It should be noted in both cases that the solution found by Abaqus and the methodology used herein are very close. Accuracy is improved (close to the solution of Abaqus) when the time step is reduced from $\Delta t = 30$ to $\Delta t = 10$ days (Figure 3.6a). However, it can also be observed that there is a significant difference between the numerical solutions (implemented methodology and Abaqus) and the analytical solution. Given that the analytical solution remains valid in this example, it can be concluded that the numerical solution overestimates the assessment. This behavior is explained by the fact that the numerical solutions does not consider that there is material beyond the unexposed boundaries. This condition can be taken into account by adding infinite elements in such boundaries. Thus, Figure 3.7 presents a comparison between the analytical solution and the improved numerical solution. It is noteworthy that both solutions are closer to the analytical solution.

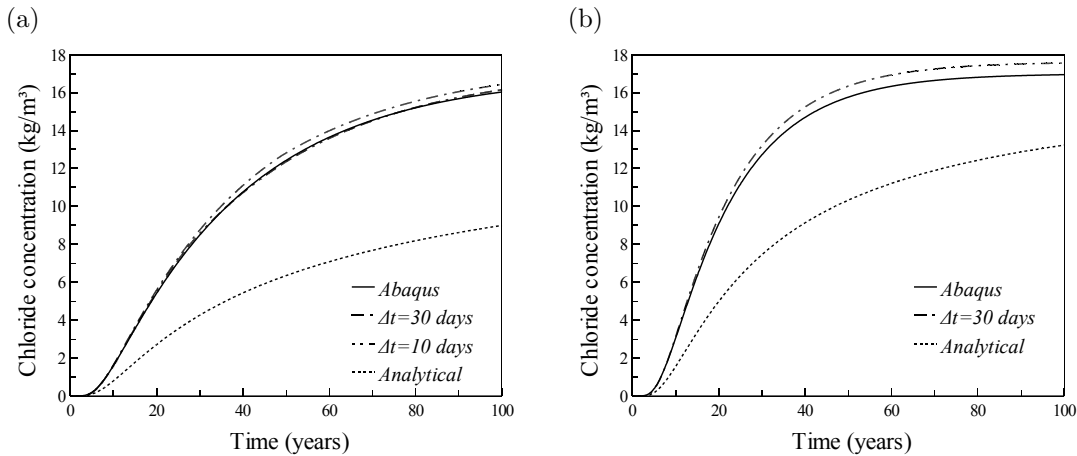


Figure 3.6: Chloride concentration at the reference node: (a) 1D case, and (b) 2D case.

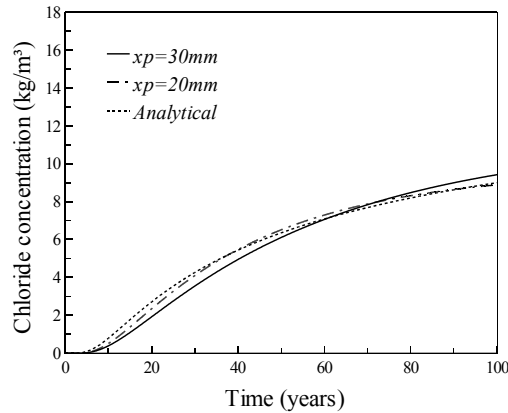


Figure 3.7: Use of infinite elements to improve the numerical solution.

3.3 Interaction between corrosion and concrete cracking

When corrosion begins, the accumulation of rust products at the corrosion cell induces expansive stresses causing concrete cracking and spalling. The kinematics of rust production is controlled by the corrosion rate, which is influenced mainly by the pH of the concrete and the availability of water and oxygen at the corrosion cell. The influence of concrete cracking on corrosion rate is not easy to evaluate. Whereas Liang et al. (2005) considered that corrosion rate is *constant* after corrosion of the total surface area of the bar, Vu and Stewart (2000) stated that i_{corr} has a *time-variant* behavior which decreases because of the accumulation of rust products.

This section presents a proposal which takes into account the interaction between reinforcement corrosion and concrete cracking derived from the model of Liang et al. (2005). On the basis of the experimental measurements carried out by Schiessl and Raupach (1997), the proposed approach assumes that corrosion rate increases when crack width reaches a limit value.

3.3.1 Model of corrosion rate

The corrosion of reinforcement is controlled by a well-known electrochemical process. The corrosion rate can be quantified in terms of a corrosion current density, i_{corr} . This parameter measures general or uniform loss of metal and relates corrosion current with a reduction of the cross-section of the metal. For instance, a corrosion rate of $i_{corr} = 1 \mu\text{A}/\text{cm}^2$ corresponds to a section loss of $11.6 \mu\text{m}/\text{yr}$ (Jones, 1992). The corrosion rate depends mainly on the electrical conductivity of concrete and the availability of oxygen and water at the corrosion cell. However, there is no model coupling the interaction between these parameters. Whereas for high humidity the oxygen availability controls the corrosion rate, for low humidity it is governed by the electrical resistivity of concrete (Vu and Stewart, 2000). This subsection presents two models of corrosion rate.

The corrosion density $i_{corr}(t)$ at time t is expressed according to Faraday's law as:

$$i_{corr}(t) = J_c(t)n_{\text{O}_2}F \quad (3.29)$$

where, n_{O_2} is the obtained electric number of O_2 molecule participating in the chemical reaction ($n_{\text{O}_2} = 4$), $J_c(t)$ is the diffusion flow of O_2 in concrete at time t and F is Faraday's constant, $F = 96500 \text{ C/mol}$. On the other hand the diffusion flow of O_2 in concrete is equal to (Liang et al., 2005):

$$J_c(t) = D_{\text{O}_2} \frac{\partial C(x)}{\partial x} \quad (3.30)$$

where D_{O_2} is the diffusion coefficient of O_2 in the concrete and x is the space coordinate in the diffusion direction. According to Fick's diffusion law there is a linear variation of the oxygen concentration. Therefore, if the oxygen concentration on the surface is $C_{\text{O}_2} = 8.93 \times 10^{-10} \text{ mol}/\text{mm}^3$ and at the depth $L_{th}(t)$ the concentration is $C_{st} = 0$, the variation of the oxygen concentration can be computed as (Liang and Yang, 2004):

$$\frac{\partial C(x)}{\partial x} = \frac{C_{\text{O}_2} - C_{st}}{L_{th}(t)} \quad (3.31)$$

where $L_{th}(t)$ is the penetration depth of chloride threshold aggressive front which represents the depth of threshold concentration C_{th} at time t . Niu et al. (1996) proposed an equation for calculating the diffusion coefficient of oxygen D_{O_2} as a function of the concrete compressive strength f'_{cu} in N/mm^2 as:

$$D_{\text{O}_2} = 3.1536 \times 10^5 \left(\frac{32.15}{f'_{cu}} - 0.44 \right) \left[\frac{\text{mm}^2}{\text{year}} \right] \quad (3.32)$$

where f'_{cu} is obtained from tests over concrete cube samples. By replacing equations 3.30 and 3.31 into equation 3.29, the corrosion rate yields to (Liang et al., 2005):

$$i_{corr}(t) = \frac{n_{\text{O}_2} F D_{\text{O}_2} C_{\text{O}_2}}{L_{th}(t)} \quad (3.33)$$

This model combines diffusion and electrochemical principles to take into consideration the influence of the availability of oxygen on the corrosion rate. However, both the availability of water and the

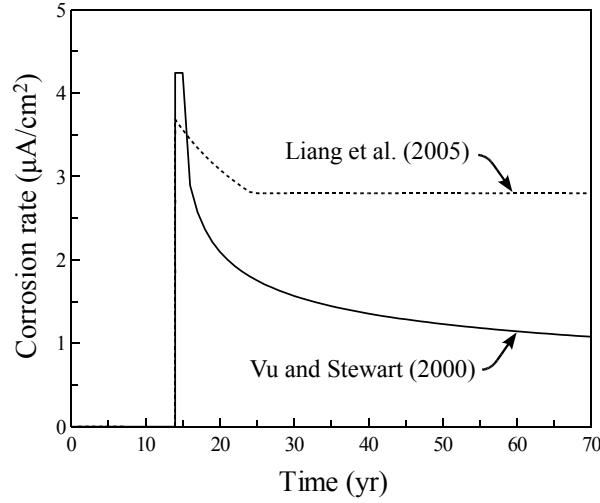


Figure 3.8: Corrosion rate models.

interaction with concrete cracking are not considered.

Vu and Stewart (2000) proposed an empirical relationship where the corrosion rate (in $\mu\text{A}/\text{cm}^2$) is a function of the cover thickness, c_t , and the water/cement ratio, w/c :

$$i_{corr}(t) = \begin{cases} \frac{37.8(1-w/c)^{-1.64}}{c_t} & \text{for } t_{ini} + 1 \text{ year} \geq t > t_{ini} \\ \frac{32.13(1-w/c)^{-1.64}}{c_t} (t - t_{ini})^{-0.3} & \text{for } t > t_{ini} + 1 \text{ year} \end{cases} \quad (3.34)$$

where the cover is given in mm. Equation 3.34 is valid when the structure is located in an environment with relative humidity of 75% and temperature of 20°. This model assumes that the corrosion rate remains constant during one year and i_{corr} decreases due to the formation of corrosion products at the corrosion cell, reducing the diffusion of the iron ions away from the steel surface. The corrosion rate computed by equation 3.34 has been determined based on experimental measures and considers the influence of w/c ratio. Nevertheless, the predicted values are only valid for structures under determined environmental conditions and do not consider either concrete cracking nor availability of oxygen and water at the corrosion cell.

Figure 3.8 presents a comparison of the corrosion rates estimated for each model (equations 3.33 and 3.34). Note that when corrosion begins ($t = 14$ years), both models tend towards a similar corrosion rate ranging between 3.7 and 4.3 $\mu\text{A}/\text{cm}^2$. Afterwards, although the kinematics of the corrosion rate is similar for both models, it stabilizes at different values. Both models are suitable to model i_{corr} in structures without cracks. However they do not consider the increase of the corrosion rate that has been measured experimentally after excessive concrete cracking appears (Schiessl and Raupach, 1997).

3.3.2 Concrete cracking

The volume of rust products is about 4 to 6 times higher than the volume of iron (Figure 3.9). Therefore the formation of corrosion products at the steel/concrete interface will lead to cracking and spalling

of concrete cover. This section describes the models used to estimate the length of this stage which is divided into two sub-stages called time to *crack initiation* and time to *severe cracking*.

3.3.2.1 Time to crack initiation

Once corrosion starts there are stresses resulting from the accumulation of corrosion products at the corrosion cell. In order to take into account this effect, Liu and Weyers (1998) proposed a model to find the time to crack initiation, t_{cr} , as a function of the amount of rust products, W . The amount of corrosion products at time t can be estimated as a function of both the density of the rust ρ_{rust} and the remaining area of steel as follows:

$$W(t) = \begin{cases} \rho_{rust} \left(\pi \frac{d_0^2}{4} - A_u^{st}(t) \right) & \text{for uniform corrosion} \\ \rho_{rust} \left(\pi \frac{d_0^2}{4} - A_p^{st}(t) \right) & \text{for pitting corrosion} \end{cases} \quad (3.35)$$

where d_0 is the initial diameter of the reinforcing bar and $A_u^{st}(t)$ and $A_p^{st}(t)$ are respectively the remaining areas of steel for uniform and pitting corrosion –i.e. equations 2.12 and 2.20. Liu and Weyers (1998) defined the amount of critical rust products W_{crit} as the amount for which all free spaces between the steel bar and the concrete are filled and concrete cracking begins. It can be calculated as:

$$W_{crit} = \frac{\rho_{steel}}{\rho_{steel} - 0.57\rho_{rust}} (W_{porous} + W_{expand}) \quad (3.36)$$

where ρ_{steel} is the density of reinforcing steel, W_{porous} is the amount of corrosion products necessary to fill the porous zone around the steel/concrete interface defined as:

$$W_{porous} = \pi\rho_{rust}\tau_{por}d_0 \quad (3.37)$$

where τ_{por} is the thickness of porous band around the steel concrete interface. W_{expand} is the amount of corrosion products needed to fill in the space due to the expansion of the concrete around the reinforcement; this is:

$$W_{expand} = \pi\rho_{rust}(d_0 + 2\tau_{por})\tau_{crit} \quad (3.38)$$

where τ_{crit} is the thickness of corrosion products needed to generate the tensile stresses (Liu and Weyers, 1998) and is computed as:

$$\tau_{crit} = \frac{c_t f_{ct}}{E_c} \left(\frac{k_{cr}^2 + l_{cr}^2}{l_{cr}^2 - k_{cr}^2} + \nu_c \right) \quad (3.39)$$

where f_{ct} is the tensile strength of concrete, E_c is the elastic modulus of concrete, c_t is the cover thickness, $k_{cr} = (d_0 + 2\tau_{por})/2$, $l_{cr} = c_t + (d_0 + 2\tau_{por})/2$ and ν_c is Poisson's ratio of concrete.

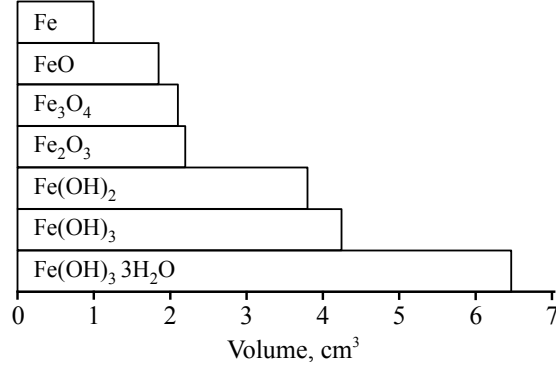


Figure 3.9: Volume of corrosion products (adapted from Nielsen (1985)).

3.3.2.2 Time to severe cracking

The time to crack initiation ends when a hairline crack of about 0.05 mm appears. Nonetheless, the stresses resulting from the accumulation of corrosion products increase the size of concrete cracks until a critical size, after which the serviceability or safety of the structure could be affected. According to Vu and Stewart (2005) and Vu et al. (2005), the time to severe cracking, t_{sp} , is equal to:

$$t_{sp} = t_{cr} + t_{pr} \quad (3.40)$$

where t_{cr} is the time to crack initiation (estimated from the Liu and Weyers model) and t_{pr} is the time to crack propagation (Figure 3.10). Based on experimental data obtained from accelerated corrosion tests with a corrosion rate of $i_{corr(acc)} = 100 \mu\text{A}/\text{cm}^2$, Vu et al. (2005) found that the accelerated time to crack propagation in hours can be estimated as:

$$t_{pr(acc)} = p_1 \left(\frac{c_t}{w/c} \right)^{p_2} \quad (3.41)$$

where p_1 and p_2 are parameters that depend on the limit crack width c_{wlim} . For instance, Table 3.1 presents the values of these parameters for various crack widths (Vu et al., 2005). Since equation 3.41 was obtained from accelerated tests, a correction factor, k_R , has been deduced by Vu et al. (2005), based on the experimental values obtained by Alonso et al. (1998) as:

$$k_R \approx 0.95 \left[\exp \left(-\frac{0.3i_{corr(acc)}}{i_{corr}} \right) - \frac{i_{corr(acc)}}{2500i_{corr}} + 0.3 \right] \quad (3.42)$$

where i_{corr} corresponds to the real corrosion rate in $\mu\text{A}/\text{cm}^2$ –i.e., equations 3.33 or 3.34. Thus, the time to crack propagation in years can be estimated as:

$$t_{pr} = k_R \frac{0.0114}{i_{corr}} t_{pr(acc)} \quad (3.43)$$

Table 3.1: Parameters for equation 3.41 (Vu et al., 2005).

Limit crack width	p_1	p_2
$c_{w_{lim}} = 0.1\text{mm}$	65	0.45
$c_{w_{lim}} = 0.5\text{mm}$	225	0.29
$c_{w_{lim}} = 1.0\text{mm}$	700	0.23

3.3.3 Coupling between concrete cracking and corrosion rate

When severe cracking begins (i.e., $t > t_{sp}$), it is assumed that the diffusion coefficient of the oxygen D_{O_2} varies linearly. Consider that at time t_n (with $t_n \gg t_{sp}$; e.g. $t_n = 500$ years) the oxygen concentration at the steel surface (i.e., C_{nO_2}) is closer to the oxygen concentration at the concrete surface C_{O_2} (i.e., $C_{nO_2} \approx C_{O_2}$). Then substituting these values into Fick's second law, it is possible to compute a new oxygen diffusion coefficient at time t_n , as:

$$D_{nO_2} = \frac{c_t^2}{4t_n \left[\text{erf}^{-1} \left(1 - \frac{C_{nO_2}}{C_{O_2}} \right) \right]^2} \quad (3.44)$$

where c_t is the cover thickness. The modified diffusion coefficient of oxygen in the concrete (D_{mO_2}) at time t becomes (Figure 3.10a):

$$D_{mO_2}(t) = \begin{cases} D_{O_2} & \text{for } t \leq t_{sp} \\ D_{O_2} + \frac{D_{O_2} - D_{nO_2}}{t_{sp} - t_n} (t - t_{sp}) & \text{for } t > t_{sp} \end{cases} \quad (3.45)$$

then, substituting equation 3.45 into 3.33, the corrosion rate when considering the RC cracked, i_{corr}^{lin} , is given by:

$$i_{corr}^{lin}(t) = \begin{cases} 0 & \text{for } t_{ini} \geq t \\ \frac{n_{O_2} F D_{mO_2}(t) C_{O_2}}{L_{th}(t)} & \text{otherwise} \end{cases} \quad (3.46)$$

where n_{O_2} is the electric number of O_2 molecule that participates in the chemical reaction; F is Faraday's constant and $L_{th}(t)$ is the penetration depth of chloride threshold aggressive front.

Figure 3.10b compares the corrosion rate computed with the linear variation approach (equation 3.46) and the corrosion rates estimated from the model of Liang et al. (2005) and Vu et al. (2005) (equations 3.33 and 3.34, respectively). The linear variation model includes concrete cracking and assumes that the change of the oxygen diffusion coefficient begins after the time to severe cracking t_{sc} defined as the time at which the crack width reaches a critical value of $c_{w_{lim}} = 0.5$ mm. It is important to note that the corrosion rates predicted with the proposed approach are within the range suggested by EN206 (Geocisa and the Torroja Institute, 2002).

3.4 Proposed model of corrosion, concrete cracking and fatigue

The corrosion-fatigue damage process in RC structures is shown in Figure 3.11. The process takes into account the interaction between:

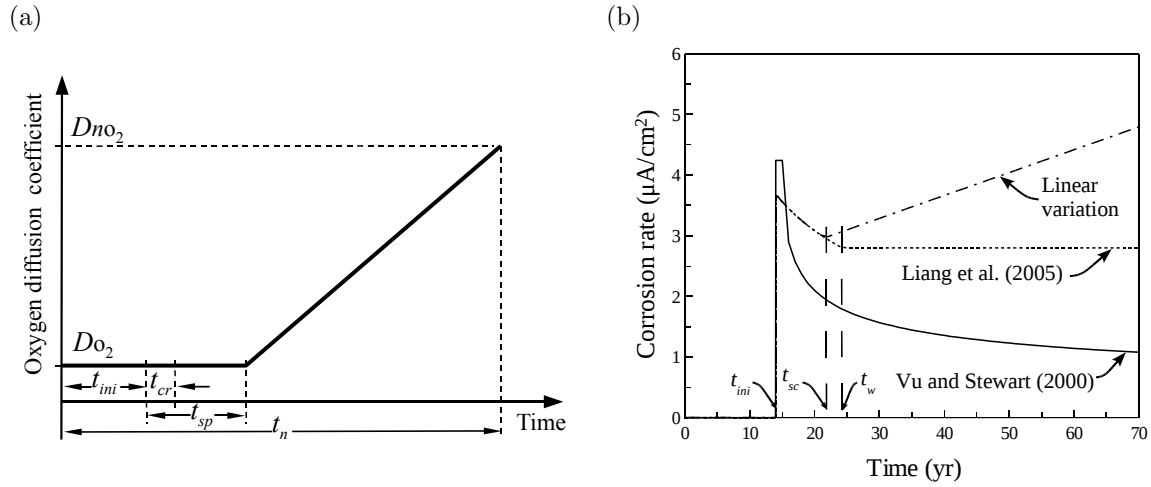


Figure 3.10: (a) Variation of the diffusion oxygen coefficient with time. (b) Time-variant corrosion rate models.

1. chloride ingress,
2. concrete cracking and
3. cyclic loading.

Chloride ingress leads to steel depassivation, and takes part in the kinematics of the corrosion process. The corrosion resulting from chloride ingress induces high localized corrosion (i.e. pitting corrosion), leading to reinforcing steel crack nucleation (Kondo, 1989; Ahn et al., 1992; Chen and Duquette, 1992). Concrete cracking caused by the accumulation of corrosion products in the steel/concrete interface influences the steel corrosion rate. On the other hand, cyclic loading governs the transition from pit to crack as well as the crack growth in reinforcing bars.

The corrosion-fatigue deterioration process is basically divided into two stages: (1) pit formation and growth; and (2) fatigue crack growth. The former involves electrochemical processes that depend mainly on environmental factors. The latter is commonly modeled using Linear Elastic Fracture Mechanics (LEFM) and depends mostly on both cyclic loads and material properties. Goswami and Hoepfner (1995) separate, conceptually, corrosion-fatigue life into the following stages: (1) electrochemical stage and pit nucleation, (2) pit growth, (3) competitive mechanisms between pit growth and fatigue crack nucleation, (4) chemically, "short" crack growth, (5) transition from "short crack" to "long crack", (6) long crack growth, and (7) corrosion fatigue crack growth until instability. However, assuming initial immunity of RC structures against corrosion and the fact that some of these stages proposed by Goswami and Hoepfner (1995) are transitional, the total corrosion-fatigue life, t_T , can be divided into the following stages (Figure 3.11):

1. corrosion initiation and pit nucleation, t_{cp} ,
2. pit-to-crack transition, t_{pt} , and
3. crack growth, t_{cg} .

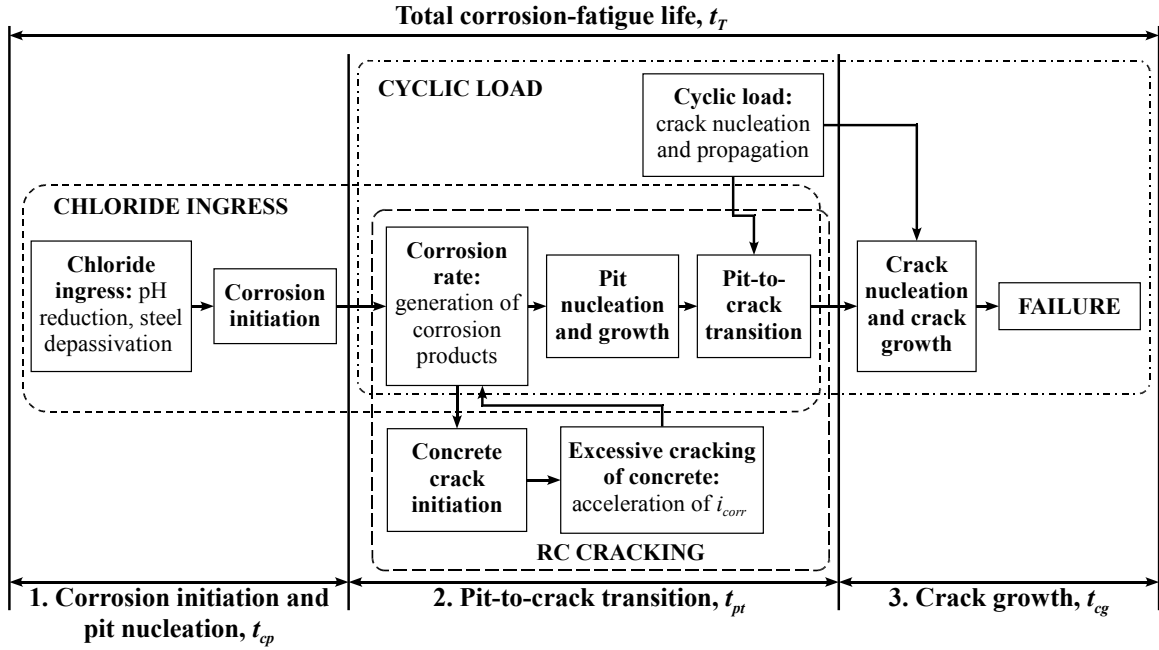


Figure 3.11: Scheme of corrosion-fatigue deterioration process in RC structures.

3.4.1 Corrosion initiation and pit nucleation, t_{cp}

This stage is divided into two sub-stages:

1. time to corrosion initiation, t_{ini} , and
2. time to pit nucleation, t_{pn} .

The first sub-stage describes the time from the end of construction until depassivation of the corrosion protective layer of reinforcing steel, and subsequently, corrosion initiation. For RC structures, the length of this stage depends mainly on the concrete characteristics, the thickness of the cover and environmental factors; it is usually computed by the analytical solution of Fick's law. Nonetheless, to perform a realistic assessment, it is advisable to implement a comprehensive model such as the one presented in section 3.2.

Pit nucleation is the result of an electrochemical process induced by corrosion. Computing the time to pit nucleation, t_{pn} , is not trivial because it depends on several environmental, material and loading factors whose interaction is still not well understood. This study assumes that: (1) chloride ingress produces pitting corrosion and (2) pit growth initiates once corrosion starts. The pit depth at time t , $p(t)$, can be calculated as (Jones, 1992):

$$p(t) = 0.0116\alpha \int i_{corr}(t) dt \quad (3.47)$$

where $p(t)$ is given in mm, α is the ratio between pitting and uniform corrosion depths, and $i_{corr}(t)$ is the time-variant corrosion rate in $\mu A/cm^2$. The time to pit nucleation is estimated by defining a threshold, p_0 , for the pit depth, $p(t)$. For example, according to Harlow and Wei (1998), this value

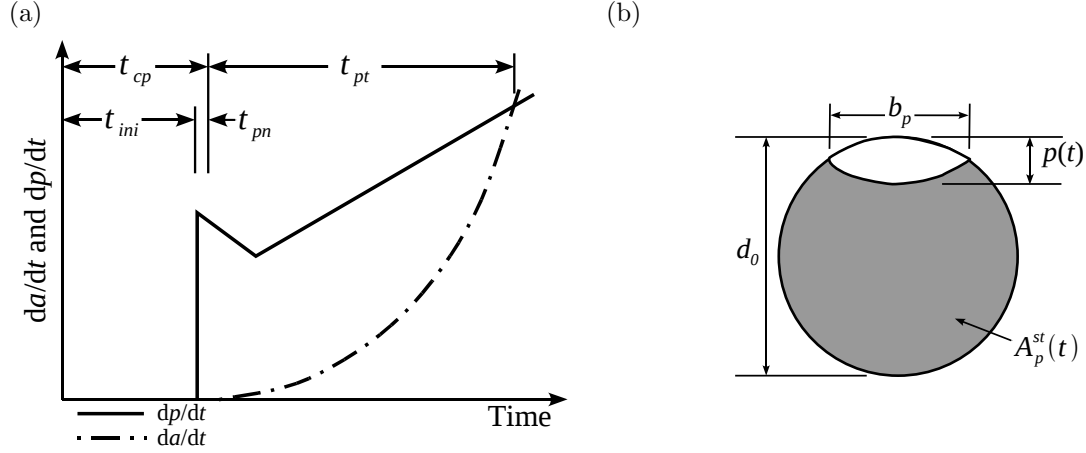


Figure 3.12: (a) Rate competition criterion. (b) Pit shape.

is $p(t_{pn}) = p_0 = 1.98 \times 10^{-6}$ m. After steel depassivation, i.e. $t_{ini} + 1\text{year} \geq t > t_{ini}$, it is reasonable to assume that $i_{corr}(t)$ remains constant and equal to (Vu and Stewart, 2000):

$$i_{corr}(t) = i_{ini} = \frac{37.8(1 - w/c)^{-1.64}}{c_t} \quad (3.48)$$

where w/c is the water-cement ratio and c_t is given in mm. Consequently, by making $p(t_{pn}) = p_0$ in equation 3.47, substituting equation 3.48 in equation 3.47 and integrating, the time to pit nucleation, t_{pn} , can be written as:

$$t_{pn} = \frac{2.281c_t p_0}{\alpha} (1 - w/c)^{1.64} \quad (3.49)$$

Equation 3.49 provides a simple relationship to estimate t_{pn} based on electrochemical principles. Other proposals to obtain t_{pn} can be found in the literature (Shi and Mahadevan, 2001); however, this discussion is beyond the scope of this study.

3.4.2 Pit-to-crack transition, t_{pt}

The time of transition from pit to crack, t_{pt} , is defined as the time at which the maximum pit depth reaches a critical value leading to crack nucleation. Crack nucleation depends on the competition between the corrosion pit growth and fatigue crack propagation. There are two approaches to estimate this transition period (Kondo, 1989; Chen et al., 1996):

1. *Rate competition criterion*: the transition takes part when the crack growth rate, da/dt , exceeds the pit growth rate, dp/dt , as illustrated in Figure 3.12a.
2. *Fatigue threshold criterion*: the transition occurs when the stress intensity factor of the equivalent surface crack growth for the pit, ΔK_{eq} , reaches the threshold stress intensity factor for fatigue crack growth, ΔK_{tr} .

In this study, the fatigue threshold criterion was not considered because experimental observations indicate that this criterion is not appropriate to estimate fatigue crack nucleation at low loading frequencies (Chen et al., 1996). Therefore, the rate competition criterion, where pit growth rate is described by electrochemical mechanisms and fatigue crack growth rate is estimated in terms of LEFM, will be discussed in the following sections. This discussion will focus on: (1) pit growth rate, (2) fatigue crack growth rate and (3) computation of pit-to-crack transition.

3.4.2.1 Pit growth rate

After pit nucleation and as a result of localized galvanic corrosion, pit growth can be estimated in terms of the change in the volumetric rate by using Faraday's law (Kondo, 1989; Harlow and Wei, 1998):

$$\frac{dV}{dt} = \frac{Mi_{corr}}{n_{Fe}F\rho_{Fe}} \quad (3.50)$$

where M is the molecular weight of iron ($M = 55.85$ g/mol), i_{corr} is the corrosion rate, n_{Fe} is the valence of iron, $n_{Fe} = 2$, F is the Faraday's constant, -i.e. $F = 96500$ C/mol, and ρ_{Fe} is the density of iron ($\rho_{Fe} = 7850$ kg/m³). Corrosion rate is the effective galvanic current between the particles and the steel matrix. For corrosion-fatigue models, the corrosion rate usually takes into account the dependence on temperature by using the Arrhenius equation:

$$i_{corr} = i_{p0} \exp\left(\frac{-\Delta H}{RT}\right) \quad (3.51)$$

where i_{p0} is the pitting current coefficient, ΔH is the activation enthalpy, R is the universal gas constant ($R = 8.314$ /mol K), and T is the absolute temperature. It is clear, from equation 3.51, that the corrosion rate increases when temperature is raised. Nevertheless, given the complexity of the corrosion process in RC, the relationship between i_{corr} and T is not simple. For instance, it has been found that the corrosion kinetics for different RC structures under conditions of constant temperature can vary widely (López et al., 1993). This variability results from the interaction between temperature and other factors such as conductivity and relative humidity. Thus, a time-variant corrosion rate model as presented in section 3.3.3 is more suitable than equation 3.51 because it considers the effect of concrete cracking.

Pit formation is a random phenomena which depends on material properties, fabrication processes and electrochemical factors (Goswami and Hoepfner, 1995). Currently, this dependence is not well understood. Some authors assume that pit growth follows the shape of a hemisphere or a prolate spheroid (Kondo, 1989; Harlow and Wei, 1998). For simplicity, a spherical shape of the pit is assumed herein (Figure 3.12b) where the maximum pit depth, $p(t)$, can be estimated from equation 3.47. Thus, the volumetric rate of pit growth (equation 3.50) can be directly rewritten in terms of pit growth rate, dp/dt , by deriving equation 3.47 with respect to time (Figure 3.12a):

$$\frac{dp}{dt} = 0.0116\alpha i_{corr}(t) \quad (3.52)$$

3.4.2.2 Fatigue crack growth rate

Fatigue crack growth rate is estimated by using Paris-Erdogan law:

$$\frac{da}{dN} = C_p (\Delta K)^{m_p} \quad (3.53)$$

where a is the crack size, N is the number of cycles, ΔK is the alternating stress intensity factor, and C_p and m_p are material constants. Alternatively, equation 3.53 can be rewritten in terms of time:

$$\frac{da}{dt} = C_p (\Delta K)^{m_p} f \quad (3.54)$$

where f is the frequency of the cyclic load. It has been established that there is a strong correlation between C_p and m_p , and their values are highly dependent on environmental aggressiveness. For RC structures, Salah el Din and Lovegrove (1982) reported experimental values for C_p and m_p corresponding to medium and long crack growth stages, leading to:

$$\frac{da}{dt} = \begin{cases} 3.83 \times 10^{-29} (\Delta K)^{20.863} f & \text{for } \Delta K \leq 9 \text{ MPa}\sqrt{\text{m}} \\ 3.16 \times 10^{-12} (\Delta K)^{3.143} f & \text{otherwise} \end{cases} \quad (3.55)$$

The stress intensity factor, ΔK , is computed as:

$$\Delta K(a) = \Delta \sigma Y(a/d_0) \sqrt{\pi a} \quad (3.56)$$

where $\Delta \sigma$ is the stress range, i.e. $\Delta \sigma = \sigma_{max} - \sigma_{min}$, d_0 is the initial diameter of the bar and $Y(a/d_0)$ is a dimensionless geometry notched specimen function, which can be approximated by (Murakami and Nisitani, 1975):

$$Y(a/d_0) = \frac{1.121 - 3.08(a/d_0) + 7.344(a/d_0)^2 - 10.244(a/d_0)^3 + 5.85(a/d_0)^4}{[1 - 2(a/d_0)^2]^{3/2}} \quad (3.57)$$

The dotted line in Figure 3.12a follows the shape of the fatigue crack growth rate as a function of time, which starts growing after corrosion initiation and pit nucleation.

3.4.2.3 Computation of pit-to-crack transition

In order to find the time for pit-to-crack transition, t_{pt} , an equivalent stress intensity factor for the pit, ΔK_{pit} must be estimated. ΔK_{pit} is found by substituting a in equation 3.56 by the pit depth $p(t)$ (equation 3.47):

$$\Delta K_{pit}(t) = \Delta \sigma Y(p(t)/d_0) \sqrt{\pi p(t)} \quad (3.58)$$

Then, the equivalent crack growth rate becomes:

$$\frac{da}{dt} = C_p [\Delta K_{pit}(t)]^{m_p} f \quad (3.59)$$

Therefore, the time of pit-to-crack transition is obtained by equating the pit growth rate (equation 3.52) with the equivalent crack growth rate (equation 3.59), and solving for t_{pt} :

$$0.0116\alpha i_{corr}(t_{pt}) = C_p(\Delta K_{pit}(t_{pt}))^m f \quad (3.60)$$

In order to calculate t_{pt} , equation 3.60 must be solved numerically. Figure 3.12a illustrates the graphical solution for t_{pt} , where the time of pit-to-crack transition is found at the intersection between the continuous and dotted lines.

3.4.3 Crack growth, t_{cg}

This section focuses on the time from crack initiation until crack size reaches a value that causes failure. The size of the initial crack in the steel reinforcement, a_0 , is estimated as the pit depth when the transition from pit to crack is reached, i.e. $a_0 = p(t_{pt})$ (equation 3.47). The size of the critical crack, a_c , is the crack size at which the RC member reaches a limit state of resistance (e.g. bending capacity). This time is obtained by integrating equation 3.55:

$$t_{cg} = \begin{cases} \frac{1}{f} \left(\int_{a_0}^{a_1} \frac{da}{3.83 \times 10^{-29} (\Delta K)^{20.863}} + \int_{a_1}^{a_c} \frac{da}{3.16 \times 10^{-12} (\Delta K)^{3.143}} \right) & \text{for } a_0 < a_1 \\ \frac{1}{f} \int_{a_0}^{a_c} \frac{da}{3.16 \times 10^{-12} (\Delta K)^{3.143}} & \text{otherwise} \end{cases} \quad (3.61)$$

where a_1 is the crack size at which the crack growth rate changes from medium to long crack growth. The transition between medium and long crack growth occurs when crack size reaches a threshold stress intensity factor estimated by $\Delta K(a_1) = 9 \text{ MPa}\sqrt{\text{m}}$ (Salah el Din and Lovegrove, 1982).

3.5 Summary and conclusions

The flowchart that summarizes the entire coupled model is depicted in Figure 3.13. The corrosion initiation process depends on both environmental features and structural configuration. After corrosion initiation, the accumulation of corrosion products in the concrete/steel interface affects the corrosion rate as a result of excessive concrete cracking. The change in the corrosion rate depends on environmental aggressiveness. By considering the interaction between pit growth and cyclic load, the rate competition criterion is evaluated, and consequently, the time of pit-to-crack transition is assessed. Finally, the crack growth becomes the governing process leading to failure.

The proposed model evaluates the total structural lifetime considering: corrosion initiation, pit-to-crack transition and crack propagation. Its robustness lies in the implicit integration of various parameters and processes affecting RC lifetime.

The conclusions of this chapter are:

1. The basic principles of the chloride penetration model consider: (1) chloride binding capacity, (2) effects of concrete aging (3) two-dimensional flow of chlorides in unsaturated concrete; and (4) the time-variant inputs for environmental temperature, humidity and chloride concentration. Since the problem is represented by a set of PDEs, a numerical approach combining finite difference and finite elements was implemented to estimate chloride penetration. In general, the results of the computer code showed significant agreement with analytical and numerical solutions.

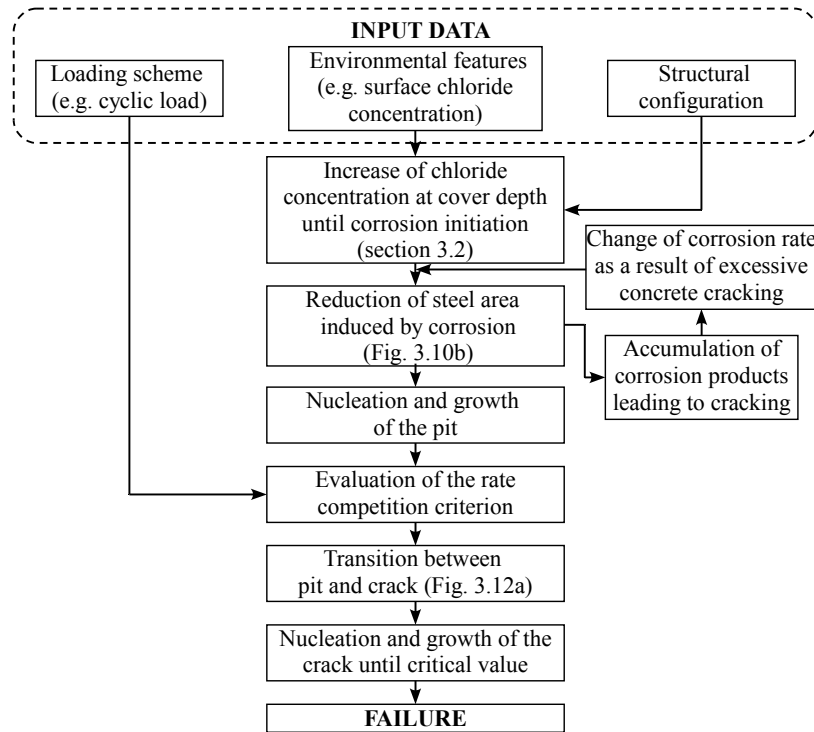


Figure 3.13: Flowchart of the proposed model of corrosion, cracking and fatigue.

2. This chapter developed a model to account for the influence of concrete cracking on corrosion rate. The proposed model assumes that severe cracking induces an increment of the oxygen diffusion coefficient. Therefore, the change in the oxygen diffusion coefficient raises the availability of oxygen at the corrosion cell increasing the corrosion rate. The corrosion rates estimated with this model are within the range of those reported by Geocisa and the Torroja Institute (2002). Future research could address the influence of humidity and electrical resistivity of concrete on corrosion rate.
3. The combined action of corrosion, concrete cracking and fatigue strongly influences the performance of RC structures and substantially reduces lifetime. The last part of this chapter develops a model that couples these phenomena. For the proposed model, corrosion nucleates a pit which is then transformed into a crack as a result of cyclic loading. Eventually, crack growth leads to structural failure.

CHAPTER 4

STOCHASTIC CORROSION-FATIGUE MODEL

4.1 Introduction

A comprehensive deterioration model should take uncertainty into account in order to make rational predictions about structural lifetime. In most engineering problems, uncertainty can be classified into the following categories (Smithson, 1989; Blockley, 1996):

1. *Randomness* is the lack of a pattern in a model or a parameter. It is present when the possible results of an experiment are known *a priori* but the result cannot be predicted with certainty.
2. *Fuzziness* is related to imprecision of definition and usually depends on the subjective interpretation of the observer. This uncertainty often results from expert appreciation of a problem. A property (e.g., cold, old, loud. etc.) is fuzzy if a precise measurement of this property can be obtained in principle.
3. *Incompleteness* refers to the quantitative insufficiency of knowledge of a problem. For this case, the information is concise, true and does not depend on the point of view of the observer. Incompleteness can be eliminated by looking for more information.

Randomness and fuzziness are characteristic of corrosion-fatigue of RC structures, where there are three sources of uncertainty associated with (1) material properties, (2) models and their parameters, and (3) environmental actions. Therefore, the purpose of this chapter is to incorporate the stochastic nature of the variables in the mechanical model of corrosion-fatigue described in chapter 3. The specific objectives of this chapter are:

1. to determine the sources and the type of uncertainty related to corrosion-fatigue;
2. to present and describe reliability problems in RC structures subjected to corrosion-fatigue;
3. to obtain and describe the models for all random/fuzzy variables and
4. to present the methodology for reliability analysis.

Figure 4.1 depicts the probabilistic approach adopted in the present study. The first part of this chapter (section 4.2) introduces some basic aspects of reliability theory and describes the limit state functions implemented in this study. The following sections present the inputs for the probabilistic

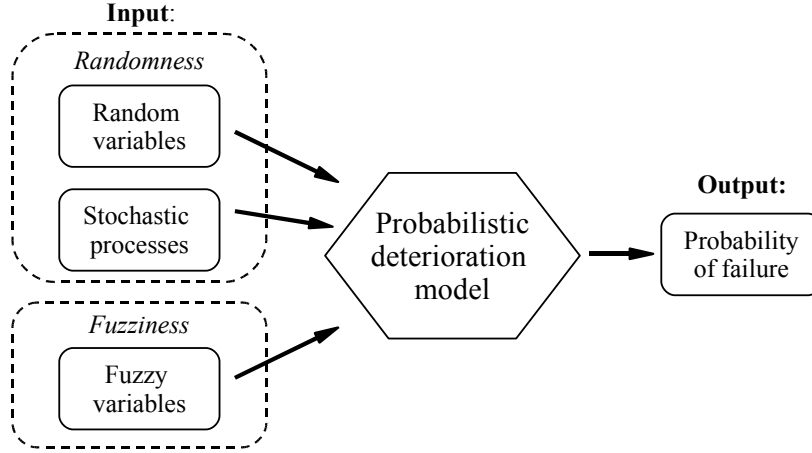


Figure 4.1: Proposed probabilistic approach.

deterioration model. The probabilistic models for the time-invariant random variables were defined on the basis of a literature review and are presented in section 4.3. Section 4.4 describes the proposed stochastic models for humidity and temperature. These models include the effect of global warming. Section 4.5 outlines the proposed stochastic models for environmental chloride concentration. Section 4.6 presents the fuzzy approach proposed to model corrosion rate.

4.2 Probabilistic framework for reliability analysis

The main goal of reliability analysis is to evaluate the ability of systems or components to remain safe and operational during their life-cycle. This information can be used to define criteria for decision making, improve the management of resources, perform sensitivity studies, etc. The criterion to separate “failure” and “non failure” is defined by the so-called *limit state function* $g(\cdot)$:

$$g(\mathbf{X}) = \mathcal{R}(\mathbf{X}) - \mathcal{S}(\mathbf{X}) \quad (4.1)$$

where \mathbf{X} is the vector containing the random variables of the problem and \mathcal{R} ; and \mathcal{S} represent the resistance and the demand on the system, respectively. Thus, whereas $\{\mathbf{x} : g(\mathbf{x}) > 0\}$ indicates that the system is safe (safe domain), $\{\mathbf{x} : g(\mathbf{x}) \leq 0\}$ denotes failure (failure domain), where \mathbf{x} is a realization of \mathbf{X} . The *probability of failure*, p_f , is an estimate of the safety of the system and can be evaluated as:

$$p_f = P[g(\mathbf{X}) \leq 0] = \int_{g(\mathbf{X}) \leq 0} f_{\mathbf{X}}(\mathbf{x}) dx_1 \dots dx_n \quad (4.2)$$

where $f_{\mathbf{X}}(\mathbf{x})$ is the joint probability density function of \mathbf{X} . There are several methods to evaluate equation 4.2 (Melchers, 1999; Haldar and Mahadevan, 2000). Given the complexity of the solution procedure used to estimate the evolution of chloride profiles, corrosion propagation, concrete cracking, crack nucleation and propagation; closed-form solutions for both the CDF of the time to corrosion initiation and the total corrosion-fatigue life are hard to find. Therefore, an appropriate tool to

deal with this kind of problem is to use Monte Carlo simulations. This study also implements Latin Hypercube sampling to reduce the computational cost of simulations. See Appendix A for more details on these methods.

The limit state functions defined in this study consider the following structural conditions:

- *Serviceability limit state*: this condition is satisfied when structures are still considered useful and safe although a given degree of deterioration is observed. For the problem treated in this study, the serviceability limit state is related to the *probability of corrosion initiation*.
- *Ultimate limit state*: this condition describes the state at which the structural safety is highly affected and may lead to total failure or collapse. In the case of corrosion-fatigue, the effective cross-sectional area of steel is reduced and failure occurs when the applied load exceeds the remaining resistance. The ultimate limit state is related to the *probability of failure*.

The probability of corrosion initiation and the probability of failure can be useful in lifetime assessment or maintenance/repair management of RC structures.

4.2.1 Probability of corrosion initiation

The time to corrosion initiation, t_{ini} , is defined as the time at which the chloride concentration at the steel reinforcement surface reaches a threshold value, C_{th} . This threshold concentration represents the chloride concentration for which the rust passive layer of steel is destroyed and the corrosion reaction begins. Note that this threshold is sensitive to the chemical characteristics of concrete components: sand, gravel and cement. Therefore, it is assumed herein that C_{th} is a random variable. The time to corrosion initiation is obtained by evaluating the time-dependent variation of the chloride concentration at the reinforcing steel. This is computed in the present study by solving the system of partial differential equations presented in section 3.2. The cumulative distribution function of time to corrosion initiation, $F_{t_{ini}}(t)$, is defined as:

$$F_{t_{ini}}(t) = P[t_{ini} \leq t] = \int_{t_{ini} \leq t} f_{\mathbf{X}}(\mathbf{x}) d\mathbf{x} \quad (4.3)$$

where \mathbf{X} is a vector of random variables and $f_{\mathbf{X}}(\mathbf{x})$ is the joint probability density function of \mathbf{X} . The limit state function that defines corrosion initiation can be written as:

$$g(\mathbf{X}, t) = C_{th}(\mathbf{X}) - C_{tc}(\mathbf{X}, t) \quad (4.4)$$

where $C_{tc}(\mathbf{X}, t)$ is the total concentration of chlorides at the concrete cover depth c_t at time t . The probability of corrosion initiation, p_{ini} , is obtained by integrating the joint probability function over the failure domain –i.e., equation 4.2.

4.2.2 Probability of failure

Given the complexity of the deterioration process, the total corrosion-fatigue life t_T is estimated as the sum of the length of three consecutive stages: (1) corrosion initiation and pit nucleation, t_{cp} ; (2)

pit-to-crack transition, t_{pt} , and (3) crack growth, t_{cg} . The cumulative distribution function of the total corrosion-fatigue life, $F_{t_T}(t)$, is defined by Zhang and Mahadevan (2001) as:

$$F_{t_T}(t) = P[t_T \leq t] = \int_{t_{cp}+t_{pt}+t_{cg} \leq t} f_{\mathbf{X}}(\mathbf{x}) d\mathbf{x} \quad (4.5)$$

where \mathbf{X} is the vector of random variables and $f_{\mathbf{X}}(\mathbf{x})$ is the joint probability density function of \mathbf{X} . If structural failure is achieved when the crack or pit size reaches a critical value, inducing the cross-section failure, the limit state function becomes:

$$g(\mathbf{X}, t) = a_c(\mathbf{X}) - a_t(\mathbf{X}, t) \quad (4.6)$$

where $a_t(\mathbf{X}, t)$ is the crack or pit size at time t and $a_c(\mathbf{X})$ is the critical crack or pit size corresponding to structural failure. For the above limit state function, there are two mechanisms leading to failure. In the first mechanism, the transition process from pit to crack described in chapter 3 takes place, and consequently, failure is generated by crack propagation. In the second mechanism, the transition does not occur because the pit growth rate is higher than the crack growth rate and corrosion becomes the leading failure mechanism. Failure induced by corrosion occurs when both the frequency and intensity of the load are low and/or when the structure is located in a highly aggressive environment.

The critical crack or pit size $a_c(\mathbf{X})$ can be defined as: (1) a deterministic value given by a fraction of the bar diameter (Salah el Din and Lovegrove, 1982; Zhang and Mahadevan, 2001), or (2) a probabilistic value estimated in terms of ultimate limit states. In this study, $a_c(\mathbf{X})$ is a random variable resulting from the evaluation of the limit state of bending which can be written as:

$$g_r(A_s(a), \mathbf{X}) = M_f(A_s(a), \mathbf{X}) - M_e(\mathbf{X}) \quad (4.7)$$

where $A_s(a)$ is the net steel area, \mathbf{X} is the vector of random variables (i.e., applied load, concrete compressive strength, yield stress, etc.), $M_f(A_s(a), \mathbf{X})$ is the bending moment capacity and $M_e(\mathbf{X})$ is the applied moment. From equation 4.7, it is noteworthy that the net steel area is a function of the crack length or pit size a . Thus, by defining A_0 as the initial cross-sectional area and $\Delta A_s(a)$ as the cross-section loss by corrosion-fatigue action, $A_s(a)$ is given by (See Figure 4.2):

$$A_s(a) = A_0 - \Delta A_s(a) \quad (4.8)$$

Figure 4.2 shows the relationship between bending moment and the crack or pit size. For the initial cross-sectional area of steel, the crack or pit size is equal to zero and the bending moment capacity is higher than the applied moment. When the crack length or pit size reaches a critical value, $a = a_c$, the bending moment capacity is equal to the applied moment causing failure:

$$M_f(A_s(a_c), \mathbf{X}) = M_e(\mathbf{X}) \quad (4.9)$$

where $A_s(a_c)$ represents the critical cross-section. The bending moment capacity can be computed as:

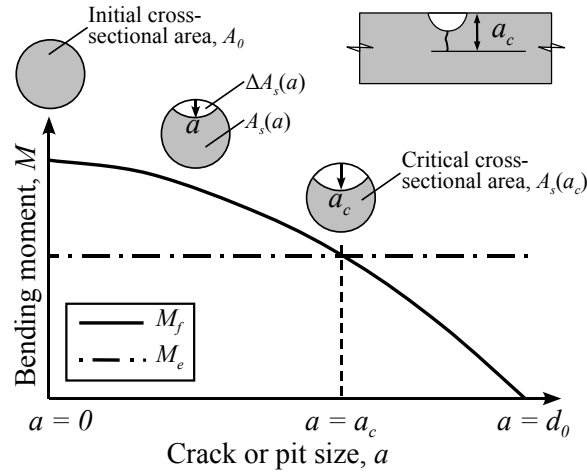


Figure 4.2: Schematic description of the computation of a_c .

$$M_f(A_s(a), \mathbf{X}) = A_s(a) f_y \left(d - 0.5 \frac{A_s(a) f_y}{f'_c b} \right) \quad (4.10)$$

where f_y is the steel yield stress, d is the effective depth of the beam, f'_c is the concrete compressive strength and b is the beam width. Thus, $A_s(a_c)$ is estimated by substituting equation 4.10 into equation 4.9:

$$A_s(a_c) = \frac{1}{f_y} \left(df'_c b - \sqrt{(df'_c b)^2 - 2f'_c b M_e(\mathbf{X})} \right) \quad (4.11)$$

Depending on the shape of the crack or the pit, a_c is obtained from equation 4.11. Given the complexity of estimating A_s as function of the crack length or pit size, a_c is computed iteratively. Equation 4.11 indicates that, for the limit state of bending, $a_c(\mathbf{x})$ does not depend on either the corrosion process nor the frequency of the cyclic load. Nonetheless, the time taken to reach $a_c(\mathbf{x})$, t_T , depends on both environmental aggressiveness and frequency of the cyclic loading. Failure probability, p_f , is estimated from equation 4.2 by considering the limit state function defined by equation 4.6.

4.3 Time-invariant random variables

This section describes the nature and existing models that describe the random variables involved within the corrosion-fatigue of RC structures. The random variables considered in the proposed corrosion-fatigue model are defined on the basis of previous probabilistic and deterministic studies. Since there are several physical problems involved in this deterioration problem (diffusion, convection, corrosion, etc.), the random variables are classified into the following categories:

- random variables related to chloride penetration (section 4.3.2), and
- random variables after corrosion initiation (section 4.3.3).

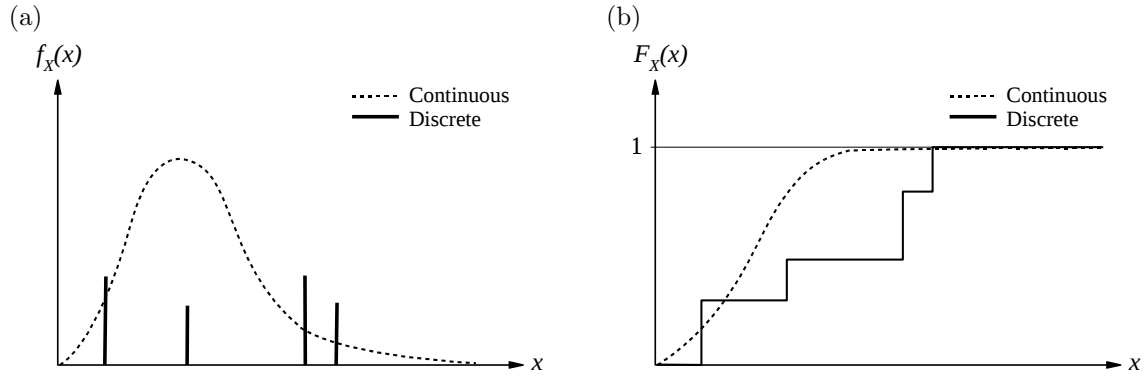


Figure 4.3: Illustrations of (a) probability distribution function and (b) cumulative distribution function.

4.3.1 Basic concepts of random variables

In probability theory the set of all possible outcomes for a random phenomenon defines the sample space Ω . An event E is defined as a subset of Ω containing outcomes $\omega \in \Omega$. The set of events defines the σ -algebra \mathcal{F} associated with Ω . A *probability measure* P associates numbers to events –i.e., $P : \mathcal{F} \mapsto [0, 1]$, indicating their probability of occurrence. Since the probability measures follow Kolmogorov’s axioms, the *probability space* which fulfills with these characteristics is noted (Ω, \mathcal{F}, P) .

In a probability space (Ω, \mathcal{F}, P) , a *random variable* X is said to be a *measurable function* such as: $X : \Omega \rightarrow \mathcal{D}_X \subset \mathbb{R}$. Where \mathcal{D}_X is a set that depends on the type of the random variable – i.e., *discrete* or *continuous*. The cumulative distribution function (CDF), $F_X(x)$, describes a random variable completely and is expressed as:

$$F_X(x) = P(X \leq x) \quad (4.12)$$

If the random variable is *discrete* (Figure 4.3), its CDF becomes:

$$F_X(x) = \sum_{i \in \mathbb{N}} p_i \mathbf{1}_{\{x^{(i)} \leq x\}}(x) \quad (4.13)$$

where p_i is probability mass function –i.e., $p_i = P(X = x^{(i)})$ and $\mathbf{1}_{\{x^{(i)} \leq x\}}(x)$ is the indicator function of the set $\{x \in \mathbb{R} : x^{(i)} \leq x\}$, which takes the following values:

$$\mathbf{1}_{\{x^{(i)} \leq x\}}(x) = \begin{cases} 1 & \text{for } x^{(i)} \leq x \\ 0 & \text{otherwise} \end{cases} \quad (4.14)$$

If the random variable is *continuous* (Figure 4.3), the probability density function (PDF) can be computed as:

$$f_X(x) = \lim_{h \rightarrow 0, h > 0} \frac{P(x \leq X \leq x + h)}{h} = \frac{dF(x)}{dx} \quad (4.15)$$

The probability distribution of a random variable is often characterized by the n -th moments of

the variable. The following moments (measures) are usually used to characterize a random variable X :

- the *expected value* or *mathematical expectation* $E[X]$ or μ_X ;
- the *variance* $\text{Var}[X]$; and
- the *coefficient of variation* $\text{COV}[X]$, which can be estimated as $\text{COV}[X] = \sigma_X/\mu_X$.

Further descriptions and details on probability theory can be found in (Gut, 2005; Ross and Pekoz, 2007).

4.3.2 Random variables related to chloride penetration

This section presents the random variables used in the chloride penetration model (section 3.2.1). The following variables are treated as random:

1. Chloride ingress:
 - reference chloride diffusion coefficient, $D_{c,ref}$;
 - activation energy of the chloride diffusion process, U_c ; and
 - age reduction factor, m_c .
2. Moisture diffusion:
 - reference humidity diffusion coefficient, $D_{h,ref}$;
 - parameter representing the ratio $D_{h,min}/D_{h,max}$, α_0 ; and
 - parameter characterizing the spread of the drop in D_h , n .
3. Heat transfer:
 - thermal conductivity of concrete, λ ;
 - concrete specific heat capacity, c_q ; and
 - density of concrete, ρ_c .

The distributions and the probability measures of these variables are presented in Table 4.1. These values have been estimated for ordinary Portland concrete with $w/c = 0.5$ and are valid for unsaturated conditions.

4.3.3 Random variables after corrosion initiation

In chloride-contaminated environments, corrosion occurs because of localized breakdown of the passive layer when a sufficient amount of chloride ions reach the reinforcing steel. The random variables after corrosion initiation are:

1. Computation of the time to corrosion initiation:
 - chloride threshold concentration, C_{th} ; and

Table 4.1: Random variables related to chloride penetration.

Variable	Mean	COV	Distribution	Reference
$D_{c,ref}$	$3 \times 10^{-11} \text{ m}^2/\text{s}$	0.20	log-normal	Saetta et al. (1993); Duracrete (2000); Val and Trapper (2008)
U_c	41.8 kJ/mol	0.10	beta on [32,44.6]	Collepardi et al. (1972); Page et al. (1981)
m_c	0.15	0.30	beta on [0,1]	Page et al. (1981); Val (2006)
$D_{h,ref}$	$3 \times 10^{-10} \text{ m}^2/\text{s}$	0.20	log-normal	Bazant and Najjar (1971, 1972); Saetta et al. (1993); Val and Trapper (2008)
α_0	0.05	0.20	beta on [0.025,0.1]	Val and Trapper (2008)
n	11	0.10	beta on [6,16]	Bazant and Najjar (1971, 1972); Val and Trapper (2008)
λ	2.5 W/(m °C)	0.20	beta on [1.4,3.6]	Neville (1981)
c_q	1000 J/(kg °C)	0.10	beta on [840,1170]	Neville (1981)
ρ_c	2400 kg/m ³	0.20	normal	

- concrete cover thickness, c_t .

2. Concrete cracking:

- density of rust products, ρ_{rust} ;
- thickness of the porous band around the bar, τ_{por} ; and
- pitting factor, α .

3. RC strength:

- compressive strength of concrete, f'_c ;
- tensile strength of concrete, f_{ct} ;
- modulus of elasticity of concrete, E_{cm} ; and
- yield stress of reinforcement, f_y .

The random variables presented in Table 4.2 are valid for ordinary Portland concrete with $w/c = 0.5$. The variables f'_{ck} and f_{yk} represent the characteristic compressive cylinder strength and the characteristic yield stress of reinforcement, respectively. The characteristic values of strength are defined by the European standard (2004) as that value of strength below which 5% of all possible strength test results may be expected to fall. f'_{ck} should be expressed in N/mm² to estimate f_{ct} and E_{cm} .

4.4 Stochastic model for humidity and temperature

In order to make a good estimation of the time to corrosion initiation, it is important to implement a model that realistically reproduces the temperature and humidity in the environment. This section proposes a weather model that adds a stochastic perturbation to a sinusoidal mean trend representing the seasonal variations.

A scalar stochastic process $H(\mathbf{x}, \omega)$ is a collection of random variables indexed by a continuous parameter $\mathbf{x} \in \mathcal{B}$, where \mathcal{B} is an open set of \mathbb{R}^d which describes the geometry of the physical system

Table 4.2: Random variables after corrosion initiation.

Variable	Mean	COV	Distribution	Reference
C_{th}	0.48 ^a wt.-%Cl cement	0.15 ^a	normal	Duracrete (2000)
	1.60 ^b wt.-%Cl cement	0.20 ^b	normal	Duracrete (2000)
	0.50 ^c wt.-%Cl cement	0.10 ^c	normal	Duracrete (2000)
c_t	nominal	0.25	normal ^d	Duracrete (2000); McGee (2000); Val and Stewart (2003)
f'_c	$f'_{c_k}/(1 - 1.64COV)$	0.15	normal	Melchers (1999); European standard (2004)
f'_{ct}	$0.3f'_{c_k}{}^{2/3}$			European standard (2004)
E_{cm}	$9.5(f'_{c_k} + 8)^{1/3}$			European standard (2004)
f'_y	$f_{y_k}/(1 - 1.64COV)$	0.10	normal	Melchers (1999); European standard (2004)
ρ_{rust}	3,600 kg/m ³	0.10	normal	Liu (1996); Thoft-Christensen (2000)
τ_{por}	12.5 μ m	0.20	normal	Liu (1996); Thoft-Christensen (2000)
α	5.65	0.22	Gumbel	Tuutti (1982); González et al. (1995); Stewart (2004)

^aaccording to “definition 1” (section 2.4.2).

^baccording to “definition 2” and valid for constantly water saturated conditions.

^caccording to “definition 2” and valid for constantly humid conditions.

^dtruncated at 10 mm (lower bound)

($d = 1, 2,$ or 3 in practice). $H(\mathbf{x}_0, \omega)$ is a *random variable* for a given $\mathbf{x}_0 \in \mathcal{B}$ or is a *realization* of the process for a given outcome $\omega_0 \in \Omega$. For the sake of simplicity, this study focuses only on scalar stochastic processes.

A stochastic process is called *Gaussian* if all its components $\{H(\mathbf{x}_1), \dots, H(\mathbf{x}_q)\}$ are Gaussian. Gaussian stochastic processes are of practical interest because they are completely defined by their mean $\mu(\mathbf{x})$ and their autocovariance function:

$$C_{HH}(\mathbf{x}, \mathbf{x}') = \text{Cov}[H(\mathbf{x}), H(\mathbf{x}')] \quad (4.16)$$

The autocorrelation function $\rho(\mathbf{x}, \mathbf{x}')$ is also used to describe the process:

$$\rho(\mathbf{x}, \mathbf{x}') = \frac{C_{HH}(\mathbf{x}, \mathbf{x}')}{\sigma(\mathbf{x})\sigma(\mathbf{x}')} \quad (4.17)$$

where the variance function $\sigma^2(\mathbf{x})$ is:

$$\sigma^2(\mathbf{x}) = C_{HH}(\mathbf{x}, \mathbf{x}). \quad (4.18)$$

According to Ghanem and Spanos (1991), there are two efficient methods to manage stochastic processes: Karhunen-Loève expansion or polynomial chaos. Taking into account the complexity of the implementation and the computational time, Karhunen-Loève was selected as the most suitable method to represent the weather variables.

4.4.1 Karhunen-Loève discretization of humidity and temperature

Analogous to Fourier series, the Karhunen-Loève expansion represents a stochastic process as a combination of orthogonal functions on a bounded interval –i.e., $[-l, l]$. The development of a stochastic

process by the Karhunen-Loève method is based on the spectral decomposition of the covariance function of the process. Since the covariance function is symmetrical and positive definite, its eigenfunctions are orthogonal and form a complete set of deterministic orthogonal functions, $f_i(t)$, which are used to represent the stochastic process. The random coefficients of the process $\xi_i(\omega)$ can also be considered orthogonal or, in other words, statistically uncorrelated.

Let $\kappa_\phi(t, \omega)$ be a stochastic process describing the humidity or temperature ϕ and defined over the domain \mathcal{B} , with ω belonging to the space of random events Ω . $\kappa_\phi(t, \omega)$ can thus be expanded as follows (Ghanem and Spanos, 1991):

$$\kappa_\phi(t, \omega) \simeq \bar{\kappa}_\phi(t) + \sum_{i=1}^{n_{KL}} \sqrt{\lambda_i} \xi_i(\omega) f_i(t) \quad (4.19)$$

where $\bar{\kappa}_\phi(t)$ is the mean of the process, $\xi_i(\omega)$ is a set of normal random variables, n_{KL} is the number of terms of the truncated discretization, t is the time and λ_i are the eigenvalues of the covariance function $C_{\kappa_\phi \kappa_\phi}(t_1, t_2)$ resulting from the evaluation of the following expression:

$$\int_{\mathcal{B}} C_{\kappa_\phi \kappa_\phi}(t_1, t_2) f_i(t_2) dt_2 = \lambda_i f_i(t) \quad (4.20)$$

The solution of equation 4.20 can be determined analytically when the covariance function is exponential or triangular (Ghanem and Spanos, 1991). This study assumes that the processes of humidity and temperature have an exponential covariance of the form:

$$C_{\kappa_\phi \kappa_\phi}(t_1, t_2) = e^{-|t_1 - t_2|/b_e} \quad (4.21)$$

where b_e is the correlation length and must be expressed in the same units of t . Then, accounting for the stationarity of the process the following transcendental equations are obtained (Ghanem and Spanos, 1991):

$$\begin{cases} c_e - \varphi \tan(\varphi l) = 0 \\ \text{and} \\ \varphi + c_e \tan(\varphi l) = 0 \end{cases} \quad (4.22)$$

where $c_e = 1/b_e$. If the solution of the second equation is φ^* , the eigenfunctions are:

$$f_i(t) = \frac{\cos(\varphi_i t)}{\sqrt{l + \sin(2\varphi_i l)/2\varphi_i}} \text{ for even } i \quad (4.23)$$

and

$$f_i^*(t) = \frac{\sin(\varphi_i^* t)}{\sqrt{l - \sin(2\varphi_i^* l)/2\varphi_i^*}} \text{ for odd } i \quad (4.24)$$

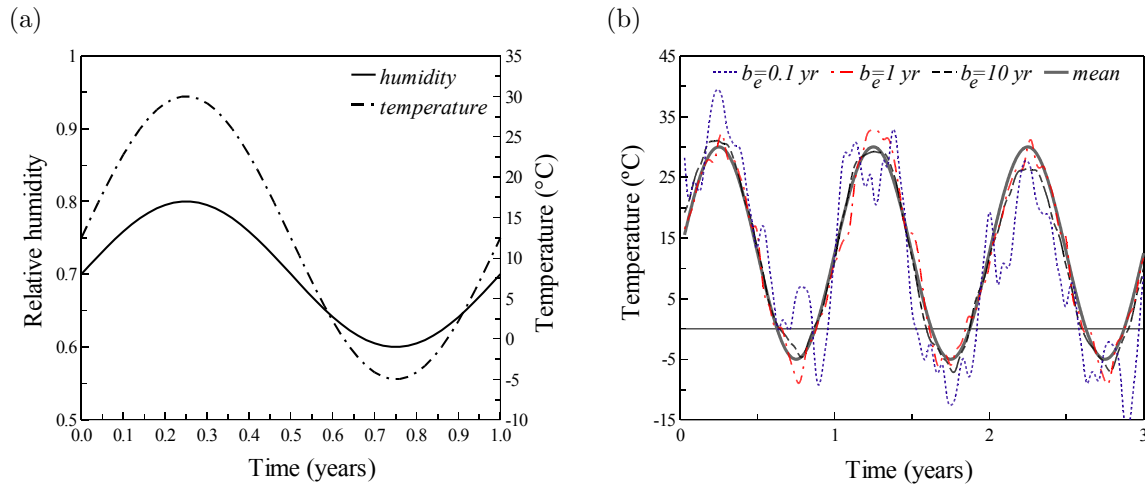


Figure 4.4: Modeling weather: (a) mean trends of temperature and humidity and (b) stochastic realizations for temperature.

The corresponding eigenvalues after solving equation 4.20 for these functions are:

$$\lambda_i = \frac{2c_e}{\varphi_i^2 + c_e^2} \text{ for even } i \quad (4.25)$$

and

$$\lambda_i^* = \frac{2c_e}{\varphi_i^{*2} l + c_e^2} \text{ for odd } i \quad (4.26)$$

where φ_i and φ_i^* are the solutions of the transcendental equations –i.e., equation 4.22.

In order to model the effect of seasonal variations of weather, the mean of the stochastic process $\bar{\kappa}_\phi(t)$ (equation 4.19), was modeled as a sinusoidal function (Figure 4.4a):

$$\bar{\kappa}_\phi(t) = \frac{\phi_{max} + \phi_{min}}{2} + \frac{\phi_{max} - \phi_{min}}{2} \sin(2\pi t) \quad (4.27)$$

where $\bar{\kappa}_\phi(t)$ represents temperature or humidity at time t , ϕ_{max} is the maximum temperature or humidity, ϕ_{min} is the minimum temperature or humidity and t is expressed in years. Daily variations can also be considered in the model for weather as a sinusoidal function. However, this study does not take the effect of daily variations into account due to the fact that the analyses focus on long-term performance of RC structures. In this approach, both the covariance and the correlation length of weather parameters can be determined based on real measurements. Figure 4.4b shows some realizations of the stochastic process representing temperature where $\phi_{max} = 30^\circ\text{C}$ and $\phi_{min} = -5^\circ\text{C}$; the correlation lengths are 0.1, 1 and 10 years; and the truncated discretization includes 30 terms ($n_{KL} = 30$). Note that smaller correlation lengths imply that the stochastic process is less correlated, and therefore, the corresponding stochastic process is far from the mean and extreme values are frequently observed.

4.4.2 Effect of global warming on weather

Weather measurements on global warming anticipate changes in the mean temperature and humidity in the coming years (IPCC, 2007). It has been found that eleven of the twelve years during the period 1995–2006 rank among the warmest years since the beginning of the instrumental record of global surface in 1850. Besides, the linear warming trend over the last 50 years (0.13°C per decade) almost doubles the measurements during the last 100 years (0.076°C). Based on these measurements and different policies against global warming, the Intergovernmental Panel on Climate Change has announced a rise in the mean temperature from 1 to 6.4°C over the next 100 years. The basic science of weather modeling, including the greenhouse effect, is well understood and has been widely discussed. Most of these models demand large computational efforts because they integrate dynamical and physical equations to describe the complete climate system (Houghton, 2005). Nowadays, about fifteen research centers in the world are running fully coupled models. Given the difficulties of integrating a comprehensive weather model with the chloride ingress phenomenon, a simplified model of global warming is presented in this section.

The effect of global warming is modeled by assuming that the increase or decrease of humidity and temperature over time, in the upcoming years, is a linear function. By denoting ϕ as the weather parameter (humidity or temperature), the annual mean value of ϕ is equal to (Figure 4.5):

$$\bar{\phi}(t) = \phi_0 + \left(\frac{\phi_{t_a} - \phi_0}{t_a} \right) t \quad (4.28)$$

where ϕ_0 and ϕ_{t_a} are the values of the annual means of ϕ at $t = 0$ and $t = t_a$, respectively. On the other hand, to make an optimal prediction of chloride ingress, it is also important to take into consideration the seasonal variations of humidity and temperature during the year (Figure 4.5). The model divides a reference year into two seasons hot and cold for temperature, and wet and dry for humidity. Actual forecasts of global warming also indicate that droughts increase the length of hot (or wet) seasons, L_h , with respect to the length of cold (or dry) seasons, L_c IPCC (2007). By defining R_0 as the normalized duration of the cold (or dry) season for $t = 0$, i.e. $R_0 = L_c / 1$ year, and R_{t_a} as the normalized duration of the cold or dry season for $t = t_a$ (L_c in years); it is possible to linearly estimate the normalized duration of the cold or dry season R for a given t :

$$R(t) = R_0 + \left(\frac{R_{t_a} - R_0}{t_a} \right) t \quad (4.29)$$

Thus by using a sinusoidal formulation to simulate the seasonal variation of ϕ around the linear trend (equation 4.28), the seasonal mean of ϕ considering global warming becomes (Figure 4.5):

$$\bar{\kappa}_\phi(t) = \begin{cases} \bar{\phi}(t) + \frac{\phi_{max} - \phi_{min}}{2} \sin\left(\frac{t - \lfloor t \rfloor}{1 - R(t)} \pi\right) & \text{for hot or wet seasons} \\ \bar{\phi}(t) - \frac{\phi_{max} - \phi_{min}}{2} \sin\left(\frac{t - \lfloor t \rfloor + R(t) - 1}{R(t)} \pi\right) & \text{for cold or dry seasons} \end{cases} \quad (4.30)$$

where ϕ_{max} and ϕ_{min} are respectively the maximum and minimum values taken by ϕ during one year, t is expressed in years and $\lfloor \cdot \rfloor$ represents the floor function -i.e., $\lfloor x \rfloor = \max\{n \in \mathbb{Z} \mid n \leq x\}$. The effect of global warming is integrated into the stochastic model of weather by substituting equation

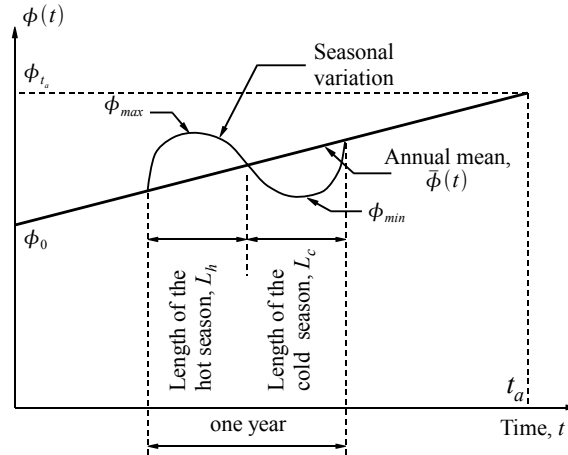


Figure 4.5: Mean of the weather model.

4.30 into equation 4.19.

4.5 Stochastic model for environmental chloride concentration

Chloride ions that ingress into the concrete can come from two sources: sea water or de-icing salts. This section presents the stochastic models used to simulate the chloride concentration in both environments.

4.5.1 Exposure to chlorides from sea water

In maritime environments, the environmental chloride concentration depends principally on the closeness to the sea, d . Based on a field study of 1158 bridges in Australia (McGee, 2000), the mean of the surface chloride concentration, $\mu_{C_{env}}$, can be computed as:

$$\mu_{C_{env}}(d) = \begin{cases} 2.95 & \text{for } d < 0.1 \\ 1.15 - 1.81 \log(d) & \text{for } 0.1 \leq d < 2.84 \\ 0.35 & \text{for } d > 2.84 \end{cases} \quad (4.31)$$

where d is expressed in km and $\mu_{C_{env}}$ in kg/m^3 . By taking equation 4.31 to define the mean, the stochastic process representing C_{env} is generated with uncorrelated log-normal fluctuations (noise). It is essential to precise that for both exposures (sea and de-icing salts) the models of surface chloride concentration represent *environmental* chloride concentrations and not *notional* surface concentrations (which appears from empirical models based on the solution of Fick's law) (Val and Trapper, 2008). Since there is no information available on the coefficient of variation (COV) for *environmental* chloride concentrations, the COV used herein is based on previous probabilistic studies which consider *notional* surface concentrations (Vu and Stewart, 2000; Duracrete, 2000). Figure 4.6a presents some realizations of C_{env} where the processes were generated by considering three mean values of $\mu_{C_{env}}$: 2.95, 1.15 and 0.35 kg/m^3 which correspond to $d < 0.1$, $d = 1$ and $d = 2.84$ km, respectively (equation 4.31); a COV of 0.20 was used for all these cases.

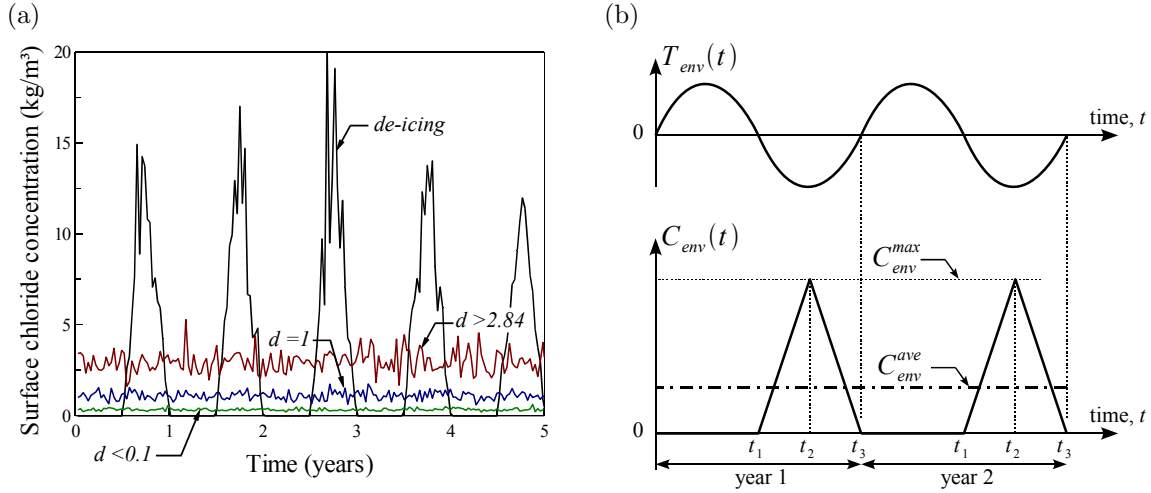


Figure 4.6: (a) Stochastic surface chloride concentrations. (b) Mean of the concentration of de-icing salts.

4.5.2 Exposure to chlorides from de-icing salts

Based on experimental measurements, the probabilistic models of exposure to de-icing salts in the literature usually assume that C_{env} remains constant all the time (Vu and Stewart, 2000; Duracrete, 2000). However, since the kinematics of chloride ingress change as function of weather conditions, a modified model for de-icing salts exposure is adopted. This model considers the increase of C_{env} during cold seasons. Thus, the proposed model assumes that during hot seasons the mean of chloride concentration at the surface is zero; and during cold seasons, it grows linearly from zero to the maximum, C_{env}^{max} , that corresponds to the minimum temperature, returning to zero at the beginning of hot seasons (Figure 4.6b):

$$\mu_{C_{env}}(t) = \begin{cases} 0 & \text{for } t < t_1 \\ C_{env}^{max}(t - t_1)/(t_2 - t_1) & \text{for } t_1 \leq t < t_2 \\ C_{env}^{max}[1 - (t - t_2)/(t_2 - t_1)] & \text{for } t_2 \leq t < t_3 \end{cases} \quad (4.32)$$

where t_1 , t_2 and t_3 are shown in Figure 4.6b. The value of C_{env}^{max} has been defined by considering that the quantity of chloride ions deposited during one year is the same as the average annual concentration reported in the literature, C_{env}^{ave} .

In the stochastic model for de-icing exposure $C_{env} = 0$ during hot seasons and becomes a log-normal variable during cold seasons. The time-variant mean used to generate the stochastic process is computed from equation 4.32. The COV was assumed to be in the range of $[0.2, 0.4]$ but actual data needs to be collected. An example of the stochastic modeling of C_{env} for de-icing exposure is also presented in Figure 4.6a. The maximum surface chloride concentration, C_{env}^{max} , was assumed to be 14 kg/m³. This value assures that the mean of the chloride ions deposited during a year is 3.5 kg/m³ which agrees with the data reported in (Vu and Stewart, 2000; Duracrete, 2000). A COV of 0.20 was used to generate the process shown in Figure 4.6a.

4.6 Fuzzy corrosion rate model

Modeling the behavior and the randomness of the corrosion rate after excessive cracking is difficult because i_{corr} depends on many factors (i.e., concrete electrical resistivity, oxygen and water availability). Given the complexity of the problem and the lack of experimental evidence, the use of a Sugeno type fuzzy inference system (FIS) has been proposed to implement a preliminary model. Appendix B presents a summary on fuzzy sets and fuzzy inference systems. This approach has the advantage that it includes the environmental aggressiveness in the assessment of i_{corr} after concrete cracking starts. FIS relates concrete ages with corrosion rates by taking into account:

1. an empirical model of corrosion rate which does not consider cracking or environmental aggressiveness (i.e. Vu and Stewart (2000)), and
2. the maximum corrosion rate for a given environment.

In the model, *concrete age* is represented by two membership functions. The first function is called *age of initial corrosion rate* and represents the age up to which RC remains undamaged, $\tilde{\mu}_{ini}$ (i.e., there is no corrosion or concrete cracking, Figure 4.7a):

$$\tilde{\mu}_{ini}(t) = \begin{cases} \exp\left(-\frac{1}{2} \left[\frac{t-t_{ini}}{\sigma_{ini}}\right]^2\right) & \text{for } t \geq t_{ini} \\ 0 & \text{otherwise} \end{cases} \quad (4.33)$$

where σ_{ini} is a shape parameter and t_{ini} the time to corrosion initiation. The second function is called *age of maximum corrosion rate*, which represents the age at which maximum possible corrosion rate can take place:

$$\tilde{\mu}_{max}(t) = \begin{cases} 0 & \text{for } t_{sc} \geq t \\ m_f(t - t_{sc}) & \text{for } \frac{1}{m_f} + t_{sc} \geq t > t_{sc} \\ 1 & \text{for } t > \frac{1}{m_f} + t_{sc} \end{cases} \quad (4.34)$$

where t_{sc} represents the time to severe concrete cracking and m_f is a shape parameter representing the slope of $\tilde{\mu}_{max}$ (Figure 4.7a). In equations 4.33 and 4.34, the values of the shape parameters σ_{ini} and m_f should be obtained based on experimental data and/or experts' knowledge. In the age represented by μ_{ini} , the initial corrosion rate, i_{ini} (in $\mu\text{A}/\text{cm}^2$), is obtained from the following empirical relationship (Vu and Stewart, 2000):

$$i_{ini}(t) = \begin{cases} \frac{37.8(1-w/c)^{-1.64}}{c_t} & \text{for } t_{ini} + 1 \text{ year} \geq t > t_{ini} \\ \frac{32.13(1-w/c)^{-1.64}}{c_t} (t - t_{ini})^{-0.3} & \text{for } t > t_{ini} + 1 \text{ year} \end{cases} \quad (4.35)$$

where the cover thickness, c_t , is given in cm. It is important to mention that equation 4.35 is valid when the structure is located in an environment with relative humidity of 75% and temperature of 20°C. For the age represented by $\tilde{\mu}_{max}$, the maximum corrosion rate, i_{max} , depends mainly on environmental aggressiveness. Its value is obtained from specific environmental conditions e.g. availability of chlorides, CO₂, sulfates, oxygen and water in the atmospheric environment. The maximum corrosion rates for

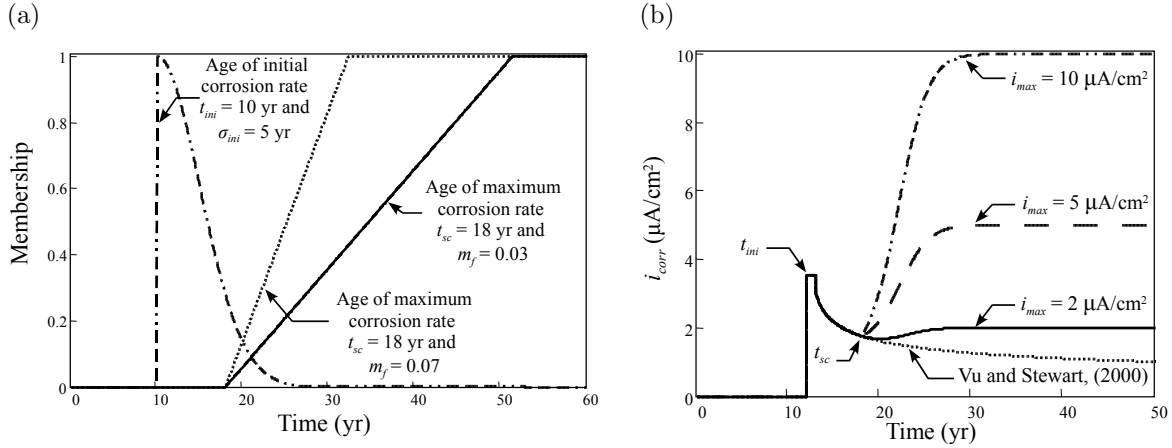


Figure 4.7: Examples of: (a) the age membership functions; and (b) the time-variant corrosion rate function.

various environments with various levels of aggressiveness are suggested by EN 206 (Geocisa and the Torroja Institute, 2002). For instance, if the structure is located in a tidal zone $i_{max} \approx 8 \mu\text{A}/\text{cm}^2$.

The rules used by FIS are:

$$\begin{cases} \text{if concrete age is } \tilde{\mu}_{ini}(t) & \text{then } i_{corr} = i_{ini}(t) \\ \text{if concrete age is } \tilde{\mu}_{max}(t) & \text{then } i_{corr} = i_{max} \end{cases} \quad (4.36)$$

Based on these rules, the proposed time-variant corrosion rate, i_{corr}^{fuzzy} is computed from the following relationship:

$$i_{corr}^{fuzzy}(t) = \frac{\tilde{\mu}_{ini}(t)i_{ini}(t) + \tilde{\mu}_{max}(t)i_{max}}{\tilde{\mu}_{ini}(t) + \tilde{\mu}_{max}(t)} \quad (4.37)$$

Figure 4.7b presents some examples of fuzzy corrosion rate functions. Note that the corrosion rates follow the empirical relationship during the years after corrosion initiation and approach the maximum corrosion rate after the time to severe cracking. The advantage of this fuzzy approach is that the corrosion rate can be estimated based on local conditions, experts' knowledge and empirical models or observations. For example, for a given site, an expert can define the shape of the membership functions or the value of the threshold corrosion rate taking into account his/her knowledge about concrete quality, material properties, environmental aggressiveness, RC behavior in similar conditions, etc. Finally it is important to clarify that these functions can be permanently updated based on field measurements and experimental data.

Figure 4.8 compares four models of corrosion rate. In the first model, the time-variant corrosion rate has been computed by using the relationship proposed by Vu and Stewart (2000). In this model, the corrosion rate remains constant during the first year, after which, the formation of rust products on the steel surface reduces this rate substantially. The second model (Liang et al., 2005) considers a reduction of corrosion rate, from the corrosion initiation time, (t_{ini}) until the time of full corrosion, (t_w). After this point, the corrosion rate remains constant. In the third case, the model includes concrete cracking and assumes that the change of the diffusion coefficient of concrete begins only after

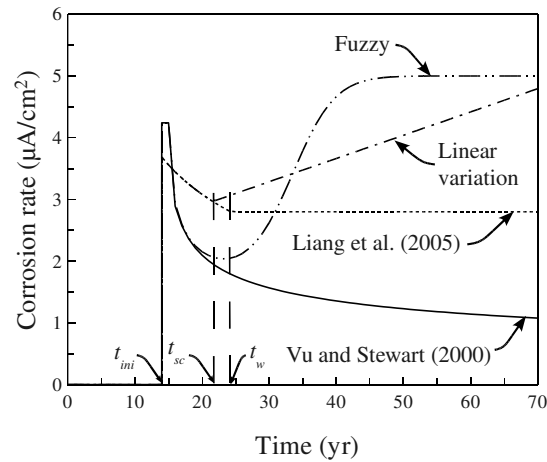


Figure 4.8: Time-dependent corrosion rates models.

the time to severe cracking, (t_{sc}). After this time, diffusion grows due to the increase in the oxygen diffusion coefficient (section 3.3.3). The last model is similar to the previous one but the kinematics of the corrosion rate after t_{sc} is controlled by a fuzzy relationship. The first two models presented in Figure 4.8 do not take into account concrete cracking to estimate corrosion rate, while the last two do. In this thesis the last model was used to compute corrosion rate because it takes into account environmental aggressiveness.

4.7 Summary and conclusions

This chapter presented the stochastic deterioration model for the corrosion-fatigue deterioration process.

The conclusions of this chapter are presented as follows:

1. The uncertainties for the corrosion-fatigue deterioration process come from three sources: (1) material properties, (2) models and their parameters, and (3) environmental actions. These sources have been classified into two categories: randomness and fuzziness. While randomness is treated under a classical probabilistic approach, fuzziness uses fuzzy sets.
2. There are two quantities of interest in the reliability analysis: probability of corrosion initiation and probability of failure. Each quantity is estimated by evaluating the limit state functions corresponding to the serviceability and ultimate limit states, respectively. Depending on the targets of the analysis, both limit state functions can be useful for reliability assessment or for maintenance/repair management.
3. This chapter adopted and proposed models for the random/fuzzy variables. The time-invariant random variables were modeled by classical distributions (Normal, Log-normal, Beta, etc.), where their statistical parameters were defined based on other deterministic and probabilistic studies. The time-variant random variables were represented by stochastic processes. The weather model,

for humidity and temperature, accounted for the effects of seasonal variations and global warming. For the environmental chloride concentration, the stochastic processes distinguish between exposure to de-icing salts or to the sea. Given both the lack of experimental evidence and the complexity of the corrosion rate, the proposed model implements a fuzzy inference system. This fuzzy model is based on fuzzy rules and a deterministic model and considers the environmental aggressiveness when concrete cracking starts.

4. Taking into account the complexity of the system (deterioration model, random and fuzzy variables), Monte Carlo simulation and Latin Hypercube sampling will be used for the reliability analysis. Since the deterioration phenomenon depends on time, the chosen reliability method allows for the consideration that the input random variables and the response of the system are time-dependent.

CHAPTER 5

NUMERICAL APPLICATIONS

5.1 Introduction

The proposed model presented in previous chapters can be used to (1) improve knowledge about the deterioration phenomenon, (2) optimize the design and/or the schedule of interventions (e.g., inspection/maintenance); and (3) evaluate the reliability of existing RC structures. Therefore, the numerical formulation of the model described in chapter 3 as well as the methodology for the reliability analysis presented in chapter 4 were implemented in a program written in Fortran 95. This chapter presents various practical applications to illustrate the benefits of the model and to evaluate the sensitivity of the parameters.

The objectives of this chapter are:

1. to study the kinematics of the proposed model and to analyze the sensitivity of the model regarding the system parameters;
2. to evaluate the probabilities of corrosion initiation and failure for RC structures; and
3. to estimate the lifetime reduction caused by the combined action of corrosion and fatigue.

Given the complexity of the problem and in order to study each stage of the deterioration phenomenon more consciously, this chapter presents five examples. The first example presents a deterministic analysis of chloride penetration on a RC wall (section 5.2). The second example uses a probabilistic approach to perform a sensitivity study of the chloride penetration model on RC members as walls and columns (section 5.3). The third example studies the influence of real exposure conditions, including global warming, on a RC wall (section 5.4). The fourth example focuses on the deterioration process caused by corrosion-fatigue on a RC bridge girder (section 5.5). Finally, the last example integrates realistic environmental exposure conditions to the model of corrosion-fatigue to evaluate the failure probability of a RC bridge girder (section 5.6).

5.2 Case study 1: Deterministic assessment of chloride ingress

5.2.1 Problem description

This example is aimed at studying the influence of realistic weather conditions on the kinematics of chloride penetration in RC slabs or walls. To simplify the analysis, the flow of chlorides is assumed to

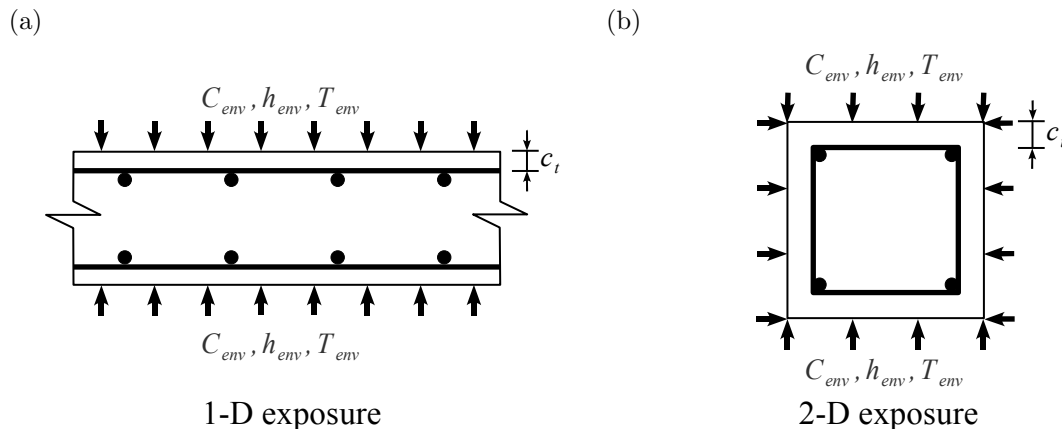


Figure 5.1: Cross-sections of the studied RC members: (a) slab or wall and (b) column or beam.

Table 5.1: Values used in the deterministic study.

Chloride transport		Moisture diffusion		Heat transfer	
Variable	Value	Variable	Value	Variable	Value
C_{env}^{max}	16 kg/m ³	h_{min}	0.6	T_{min}	-5 °C
$D_{c,ref}$	3×10^{-11} m ² /s	h_{max}	0.8	T_{max}	30 °C
U_c	41.8 kJ/mol	$D_{h,ref}$	3×10^{-10} m ² /s	λ	1.4 W/(m °C)
B_c	1 m/s	α_0	0.05	c_q	1000 J/(kg °C)
m_c	0.15	n	10	B_T	7.75 W/(m ² °C)
		U	25 kJ/mol		
		B_h	3×10^{-7} m/s		

occur only in one-dimension (e.g., Figure 5.1a), the RC slab or wall is exposed to de-icing salts and the Langmuir isotherm was used to account for the binding effect.

The evolution of environmental parameters (temperature, humidity and environmental chloride concentration) is modeled by deterministic functions which can be considered as mean trends (sections 4.4 and 4.5). The temperature and humidity models used in this example consider seasonal effects where the minimum and maximum values of humidity and temperature as well as the other constants used in the example are defined in Table 5.1. However, since the kinematics of the chloride ingress changes as function of weather conditions, the modified model for de-icing salts exposure described in section 4.5 is adopted in this example. This model considers that during the hot seasons the chloride concentration at the surface is zero, whereas during the cold seasons it becomes time-variant. For this example the value of C_{env}^{max} presented in Table 5.1 entails that an average surface concentration of $C_{env}^{ave} = 4$ kg/m³ is applied during a year (Vu and Stewart, 2000; Duracrete, 2000).

Other general assumptions for this example are summarized as follows:

- the concentration of chlorides inside the concrete is zero at the beginning of the analysis;
- the structure is located in a partially-saturated environment;
- the concrete contains 400 kg/m³ of Ordinary Portland Cement (OPC) with 8% of C₃A and $w/c = 0.5$;

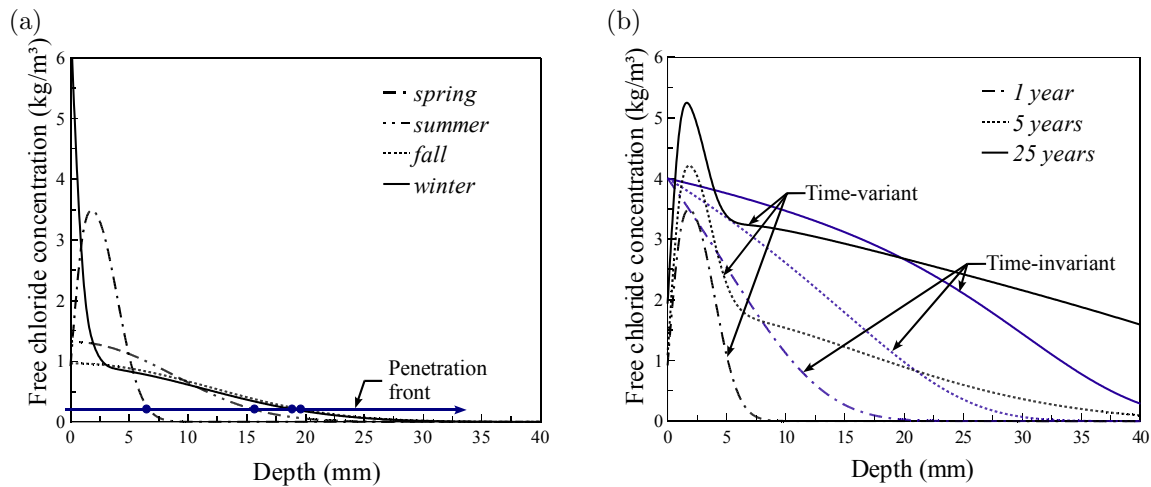


Figure 5.2: Profiles of free chlorides for: (a) different seasons after one year of exposure, (b) the middle of spring and various times of exposure.

- the constants of the isotherms are $\alpha_L = 0.1185$, $\beta_L = 0.09$ (Tang and Nilsson, 1993; Glass and Buenfeld, 2000);
- the curing period, t_e , is 28 days; and
- the finite difference weighting factor is 0.8, and the relaxation factor is 0.9 for the numerical solution of Fick's diffusion law.

The assumptions mentioned above were also considered for all the examples presented in this chapter unless otherwise specified.

5.2.2 Results

Figure 5.2a depicts the profiles of chlorides for different seasons after one year of exposure. The analysis begins at the end of exposure to chlorides (middle of spring) and ends when $C_{env}(t)$ is maximum (middle of winter). The *penetration front* represents the depth at which a given chloride concentration is observed. Figure 5.2a show the advance of the penetration front for a chloride concentration of 0.20 kg/m^3 . Although de-icing salts are not applied during spring, summer and fall, the penetration front advances towards the reinforcement. Chloride ingress is more appreciable from spring to summer (from 7 to 16 mm) than from summer to fall (from 16 to 18.5 mm) because chloride diffusivity increases for higher temperatures and humidities (see equations 3.10 and 3.12). It can also be observed that during winter the chloride concentration tends to C_{env}^{max} at the exposed surface.

Given that the shape of the chloride profiles depends on the season, Figure 5.2b presents the profiles after 1, 5 and 25 years of exposure at the middle of spring. These profiles were calculated for two types of environmental actions: *time-variant* and *time-invariant*. In the former, temperature, humidity and surface chloride concentration consider seasonal effects. In the latter, all the environmental variables are considered constants –i.e., $C_{env}^{ave} = 4 \text{ kg/m}^3$, $T_{env} = 12.5 \text{ }^\circ\text{C}$ and $h_{env} = 0.7$. Note that there is a large increase in the penetration depth from 1 to 5 years in both cases. Nevertheless, the rate

Table 5.2: Probabilistic models of the random variables.

Physical problem	Variable	Mean	COV	Distribution
<i>Chloride ingress</i>	$D_{c,ref}$	$3 \times 10^{-11} \text{ m}^2/\text{s}$	0.20	log-normal
	C_{th}	0.5 wt% cement	0.20	normal
	c_t	nominal	0.25	normal ^a
	U_c	41.8 kJ/mol	0.10	beta on [32,44.6]
	m_c	0.15	0.30	beta on [0,1]
<i>Moisture diffusion</i>	$D_{h,ref}$	$3 \times 10^{-10} \text{ m}^2/\text{s}$	0.20	log-normal
	α_0	0.05	0.20	beta on [0.025,0.1]
	n	11	0.10	beta on [6,16]
<i>Heat transfer</i>	λ	2.5 W/(m °C)	0.20	beta on [1.4,3.6]
	ρ_c	2400 kg/m ³	0.20	normal
	c_q	1000 J/(kg °C)	0.10	beta on [840,1170]

^atruncated at 10 mm (lower bound)

of chloride ingress decreases from 5 to 25 years. This reduction is due mainly to the decrease of chloride diffusivity with time –i.e., equation 3.11. If the cover thickness is $c_t = 4$ cm, the time-variant model gives greater concentrations at c_t for all exposures higher than 5 yr. This result is due to the acceleration of chloride penetration during hot and wet seasons. This analysis confirms that transfer mechanisms are very sensitive to environmental actions.

5.3 Case study 2: Probabilistic analysis of the time to corrosion initiation

5.3.1 Problem description

The main goal for this example is to study the influence of chloride binding, weather conditions, concrete aging, convection, correlation length and two-dimensional chloride ingress on the probability of corrosion initiation. Figure 5.1 shows the studied RC wall and column. This application accounts for continental weather with structures placed at moderate latitudes (e.g., European countries) and far from the ocean where the source of chlorides come only from de-icing salts. The values for the weather model (h_{max} , h_{min} , T_{max} and T_{min}) are presented in Table 5.1 and the probabilistic models used in this study are shown in Table 5.2. The cover thickness is modeled by a normal distribution truncated at 10 mm and its mean is set as $\mu c_t = 40\text{mm}$ with a COV=0.25.

Other general assumptions concerning the probabilistic model are:

- the truncated Karhunen-Loève expansion includes 30 terms –i.e., $n_{KL} = 30$;
- the range of each random variable is divided into 10 equally probable intervals for the Latin Hypercube sampling; and
- the random variables are independent.

5.3.2 Results

For all the cases studied, and according to Lounis (2005), the results of Monte Carlo simulation indicate that the time to corrosion initiation is log-normally distributed. The test of Kolmogorov-Smirnov (K-S) with a significance level of 5% was used as selection criterion.

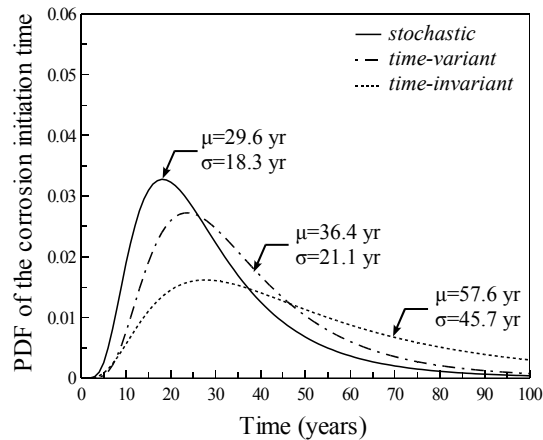


Figure 5.3: Impact of type of weather model.

Figure 5.3 depicts the influence of the type of weather model –i.e., time-invariant, time-variant and stochastic, on the PDF of the corrosion initiation time. For the time-invariant case the annual temperature and relative humidity were set to 12.5°C and 0.7, respectively. Such values correspond to the annual mean of the time-variant model. The time-variant case accounts for the sinusoidal variation of temperature and humidity with the parameters presented in Table 5.1. The stochastic case considers that the mean is defined by the time-variant model with correlation length of 0.1 year (sections 4.4 and 4.5). It should be noted that the mean and standard deviation of the corrosion initiation time decrease when both the seasonal variations and the randomness of humidity and temperature are considered. Taking as a reference the mean obtained from the stochastic analysis, it is observed that the mean of the corrosion initiation time increases by 23% and 94% for the time-variant and time-invariant models, respectively. This increment is expected because, as shown in Figure 5.2b, accounting for the seasonal variation of humidity and temperature (time-variant model) reduces the corrosion initiation time. The reduction is more appreciable when the time-variant model is coupled with a stochastic process, for which there are extreme values that accelerate the chloride penetration. Given that actual structures are subjected to random environmental actions, these results highlight the importance of including comprehensive probabilistic models of weather conditions in the chloride ingress assessment.

The effect of chloride binding and the type of isotherm on the PDF of the corrosion initiation time is shown in Figure 5.4a. This analysis considers temperature and humidity as stochastic processes with a correlation length of 0.1 year. The constants for the Freundlich isotherm are $\alpha_F = 0.256$, $\beta_F = 0.397$ (Tang and Nilsson, 1993; Glass and Buenfeld, 2000). As expected, the results indicate that ignoring the effect of binding overestimates the mean of the corrosion initiation time. This behavior seems reasonable because when binding is not considered, it is assumed that all the chlorides involved in the flow (bound and free) ingress into the concrete matrix simultaneously, and therefore, the time to corrosion initiation occurs earlier. No significant difference was observed between both Langmuir and Freundlich isotherms. This similarity lies in the fact that the constants for both isotherms were determined for concrete with identical characteristics. This suggests that for this type of studies, no improvement in this direction is needed.

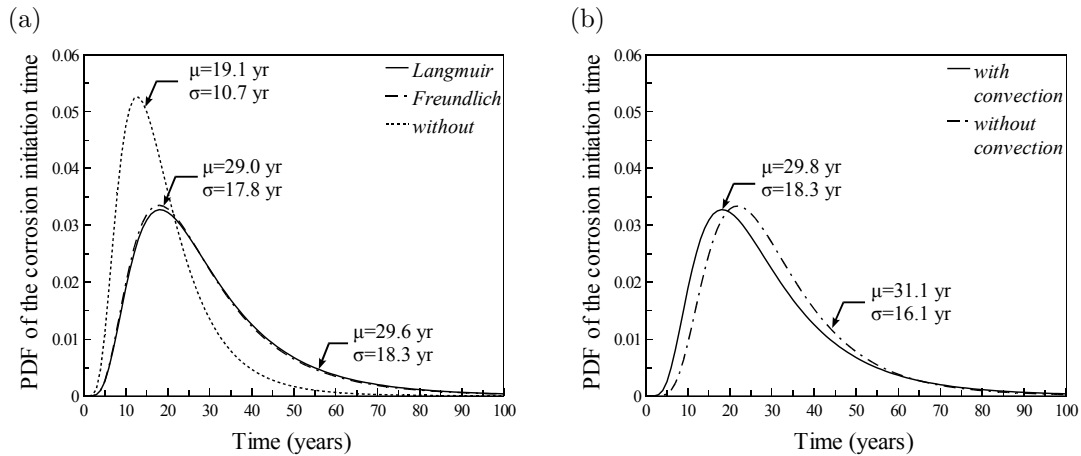


Figure 5.4: Effect of (a) binding and type of isotherm and (b) convection.

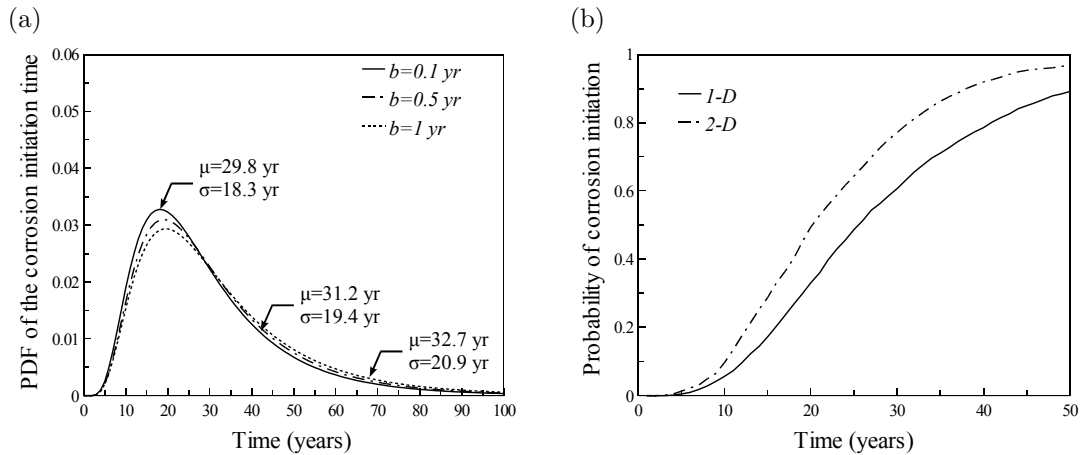


Figure 5.5: (a) Influence of the correlation length b . (b) Probability of corrosion initiation for 1-D and 2-D exposures.

The impact of convection on the PDF of the corrosion initiation time is plotted in Figure 5.4b. These PDFs were obtained for Langmuir isotherm, correlation length of 0.1 year, and by modeling the environmental actions stochastically. It can be noted from Figure 5.4b that accounting for the chloride ingress by convection slightly decreases the mean of the corrosion initiation time. This reduction is due to the addition of a second mechanism of chloride ingress (i.e., convection) which augments the chloride concentration at the corrosion cell reducing the time to achieve the threshold concentration.

Figure 5.5a describes the influence of the correlation length b on the probability of corrosion initiation. For this study, correlation lengths of 0.1, 0.5 and 1 year, have been compared. Although this value should be determined based on real measurements of temperature and humidity, the results indicate that its influence on the mean and standard deviation of the probability of corrosion initiation is not significant. Moreover, it is noticed that smaller values of b lead to conservative results. This behavior is expected because small values of b entail the presence of extreme values that accelerate the

Table 5.3: Description of the studied environments.

Climate	Description	Temperature		Humidity		μC_{env}
		T_{min}	T_{max}	h_{min}	h_{max}	
<i>Continental</i>	places located at middle latitudes far from the ocean.	-10°C	20°C	0.6	0.8	Eq. 4.32
<i>Oceanic</i>	structures placed at middle latitudes close to the ocean.	5°C	25°C	0.6	0.8	Eq. 4.31
<i>Tropical</i>	sites emplaced at equatorial latitudes close to the ocean.	20°C	30°C	0.7	0.9	Eq. 4.31

process of chloride ingress.

Finally, the variation of the probability of corrosion initiation for 1-D and 2-D exposures is shown in Figure 5.5b. Both cases include the probabilistic nature of environmental actions, chloride ingress by convection, chloride binding and a correlation length of 0.1 years. As expected, higher probabilities correspond to 2-D exposure. The reduction of corrosion initiation time is due to the exposure to chlorides on both sides of the structural element. For instance, for 30 years of exposure the probability of failure is increased 27% when 2-D exposure is considered. These results stress the importance of including a two-dimensional analysis for correct prediction of corrosion initiation in small RC members such as columns and beams.

5.4 Case study 3: Influence of global warming on corrosion initiation time

5.4.1 Problem description

The main goal of this example is to study the influence of real weather conditions on both the probability of corrosion initiation and lifetime reduction. Towards this aim, let us consider a RC slab or wall, with one side exposed to environmental actions (Figure 5.1a). Knowing that the depth of the RC member is much smaller than its other dimensions, the problem is reduced to one-dimensional flow of chlorides into concrete. However, it is important to highlight that for smaller members (e.g., columns or beams) the two-dimensional flow accelerates the probability of corrosion initiation for the corner bars –i.e., Figure 5.5b. The probabilistic models for the random variables are defined in Table 5.2. The cover thickness follows a normal distribution truncated at 10 mm with the following statistical parameters: $\mu c_t = 50\text{mm}$, and $\text{COV}=0.25$.

This application accounts for three environments with the characteristics defined by both latitude and closeness to the sea. Table 5.3 presents the values adopted for each case. For the continental environment, chloride concentration is $C_{env}^{max} = 14 \text{ kg/m}^3$, and for the marine environment, it depends on the distance from the sea.

To account for the effect of global warming, three possible scenarios were defined (Table 5.4). The characteristics of these scenarios were assigned based on the forecasts given by the Intergovernmental Panel on Climate Change IPCC (2007); which, in the author’s opinion, presents the most compendious study on global warming. These predictions account for a combination of natural and anthropogenic driving forces. The action of natural forcings refers to natural climate changes due mainly to solar and volcanic activities. Anthropogenic forcings encompass the effect of human perturbations on climate.

Table 5.4: Parameters used to simulate global warming.

Scenario	Characteristics	ΔT_a	Δh_a	ΔR_a
<i>Without</i>	climate change is neglected	0°C	0	0
<i>Expected</i>	use of alternative and fossil sources of energy, birthrates follow the current patterns and there is no extensive use of clean technologies.	2.5°C	0.05	-0.1
<i>Pessimistic</i>	vast utilization of fossil sources of energy, appreciable growth of population and there are no policies to develop and extend the use of clean technologies.	6.5°C	0.10	-0.2

Among the anthropogenic forcings, the most important factors considered in such studies are:

- carbon dioxide, methane, nitrous oxide emissions;
- global population growth;
- introduction of new and clean technologies leading to the reduction of the impact of climatic change and
- use of fossil sources of energy.

Consequently, the three possible scenarios are *without*, *expected* and *pessimistic* global warming. Each scenario is defined in terms of (section 4.4):

- the difference between the annual means of temperature for the initial year t_0 and the year of the end of the forecast t_a , $\Delta T_a = T_{t_a} - T_{t_0}$,
- the difference between the annual mean of relative humidity for t_0 and t_a , $\Delta h_a = h_{t_a} - h_{t_0}$, and
- the difference between the normalized durations of the cold seasons for t_0 and t_a , $\Delta R_a = R_{t_a} - R_{t_0}$.

By taking as reference a period of analysis of 100 years –i.e., $t_a = 100$ years, the features and the values of ΔT_a , Δh_a and ΔR_a for each scenario are presented in Table 5.4. Figure 5.6 shows an example of the temperature model including the effects of global warming. For seasonal variation, the temperature fluctuates between $T_{min} = -10^\circ\text{C}$ and $T_{max} = 20^\circ\text{C}$ for a year. Taking into consideration all scenarios of global warming described in Table 5.4, the impact of climate changes at the end of the reference period is easily observable in Figure 5.6. Specifically, the length of cold seasons has decreased –i.e., $R_0 > R_{t_a}$, and temperatures during the whole year are higher. This difference is emphasized in the pessimistic scenario.

5.4.2 Results

For a better understanding of the effects of global warming on RC structures under real weather conditions, this section distinguishes between two main issues:

- the probability of corrosion initiation without climate changes, and
- the lifetime reduction induced by global warming.

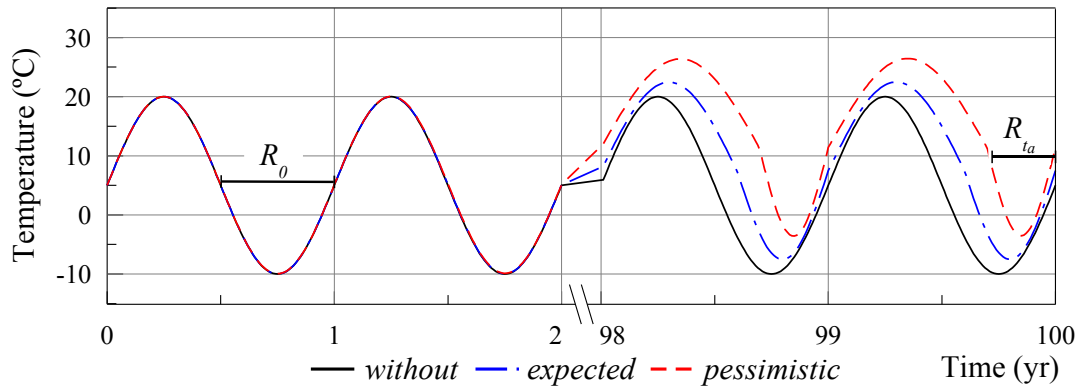


Figure 5.6: Example of the temperature model including global warming.

The results presented herein also account for: the stochastic model of humidity and temperature, chloride binding (Langmuir isotherm) and convection.

5.4.2.1 Probability of corrosion initiation without climate changes

The aim of this analysis is to perform a comprehensive study of the influence of weather conditions without considering climate change repercussions. This study discusses the effects of:

- three different *environmental exposures* (continental, tropical and oceanic) and
- the *distance to the sea* d (less than 100 m, around 1 km or more than 3 km) for marine environments.

The effect of the type of environmental exposure on the probability of corrosion initiation is plotted in Figure 5.7a. This Figure presents the probabilities of corrosion initiation for the environments described in Table 5.3. The surface chloride concentration for the marine environment (tropical or oceanic), is defined by a distance to the sea $d < 0.1\text{km}$. It is observed that the highest probabilities of corrosion initiation p_{corr} correspond to marine environments, in particular, for the tropical environment. These results are explained by the fact that (1) structures placed in marine environments are exposed to chlorides all the time and (2) high temperature and humidity accelerate the penetration of chloride ions inside the concrete matrix. The difference between continental and tropical environments highlights the importance of implementing a chloride penetration model that includes environmental effects. Given that the environmental chloride concentration is the same for both marine environments (e.g., tropical and oceanic), a simplified analysis would lead to the same results for both environments when climatic considerations are not taken into account.

Figure 5.7b describes the influence of the distance from the sea on the probability of corrosion initiation. These profiles were computed for oceanic and tropical environments. It is observed that the probability of corrosion initiation is higher for the locations close to the sea. This behavior is due to the increase of the environmental chloride concentration. The impact of the distance to the sea can be observed by analyzing the results for a lifespan of 30 years for the oceanic environment. In

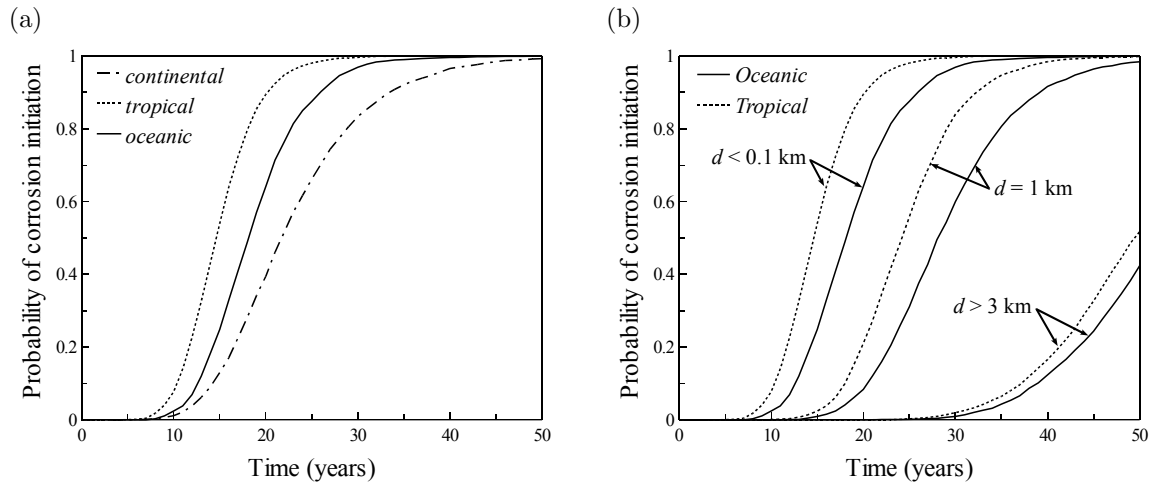


Figure 5.7: (a) Effect of type of exposure. (b) Influence of the distance to the sea.

this case the probabilities of corrosion initiation change from 0.01 to 0.99 when the distance to the sea is reduced from $d = 3$ km to $d < 0.1$ km, respectively. These differences justify the importance of including d in the life-cycle analysis. It can also be noted from Figure 5.7b that for all locations, the probability of corrosion initiation is higher for tropical environments. Although the chloride surface concentrations for both environments are the same, given that tropical environments are characterized by larger values of temperature and humidity, the time to corrosion initiation is reduced.

5.4.2.2 Lifetime reduction induced by global warming

The objective of this subsection is to study the influence of global warming on lifetime reduction under different environmental exposures and climate change scenarios. The results reported herein are expressed in terms of *critical time* which is defined as the time to reach 95% of the probability of corrosion initiation p_{corr} . The following aspects are discussed:

- the combined effect of the type of weather model (mean trend or stochastic) and climate changes on the critical times (for the continental environment and all the scenarios);
- the influence of global warming on the probability of corrosion initiation (for the oceanic environment and all the scenarios); and
- the effect of global warming on the critical times and the lifetime reduction (for all environments and scenarios).

Figure 5.8a shows the influence of the weather model on the critical times for the different global warming scenarios and the continental environment. The following cases of weather modeling are compared: (1) only the mean trend is considered; and (2) a stochastic variation is added. In all three scenarios accounting for the randomness associated with weather reduces the critical times. By comparing both results (stochastic and mean trend) it is observed that this reduction is about 20% for all scenarios (see Figure 5.8b). This difference is explained by the presence of extreme values of

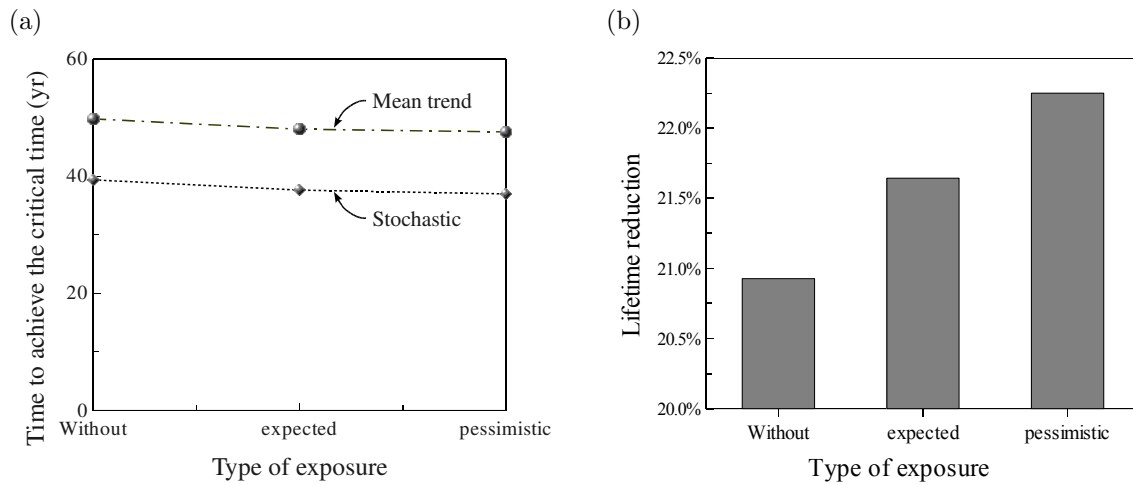


Figure 5.8: Comparison between weather models: (a) time to achieve the 95% of p_{corr} , (b) lifetime reduction.

temperature and humidity for the stochastic model that influences the chloride penetration process. Since these extreme values have been observed during real exposure conditions, these results justify the consideration of the randomness inherent to the phenomenon for a better lifetime assessment. It can be also noticed that the largest lifetime reductions correspond to the expected and pessimistic scenarios (Figure 5.8b). Although the difference is not important (from 20.9 to 22.3%), this behavior is principally due to the increase of temperatures and humidities induced by global warming that reduces the time to corrosion initiation.

The effect of global warming on the probability of corrosion initiation is presented in Figure 5.9. The curves plotted in this figure correspond to the oceanic environment for all the considered locations. Overall behavior indicates that global warming increases the probability of corrosion initiation, particularly, for the pessimistic scenario. This increase is explained by the acceleration of the chloride flow induced by global warming which raises temperature and humidity as well as the length of the hot and wet periods. It can also be noted that the lifetime reduction induced by global warming is more significant for structures located far from the sea. Since the corrosion initiation time is shorter for higher surface chloride concentrations, the effect of global warming is less appreciable in this case. This means that in structures near the sea, the process is completely dominated by high chloride concentrations at the surface and rarely influenced by climatic changes.

Figure 5.10a presents the critical times for all environments considered and distances from the sea. It is observed that shorter critical times correspond to marine environments closer to the sea. The difference between critical times for scenarios without and with global warming increases when the distance to the sea is greater. These results confirm that structures far from the ocean are more susceptible to global warming in terms of reduction of critical time. For instance, global warming can reduce the critical times from 6 to 14 years for structures located at 3 km away from the seashore while this reduction is only from 1 to 3 years for $d < 0.1$ km. By comparing both marine environments, it can also be noted that the impact of global warming is more important for oceanic environments where the chloride ingress process is more sensitive to climatic changes.

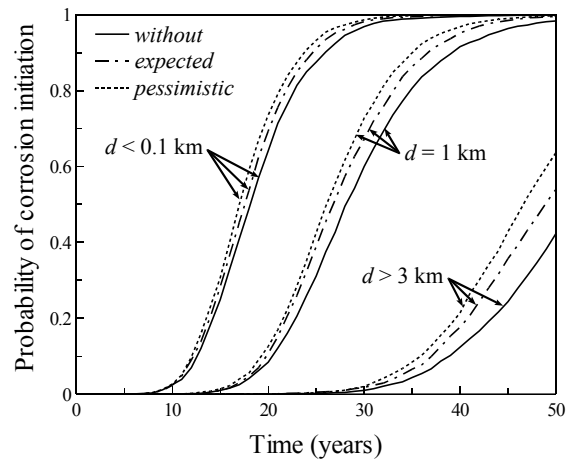


Figure 5.9: Effect of global warming for the oceanic environment.

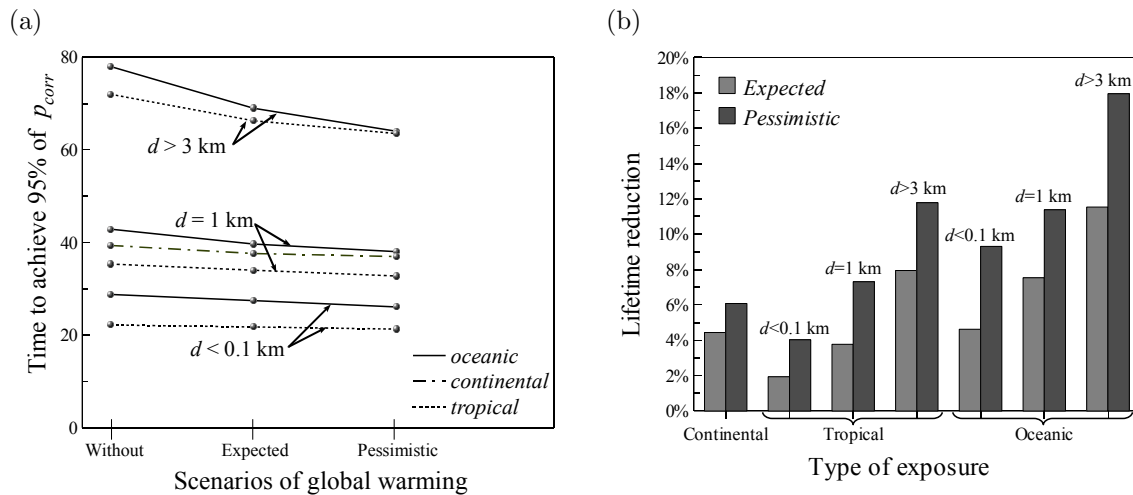


Figure 5.10: (a) Time to achieve the 95% of p_{corr} . (b) Lifetime reduction induced by global warming.

Results can also be analyzed by computing the percentage of lifetime reduction taking as reference the case without global warming (Figure 5.10b). From these results it is observed that global warming induces lifetime reductions from 2 to 12% for the *expected* scenario and from 4 to 18% for the *pessimistic* scenario. By comparing the average lifetime reduction for all the environments, the larger influence corresponds to the oceanic environment (10.4%) followed by tropical environment (6.1%) and finally the continental environment (5.3%). These results justify the implementation of countermeasures directed at: (1) reducing and/or mitigating the action of global warming on weather and (2) minimizing the impact of climate changes on RC structures. These countermeasures should be adopted in function of specific features of the structure such as type of environment and location.

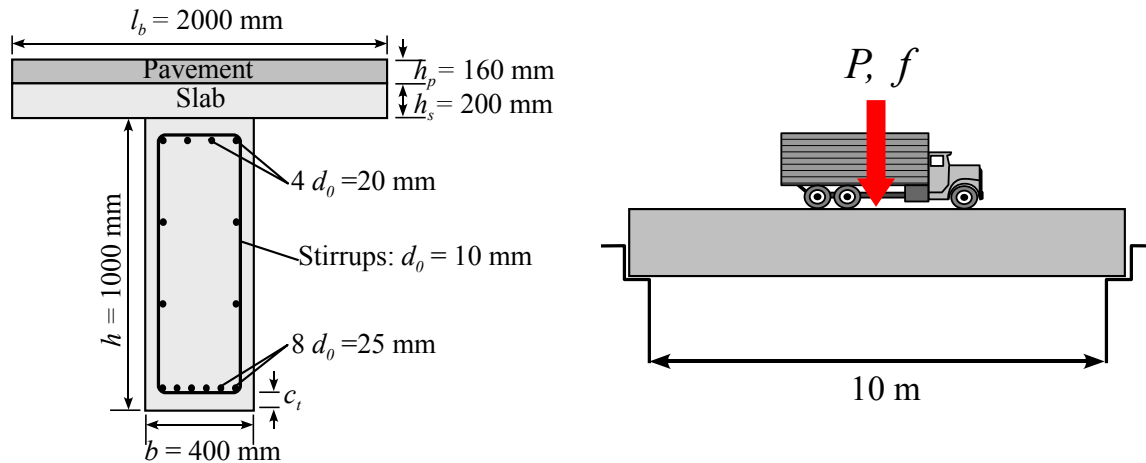


Figure 5.11: Configuration of bridge girder.

Table 5.5: Design load and material constants.

Variable	Value	Description
P_k	150 kN	Characteristic punctual design load
E_{st}	200000 MPa	Elastic modulus of steel
$f_{c_k}^t$	30 MPa	Characteristic concrete compression strength
f_{y_k}	500 MPa	Characteristic steel strength
γ_c	22 kN/m ³	Specific weight of concrete
γ_p	18 kN/m ³	Specific weight of pavement
ν_c	0.2	Concrete Poisson ratio
ρ_{st}	8000 kg/m ³	Density of steel
ρ_c	2900 kg/m ³	Density of cement
ρ_a	2600 kg/m ³	Density of aggregate
a/c	5.14	Aggregate-to-cement ratio

5.5 Case study 4: Corrosion-fatigue action in saturated environments

5.5.1 RC girder and basic considerations

This section presents an application describing the combined effect of corrosion-fatigue in a simply supported RC bridge girder subjected to cyclic loading (e.g. traffic). The span of the girder is 10m with the geometrical characteristics of the cross-section and the steel reinforcement shown in Figure 5.11. The girder has been designed according to the European standard (2004). In addition to the dead load, a truck wheel load is applied on the girder. The design load, P_k , corresponds to a wheel load located in the middle of the span (Figure 5.11). Table 5.5 presents the load and the material properties used in the design and the analysis.

The effect of environmental aggressiveness on structural reliability, is considered by accounting for four levels of aggressiveness (Table 5.6). Each level is characterized by: (1) a chloride surface concentration, C_s , (2) an expected threshold corrosion rate, i_{th} , and (3) a concrete cover, c_t . The analytical solution to Fick's diffusion law is implemented in this example. The chloride surface concentration is treated as a random variable for which the mean depends on the proximity to the sea and is computed based on the study of McGee (2000). The expected threshold values of the corrosion rate are

Table 5.6: Description of the studied environments.

Level of aggressiveness	Description	C_s^\dagger kg/m ³	i_{th}^\ddagger μA/cm ²	c_t^* mm
Low	structures placed at 2.84 km or more from the coast; sea spray carried by the wind is the main source of chlorides.	0.35	0.5	40
Moderate	structures located between 0.1 and 2.84 km from the coast without direct contact with seawater.	1.15	2	45
High	structures situated to 0.1 km or less from the coast, but without direct contact to seawater. RC structures subjected to de-icing salts can also be classified in this level.	2.95	5	50
Extreme	structures subjected to wetting and drying cycles; the processes of surface chloride accumulation are wetting with seawater, evaporation and salt crystallization.	7.35	10	55

Sources: [†]McGee (2000), [‡]Geocisa and the Torroja Institute (2002) and ^{*}European standard (2004).

based on the EN206 (Geocisa and the Torroja Institute, 2002), and the cover is defined according to EUROCODE 2 (European standard, 2004).

The basic considerations and assumptions in this example are:

- chloride diffusion occurs in saturated conditions;
- cross-section confinement is taken into account by using the Kent and Park model (Kent and Park, 1971) and stress-strain relationship for steel follows an elasto-plastic model;
- the elasticity modulus and the tensile strength of concrete are given in terms of the compressive strength according to EUROCODE 2 (European standard, 2004);
- a limit crack width of 0.5 mm is used as a threshold for severe concrete cracking, t_{sc} ;
- the water/cement ratio is calculated by using Bolomey's formula (Vu and Stewart, 2000);
- a threshold pit depth, p_0 , of 1.98×10^{-6} m is used to estimate the time to pit nucleation;
- the deterioration process is continuous; i.e. there is no maintenance; and
- the limit state of bending capacity is used to compute the ultimate crack size in steel a_c .

The probabilistic models adopted for the random variables are given in Table 5.7. It is worth noting the high variability of surface chloride concentration. Data reported by McGee (2000) on C_s was obtained from a field-based study of 1,158 bridges in the Australian state of Tasmania.

The chloride diffusion coefficient is influenced by many factors such as mix proportions (i.e. water/cement ratio, cement type), curing, compaction and environment (i.e. relative humidity and temperature), among others. Nonetheless, experimental studies report an important correlation between D_c and w/c (Papadakis et al., 1996; Thoft-Christensen, 2002). Papadakis et al. (1996) propose the following equation:

$$D_c(w/c) = 0.15D_{H_2O} \frac{1 + \rho_c w/c}{1 + \rho_c w/c + \frac{\rho_c a/c}{\rho_a}} \left(\frac{\rho_c w/c - 0.85}{1 + \rho_c w/c} \right)^3 \quad (5.1)$$

Table 5.7: Probabilistic models of the variables used in the example.

Variable	Distribution	Mean	COV
P	Log-normal	115 kN	0.20
f'_c	Normal	40 MPa	0.15
f_y	Normal	600 MPa	0.10
C_{th}	Uniform	0.90 kg/m ³	0.19
C_s			
Low	Log-normal	0.35 kg/m ³	0.50
Moderate	Log-normal	1.15 kg/m ³	0.50
High	Log-normal	2.95 kg/m ³	0.50
Extreme	Log-normal	7.35 kg/m ³	0.70
ρ_{rust}	Normal	3600 kg/m ³	0.10
τ_{por}	Log-normal	12.5 × 10 ⁻⁶ m	0.20
α	Gumbel	5.65	0.22

where, D_{H_2O} is the chloride diffusion coefficient in an infinite solution, (-i.e. $D_{H_2O}=50491.08$ mm²/yr for NaCl), a/c is the aggregate-to-cement ratio, and ρ_c and ρ_a are the densities of cement and aggregates, respectively. In order to compute the probabilistic model of D_c (equation 5.1), Monte Carlo simulations were carried out and a Kolmogorov-Smirnov test (KS-test) with a level of significance of 5% was adopted as the fitting criteria. This analysis also considers: (1) the values of a/c , ρ_c and ρ_a presented in Table 5.5, (2) the correlation between w/c and the compressive strength of concrete (i.e. Bolomey's formula) and (3) the probabilistic model of f'_c given in Table 5.7. The results of the KS-test indicate that D_c follows a log-normal distribution with mean equal to 41.96 mm²/yr (13.3×10^{-12} m²/s) and a COV of 67%. Vu and Stewart (2000) also reported other experimental data with similar values. In another approach, Thoft-Christensen (2002) considered that D_c depends principally on the water/cement ratio and the temperature, T :

$$D_c(w/c, T) = 11.146 - 31.025w/c - 1.941T + 38.212w/c^2 + 4.48w/cT + 0.024T^2 \quad (5.2)$$

In this case, by assuming that T is normally distributed $N(15^\circ\text{C}, 3^\circ\text{C})$, the KS-test indicates that D_c follows a log-normal distribution with mean equal to 16.25 mm²/yr (5.15×10^{-13} m²/s) and a COV of 35%. The results obtained by considering this approach are significantly smaller than in the first case. As a matter of fact, equation 5.2 results from fitting experimental data, and does not reflect the real scatter of the diffusion process in real structures. Therefore, by considering that the data obtained with the Papadakis formula are consistent with other empirical results, equation 5.1 is adopted.

Fatigue analysis is performed under cyclic loading simulated by a random wheel load, P , with a daily traffic frequency, f , applied at the center of the span. It is assumed that P follows a log-normal distribution (Table 5.7). To simplify the analysis, the traffic frequency and the statistical parameters of P are considered as time-invariant and the effect of higher traffic frequencies on the applied load is not taken into account. To study the implications of f , several scenarios were considered: 50, 500, 1000 and 2000 cycles/day. It is important to stress that these frequencies are in the range defined by the EUROCODE 1 for heavy trucks (European standard, 2004).

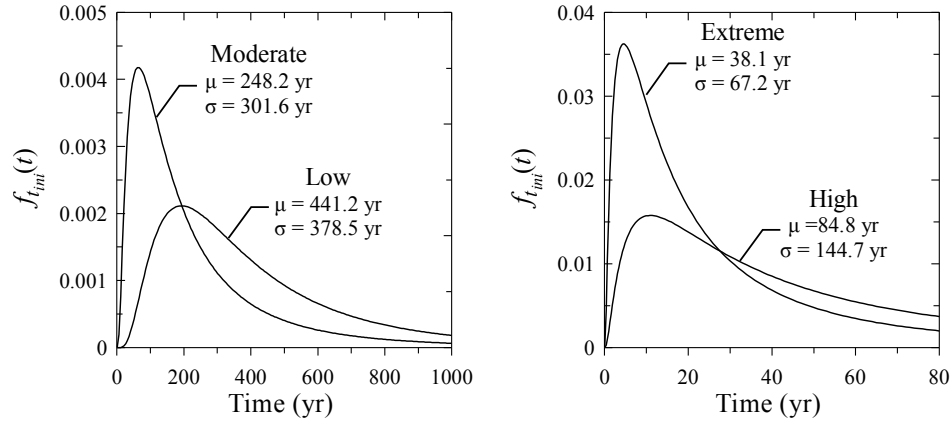


Figure 5.12: PDFs of t_{ini} for various levels of aggressiveness.

5.5.2 Results

The main goal of this analysis is to understand the influence of the most important variables on the length of each stage of the deterioration process:

1. corrosion initiation and pit nucleation,
2. pit-to-crack transition,
3. crack growth,
4. total corrosion-fatigue lifetime, and
5. contribution of each stage to the total lifetime.

5.5.2.1 Corrosion initiation and pit nucleation

For all levels of aggressiveness, the goodness-of-fit test indicates that both t_{ini} and t_{pn} follow log-normal distributions. As expected, the mean, $\mu_{t_{ini}}$, and standard deviation, $\sigma_{t_{ini}}$, decrease when environmental aggressiveness increases (Figure 5.12). The high standard deviations result from the high COVs of C_s and D_c . The impact of the high variability of C_s on the PDF of t_{ini} , is studied by varying its COV, as shown in Figure 5.13. Then, $\mu_{t_{ini}}$ diminishes when μ_{C_s} increases, and tends to larger values when the COV of C_s becomes high. It is also observed that the relationship between μ_{C_s} and $\mu_{t_{ini}}$ is not linear and there is a limit (e.g. $\mu_{C_s} = 2 \text{ kg/m}^3$) from which an increase of μ_{C_s} does not produce significant variation of $\mu_{t_{ini}}$. In addition, it should be noted that $\text{COV}(C_s)$ has more impact on $\mu_{t_{ini}}$ for smaller values of μ_{C_s} (Figure 5.13).

For the time to pit nucleation, the mean of t_{pn} varies between 3.9 and 5.4 days with a $\text{COV}(t_{pn})$ of 0.25 for all levels of aggressiveness. Therefore, given both the higher magnitude and the variability of the time to corrosion initiation, it can be concluded that the time to pit nucleation is negligible.

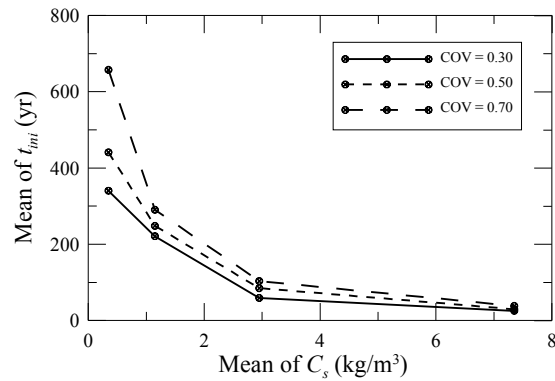


Figure 5.13: Relationship between $\mu_{t_{ini}}$ and μ_{C_s} in terms of $COV(C_s)$.

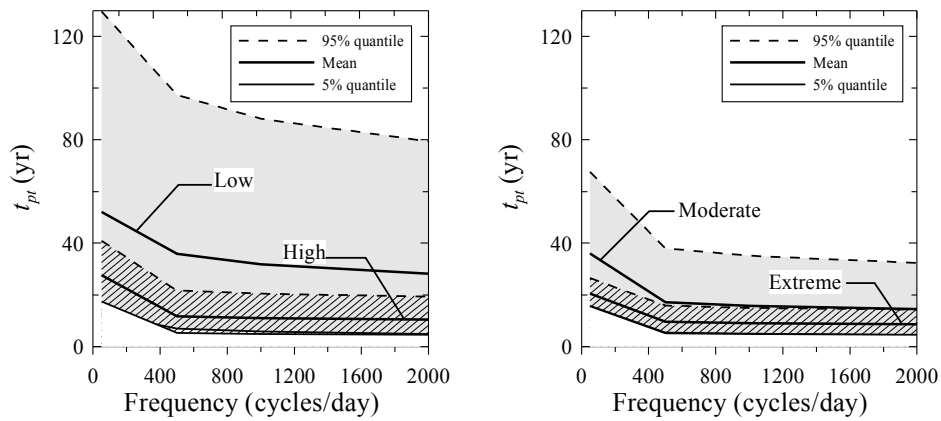


Figure 5.14: Mean and 90% confidence interval of t_{pt} for several traffic frequencies.

5.5.2.2 Pit-to-crack transition

For all levels of aggressiveness and traffic frequencies, the KS-test has shown that the time to transition from pit to crack follows a log-normal distribution. Figure 5.14 presents the mean and 90% confidence interval of t_{pt} , for several traffic frequencies. The ranges of [8.6, 52.1] years and [3.1, 41.8] years are obtained for $\mu_{t_{pt}}$ and $\sigma_{t_{pt}}$, respectively. In all cases, the mean and confidence interval for t_{pt} decrease for high values of traffic frequency. This phenomenon is expected because the crack growth rate is function of f , and therefore, the intersection between dp/dt and da/dt occurs earlier when f is increased. It can also be observed that the mean and the dispersion of t_{pt} are smaller when environmental aggressiveness increases. This reduction is explained by the fact that high levels of environmental aggressiveness are related to high values of i_{th} . Thus, when i_{th} reaches high values, the fatigue crack growth rate increases leading to early crack nucleation.

Since a crack is nucleated at the end of this stage, and the initial crack size becomes input data to compute the length of the following stage, Figure 5.15 shows the PDFs of a_0 , for various levels of aggressiveness with several traffic frequencies. In all cases, the goodness-of-fit test shows that a_0 follows a log-normal distribution with μ_{a_0} varying between 1.5 and 8.9 mm and σ_{a_0} between 0.95 and

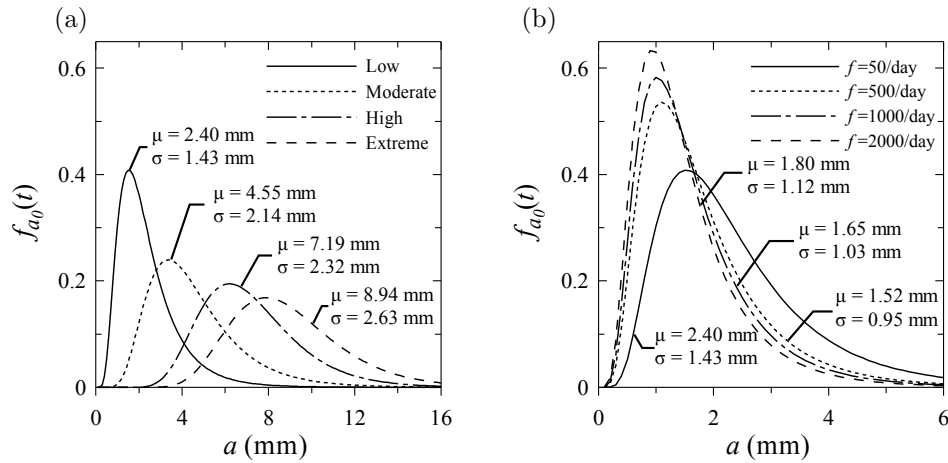


Figure 5.15: PDFs of a_0 for: (a) various levels of aggressiveness and $f = 50$ cycles/day; (b) low level of aggressiveness and various traffic frequencies.

2.63 mm. The overall behavior indicates that both the mean and standard deviation tend to higher values when the level of aggressiveness is increased (Figure 5.15a). This increase is expected, because given the predominance of pitting corrosion for high levels of aggressiveness, the transition occurs for larger initial crack sizes. From the relationship between the mean and standard deviation of a_0 and the traffic frequency, it is possible to notice that both μ_{a_0} and σ_{a_0} decrease when f goes to higher values (Figure 5.15b). This reduction is due to the fact that an increment of traffic frequency turns on the fatigue to become the predominant process, and subsequently, accelerates the pit-to-crack transition.

5.5.2.3 Crack growth

In all the cases, the KS-test confirms that t_{cg} follows a log-normal distribution with $\mu_{t_{cg}}$ varying between 1.6 and 47.9 years and $\sigma_{t_{cg}}$ between 0.3 and 11.1 years. Figure 5.16 shows the relationship between the mean and the 90% confidence interval of t_{cg} and traffic frequencies. Overall behavior indicates that the mean and the dispersion of t_{cg} diminishes when traffic frequency increases. This behavior is explained by the fact that failure is reached in a shorter period when frequency tends to higher values. Furthermore, it can be noted that the mean and the dispersion decrease for higher levels of aggressiveness. This reduction is due to the fact that the size of the initial crack leads to larger values for higher levels of environmental aggressiveness, and therefore, the time to reach failure is lower.

Section 4.2.2 explains the assessment of the size of the critical crack or pit at which the RC member reaches the bending limit state a_c . For all traffic frequencies and levels of environmental aggressiveness, a_c follows a Weibull distribution with mean and standard deviation of 11.86 and 0.97 mm, respectively. This non-dependency of f and environmental aggressiveness is expected because the bending limit state depends mainly on the critical cross-section of steel bars leading to bending failure, $A_s(a_c)$, as well as load intensity. In addition, it is observed that the mean of a_c is close to the deterministic value reported by Salah el Din and Lovegrove (1982) –i.e. $a_c = 0.5d_0 = 12.5$ mm.

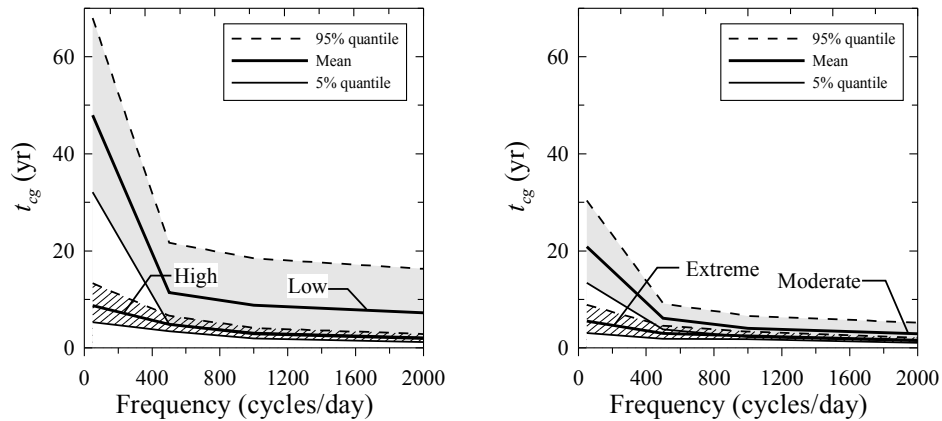


Figure 5.16: Mean and 90% confidence interval of t_{cg} for several traffic frequencies.

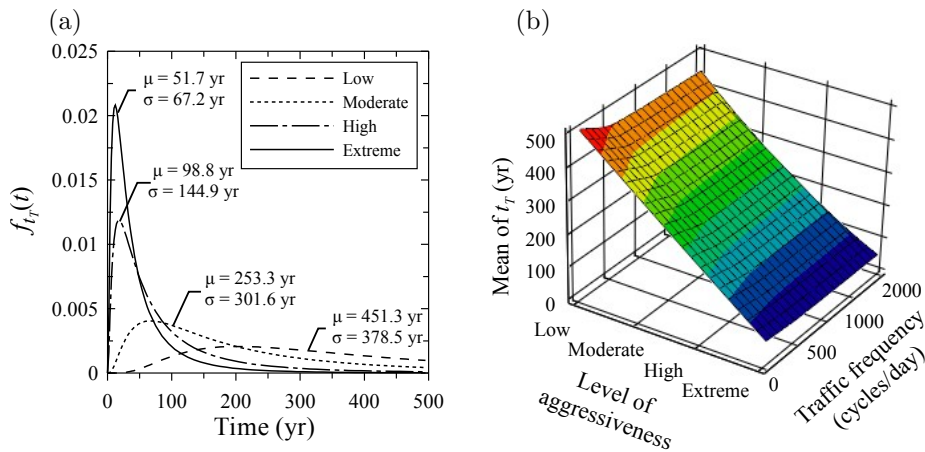


Figure 5.17: (a) PDFs of t_T for various levels of aggressiveness and $f = 500$ cycles/day; (b) mean of t_T for both, various levels of aggressiveness and traffic frequencies.

5.5.2.4 Total corrosion-fatigue lifetime

The total corrosion-fatigue lifetime t_T follows a log-normal distribution with mean varying between 35.8 and 448.8 years and standard deviation between 49 and 264.7 years. The PDFs of t_T for various levels of aggressiveness and $f = 500$ cycles/day are depicted in Figure 5.17a. As expected, μ_{t_T} and σ_{t_T} decrease for higher levels of aggressiveness. Figure 5.17b presents the mean of t_T for various levels of aggressiveness and traffic frequencies. In general, the critical time, t_T , occurs earlier when traffic frequency is augmented. Overall behavior of t_T agrees with the results found for each stage.

5.5.2.5 Contribution of each stage to total lifetime

The percentage of participation of each stage in the total corrosion-fatigue life is estimated by the ratios of the time-spans (Figure 5.18). In all cases, the participation is mainly due to t_{cp} , followed by t_{pt} and t_{cg} . Whereas for t_{cp} , the participation decreases when the level of aggressiveness is increased, for t_{pt} and t_{cg} , it grows when the level of environmental aggressiveness becomes higher. This behavior

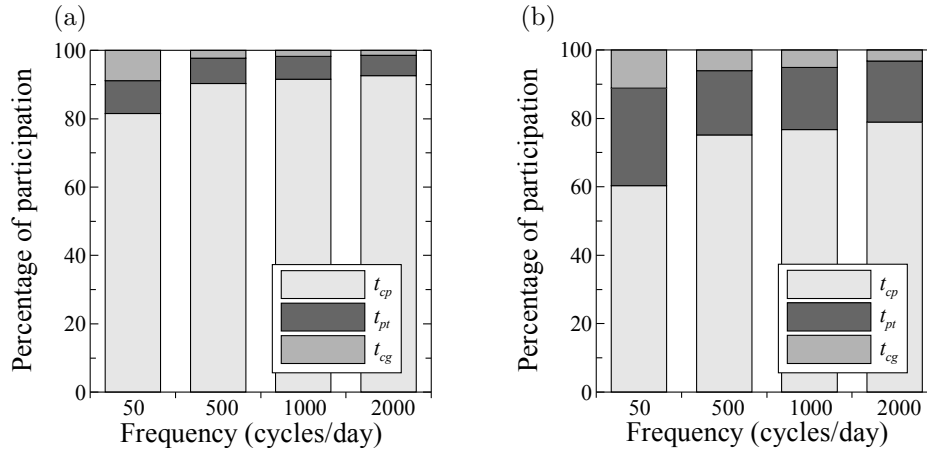


Figure 5.18: Participation of each phase in the total corrosion-fatigue life. (a) Low aggressiveness. (b) Extreme aggressiveness.

seems logical because an increment in the level of environmental aggressiveness accelerates the time to corrosion initiation and, subsequently, the participation of t_{pt} and t_{cg} takes larger values. By considering the relationship between t_{cp} and f , the percentage of participation of t_{cp} increases when traffic frequency grows. On the other hand, for t_{pt} and t_{cg} , their percentages decrease when f tends to higher values. This behavior is explained by the fact that larger traffic frequencies reduce the length of the crack nucleation and propagation stages. To conclude, given the larger impact of the time to corrosion initiation and pit nucleation on the total corrosion-fatigue life (i.e. 60 to 93% of t_T), maintenance efforts must be directed toward controlling this stage of the process.

5.5.3 Effects of corrosion-fatigue on total lifetime

This subsection presents the results concerning the combined effect of corrosion-fatigue on lifetime. First, expected total lifetimes are compared for the cases: (1) deterioration induced by corrosion only (i.e. without fatigue) and (2) deterioration produced by the combined action of corrosion-fatigue. This comparison is made to estimate the additional lifetime reduction induced by considering the combined effect. This section also shows the results of the time-dependent reliability analysis including the case without fatigue, and the analysis of the influence of A_s on failure probability.

5.5.3.1 Additional lifetime reduction induced by corrosion-fatigue

The relationship between the mean of t_T and the level of aggressiveness is plotted in Figure 5.19a. It should be noted that the mean of t_T for the case without considering fatigue damage (i.e. $f = 0$ cycles/day) is also included. The increase of traffic frequency induces an appreciable reduction of μ_{t_T} , in particular, in environments with low aggressiveness. By taking as a reference the case without considering fatigue damage, it is possible to estimate additional lifetime reduction induced by the combined action of corrosion and fatigue (Figure 5.19b). The additional reduction of t_T is high for smaller levels of aggressiveness and greater traffic frequencies. It can also be noticed that considering

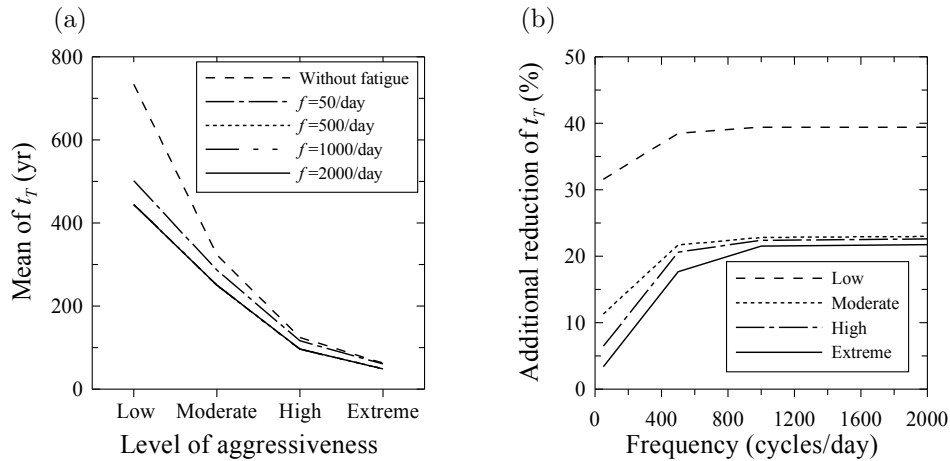


Figure 5.19: (a) Mean of t_T for various traffic frequencies. (b) Additional lifetime reduction induced by corrosion-fatigue.

the combined effect of corrosion and fatigue can represent an additional lifetime reduction from 3 to 39% with respect to the case without fatigue. The combined effect of corrosion and fatigue does not produce an appreciable additional lifetime reduction for both smaller traffic frequencies and very aggressive environments. However, for traffic frequencies between 500 and 2000 cycles/day, this combined effect induces additional lifetime reductions between 18 and 39%. These results strengthen the importance of including the combined effect of corrosion and fatigue in the lifetime assessment, in particular, when the structure is placed in corrosive environments under cyclic loading.

5.5.3.2 Structural reliability of the girder

The failure probability of the girder, p_f is plotted in Figure 5.20. The overall behavior indicates that p_f tends to higher values when both, the level of aggressiveness and the traffic frequency are increased. It must be noted that Figure 5.20 also includes the reliability analysis of the case without fatigue. As expected, reliabilities obtained by considering the combined action of corrosion and fatigue are higher than for the case without fatigue. It can also be observed that although the difference between the two cases is much larger for high traffic frequencies, for values between 500 and 2000 cycles/day, this difference remains almost constant. For instance, for a time-span of 100 years, a moderate level of aggressiveness, without considering fatigue damage, a failure probability of 1.1×10^{-2} is obtained; for the same conditions but with different frequencies, failure probability becomes 9.3×10^{-2} , 2.2×10^{-1} , 2.4×10^{-1} and 2.5×10^{-1} for traffic frequencies of 50, 500, 1000 and 2000 cycles/day, respectively. That means, the failure probability is increased by 8, 20, 21.8 and 22.7 times for the traffic frequencies of 50, 500, 1000 and 2000 cycles/day, respectively. It can be concluded that, although the combined effect of corrosion and fatigue causes a significant increase of p_f , there is a threshold above which the increase of f does not produce an appreciable change in p_f .

The influence of the reinforcement area, A_s , on the failure probability for a traffic frequency of 1000 cycles/day is plotted in Figure 5.21. Assuming that the design specifications must guarantee a given target failure probability –i.e. $p_{ft} = 10^{-4}$, during a lifetime of 50 yr, it can be observed from

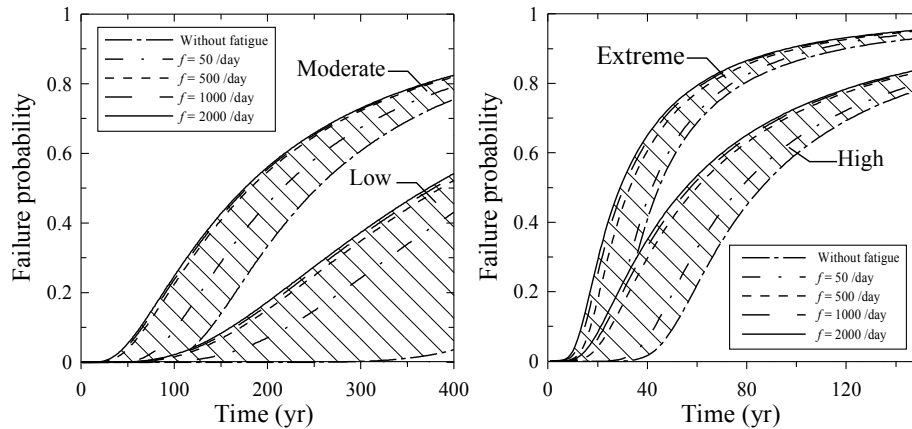


Figure 5.20: Time-dependent structural reliability of the considered bridge girder.

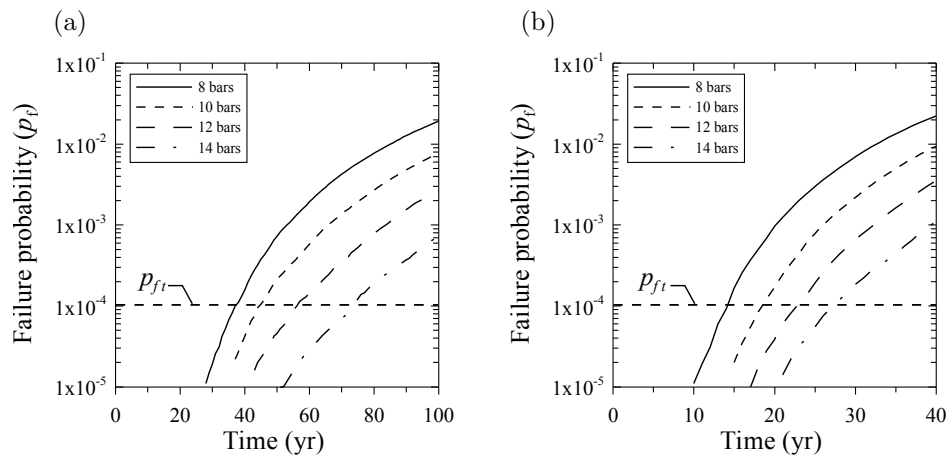


Figure 5.21: Influence of A_s on failure probability for several levels of aggressiveness: (a) low, (b) moderate.

Figure 5.21 that the reinforcement resulting from the design (i.e., 8 bars $d_0 = 25$ mm) does not assure p_{ft} . For the case of low aggressiveness (Figure 5.21a), increasing the number of bars of the same diameter (i.e., 14 bars $d_0 = 25$ mm) can guarantee this condition. Nevertheless, for the moderate level of aggressiveness, the failure probability is higher than p_{ft} at 50 years when the reinforcement area increases. Therefore, to ensure p_{ft} during the lifetime of the structure, it is necessary to implement other countermeasures such as inspection and maintenance programs for corrosion control.

5.6 Case study 5: Corrosion-fatigue under realistic environmental conditions

5.6.1 Problem description

A simplified solution of Fick's law is useful to sensitivity analyses such as the one presented in section 5.5. However, given that the analytical solution does not always represent reality, the goal of this section is to study the influence of realistic exposure conditions on failure probability. To accomplish

Table 5.8: Probabilistic models of the random variables.

Physical problem	Variable	Mean	COV	Distribution
<i>Chloride ingress</i>	$D_{c,ref}$	$3 \times 10^{-11} \text{ m}^2/\text{s}$	0.20	log-normal
	C_{th}	0.5 wt% cement	0.20	normal
	c_t	50 mm	0.25	normal ^a
	U_c	41.8 kJ/mol	0.10	beta on [32,44.6]
	m_c	0.15	0.30	beta on [0,1]
<i>Moisture diffusion</i>	$D_{h,ref}$	$3 \times 10^{-10} \text{ m}^2/\text{s}$	0.20	log-normal
	α_0	0.05	0.20	beta on [0.025,0.1]
	n	11	0.10	beta on [6,16]
<i>Heat transfer</i>	λ	2.5 W/(m °C)	0.20	beta on [1.4,3.6]
	ρ_c	2400 kg/m ³	0.20	normal
	c_q	1000 J/(kg °C)	0.10	beta on [840,1170]
<i>Corrosion-fatigue</i>	P	115 kN	0.20	Log-normal
	f'_c	40 MPa	0.15	Normal
	f_y	600 MPa	0.10	Normal
	ρ_{rust}	3600 kg/m ³	0.10	Normal
	τ_{por}	$12.5 \times 10^{-6} \text{ m}$	0.20	Log-normal
	α	5.65	0.22	Gumbel

^atruncated at 10 mm (lower bound)

this objective, the lifetime prediction includes the numerical solution for the transport governing equations in the assessment of the corrosion initiation time (section 3.2).

This example evaluates the influence of realistic environmental conditions on a simply supported RC girder presented in Figure 5.11. The material properties are presented in Table 5.5 and the climatic conditions are defined by:

- two environments: oceanic and tropical (Table 5.3);
- two scenarios of global warming: without and pessimistic (Table 5.4); and
- three levels of aggressiveness: low, moderate and high (Table 5.6).

The time to corrosion initiation considers flow of chlorides in one dimension where the Langmuir isotherm is used to account for chloride binding. The constants of the isotherm are $\alpha_L = 0.1185$ and $\beta_L = 0.09$. Similar to the example presented in section 5.5, fatigue loading is modeled by a random wheel load at the center of the span with a frequency ranging between 50 and 2000 cycles per day. The probabilistic models used to estimate the time to corrosion initiation and those corresponding to corrosion-fatigue propagation are presented in Table 5.8. Contrary to the simplified solution of Fick's law, note that the major part of random variables are used to describe the uncertainty inherent in chloride propagation. Since it was observed that the length of time to corrosion initiation is significant in total lifetime (Figure 5.18), it can be stated that this model is more representative because it studies the chloride penetration process in detail as well as its related randomness.

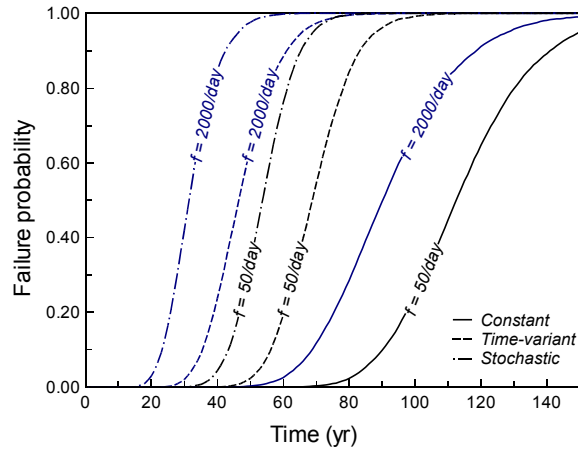


Figure 5.22: Influence of the type of entry on the failure probability for the oceanic environment.

5.6.2 Results

5.6.2.1 Influence of the environment

The effect of the weather model (constant, time-variant and stochastic) on failure probability is presented in Figure 5.22. These curves, obtained for the oceanic environment, do not consider the effect of global warming and correspond to a high level of environmental aggressiveness –i.e., $\mu_{C_{env}} = 2.95$ kg/m³ and $i_{th} = 5\mu\text{A}/\text{cm}^2$. Three types of environmental inputs are included in the analysis. The stochastic type includes seasonal variations and randomness for weather inputs (temperature, humidity and environmental chloride concentration). For the time-variant type, a sinusoidal function is used to consider the seasonal variations of temperature and humidity. The environmental chloride concentration is defined as constant for this case. Finally, the constant case supposes that temperature, humidity and environmental chloride concentration are time-independent –i.e., $T = 15^\circ\text{C}$, $h = 0.7$ and $C_{env} = 2.95$ kg/m³.

In general, failure probability is dependent on the type of input entries and frequency. Constant and time-variant models underestimate failure probabilities. For instance, for a traffic frequency of 50 cycles per day, a constant level of failure probability (i.e., $p_f = 0.5$) is reached at 53, 69 and 113 years for stochastic, time-variant and constant entries respectively. Taking as a reference the stochastic case, this implies that the time-variant and constant cases overestimate the time to reach $p_f = 0.5$ respectively of 16 and 60 years. A similar behavior is observed when traffic frequency is increased. Since the total fatigue lifetime is highly dependent on time to corrosion initiation, it is expected that the type of input entries becomes a paramount parameter in the assessment of failure probability (e.g., Figure 5.3). As discussed previously, these results support the use of a comprehensive model of chloride ingress including realistic environmental inputs for an optimum lifetime assessment.

5.6.2.2 Failure probability

Figure 5.23 presents the failure probability of the beam for the tropical environment and the three levels of aggressiveness considered. The analysis included stochastic environmental entries and does

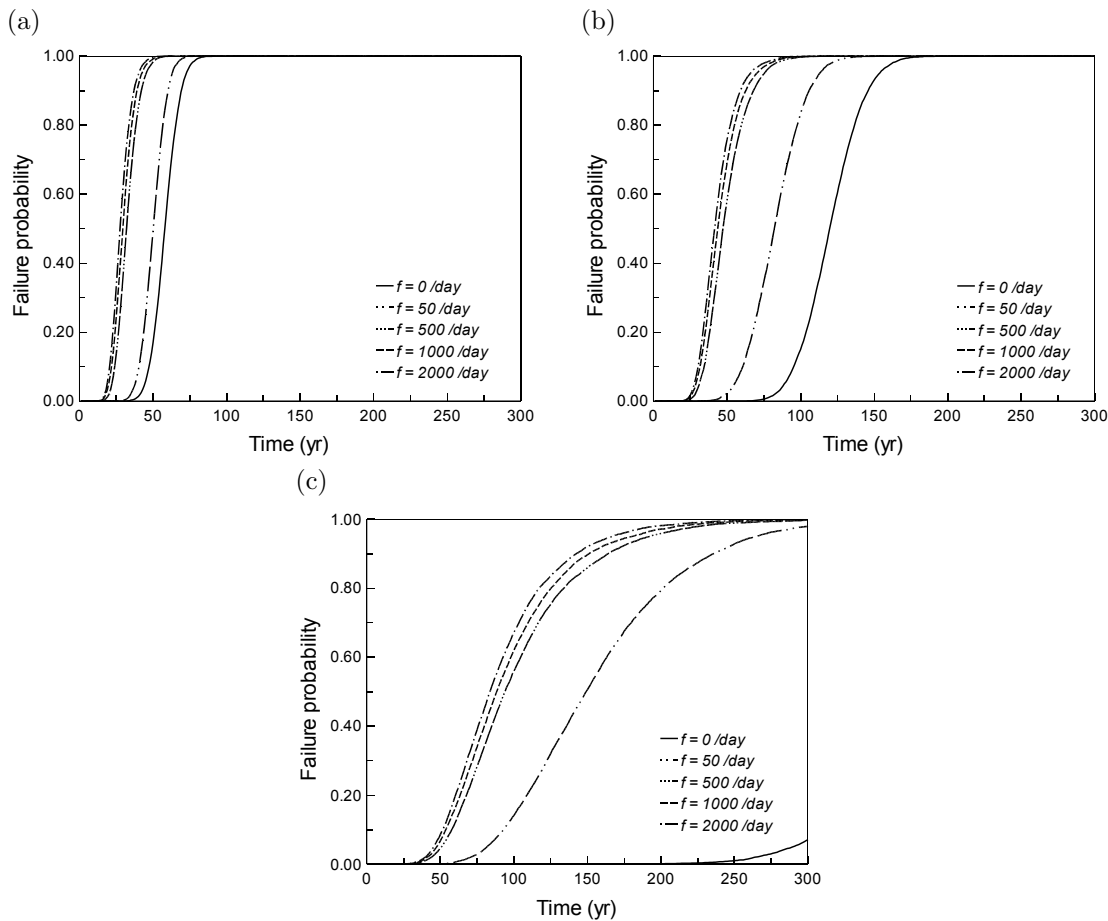


Figure 5.23: Failure probability for the tropical environment (a) high; (b) moderate and (c) low.

not account for the action of global warming.

It is observed that the failure probability increases, in all cases, when the level of aggressiveness and the frequency tend to higher values. This increment is caused by (1) higher concentrations of chlorides and corrosion rates of aggressive environments and (2) quicker crack propagation under greater traffic frequencies. If the failure probabilities are evaluated for a life-cycle length of 50 years, it is noted that the structural reliabilities are very low for all levels of aggressiveness. By considering that the failure probability should be lower than a critical value to ensure a safety level –i.e., $p_f < p_{ft} = 10^{-4}$, the studied structural configuration only guarantees this condition for the moderate level when there is no cyclic load ($p_f = 10^{-4}$) and for the low level when there is no fatigue loading ($p_f = 7 \times 10^{-5}$) and traffic frequency is 50 cycles per day ($p_f = 4 \times 10^{-4}$). These results are not surprising because in real structures close to the sea, as ports or quays, appreciable levels of deterioration have been reported after 15–20 years of exposure. The behavior for the oceanic environment is similar, but the failure probabilities are lower for all exposures and frequencies. This behavior indicates that a sophisticated model of chloride ingress calibrated with experimental observations and monitored with inspections should be included in the management of structures to assure appropriate levels of safety during the life-cycle.

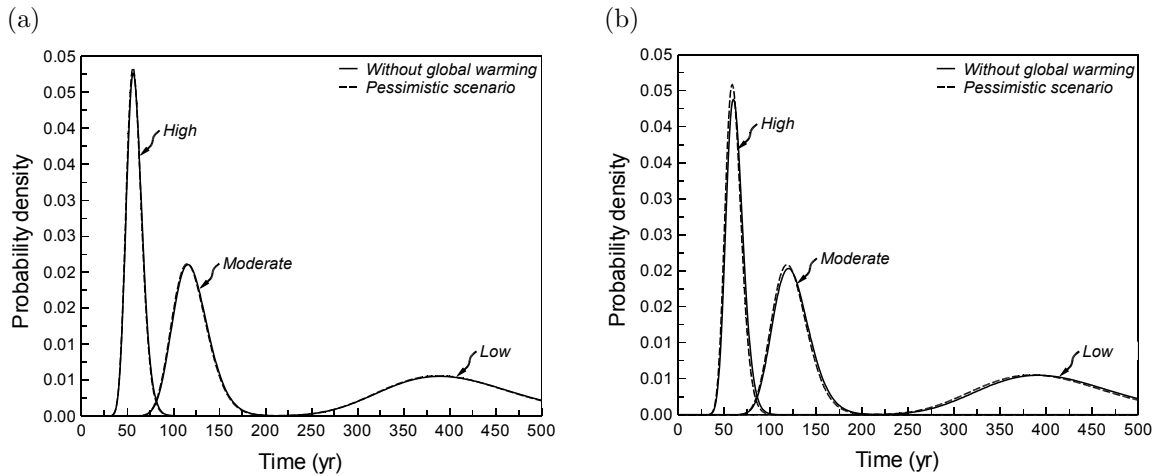


Figure 5.24: PDF total lifetime without fatigue effects (a) tropical environment; (b) oceanic environment.

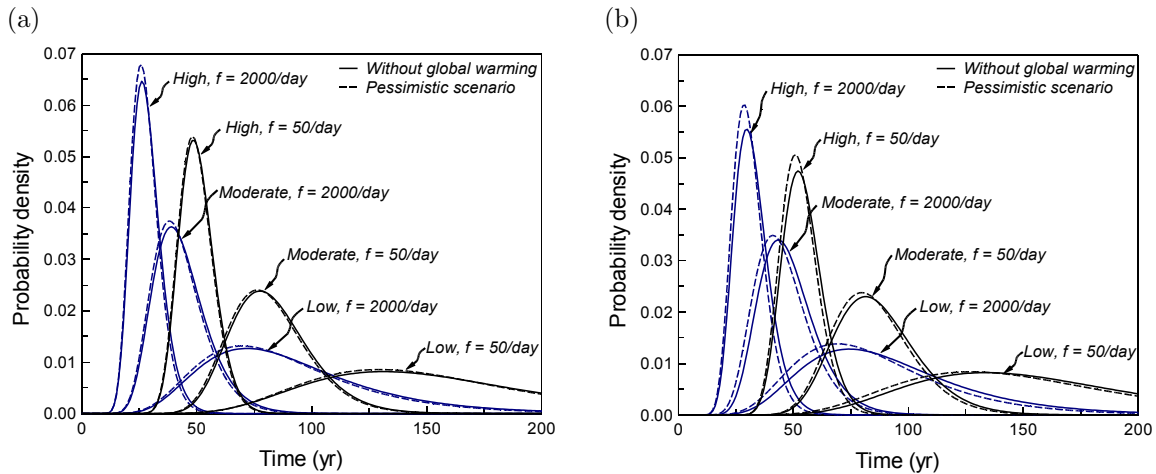


Figure 5.25: PDF total fatigue lifetime (a) tropical environment; (b) oceanic environment.

5.6.2.3 Effect of weather

The effects of weather and global warming on total lifetime is evaluated in terms of PDF. The PDFs for all the studied cases were adjusted from the Monte Carlo results where the selection criterion was the Kolmogorov-Smirnov test with a level of significance of 5%. As pointed out in section 5.5, it was found for all cases that the best fitting corresponds to log-normal distribution. Figures 5.24 and 5.25 present the PDFs of the total lifetime for two limit state functions. The former (Figure 5.24) supposes that there is no cyclic loading, and consequently, the failure mechanism is corrosion-induced cross section reduction. The latter (Figure 5.25) accounts for combined corrosion-fatigue deterioration damage.

When the structure is not subjected to cyclic loading or corrosion-fatigue damage is neglected, Figure 5.24 shows that the mean, μ_{t_T} , and the standard deviation, σ_{t_T} , of the total lifetime decrease for more aggressive environments. It is observed in general that μ_{t_T} is lower for tropical than for oceanic environments. This behavior seems logical because tropical environments are characterized by

higher temperatures and humidities that accelerate chloride ingress reducing corrosion initiation time. It is also noted that the effect of global warming is more important for structures located in oceanic environments. This analysis includes only the pessimistic scenario of global warming because there is no major difference between the expected and pessimistic scenarios. While for the tropical environment global warming only induced reductions from 0.4 to 0.7% in μ_{t_T} , for the oceanic environment this reduction ranges between 1.4 and 2.3%. As discussed in section 5.4, global warming has more influence in environments where humidity and temperature are characterized by important seasonal variations.

The effect of cyclic loading and global warming for tropical and oceanic environments when corrosion-fatigue damage is considered is plotted in Figure 5.25. This analysis also includes the effect of two traffic frequencies. Similar to the previous case, μ_{t_T} and σ_{t_T} decrease when both the level of aggressiveness and traffic frequency increase. By comparing both cases (with and without fatigue damage) it is observed that the mean of the PDF is reduced when the assessment considers the effect of the cyclic load. The reduction with respect to the case without fatigue is more important for higher traffic frequencies. For example, whereas for $f = 50$ cycles/day μ_{t_T} is reduced by 13%, 30% and 60%, respectively for high, moderate and low aggressiveness, for $f = 2000$ cycles/day these values correspond to 50%, 65% and 77%. Given the notable difference, these results justify the consideration of combined damage mechanisms in lifetime assessment.

Similar to the case without fatigue damage, the structures located in oceanic environments are more susceptible to the effects of global warming. The reduction of μ_{t_T} varies between 0.8 and 2.5% for the tropical environment and ranges between 2.6 and 3.9% for the oceanic environment when traffic frequency is $f = 50$ cycles/day. The impact of global warming increases for higher traffic frequency ($f = 2000$ cycles/day) where reductions from 2.1 to 3.2% were observed for the tropical environment and from 4.4 to 7% for the oceanic environment. High frequencies reduce the length of the stages of pit-to-crack transition and crack propagation (Figure 5.18), and consequently, the participation of the stage of time to corrosion initiation and pit nucleation becomes more important. Since the proposed model of global warming only influences the time to corrosion initiation, its impact under higher traffic frequencies is more considerable.

For all cases and environments, it is observed that the reduction induced by global warming is maximum 7% of total lifetime. However, it is important to clarify that these results are conservative because they do not include the effect of global warming after corrosion initiation. Nowadays, it is known that corrosion rate can be influenced by temperature and humidity, and therefore, should be affected by global warming. Nevertheless, there is no a model that considers this interaction. Further research in this area is required to improve the prediction after corrosion initiation.

5.7 Summary and conclusions

This chapter presented five numerical applications of the model proposed in this study. While the first part of the chapter was related to chloride ingress, the last part focused on the effect of corrosion-fatigue.

The main conclusions are:

1. The results of the numerical examples indicate that the kinematics of chloride penetration is highly influenced by the random nature of temperature, humidity, surface chloride concentra-

tion, chloride binding, convection and two-dimensional chloride ingress. Corrosion-fatigue is mainly governed by threshold corrosion rates, surface chloride concentration and traffic frequency. Therefore, the accuracy of the proposed model depends on the precise characterization of such parameters.

2. The probabilities of corrosion initiation and failure were evaluated by using Monte Carlo simulations and Latin Hypercube sampling. Overall behavior demonstrated that both probabilities are mainly influenced by the features of place such as: distance to the sea, temperature, humidity, etc.
3. Given that the proposed model integrates a probabilistic approach, the lifetime reduction produced by the coupled action of corrosion and fatigue was computed on the basis of failure probability. For traffic frequencies between 500 and 2000 cycles/day, the coupled effect of corrosion-fatigue leads to lifetime reductions between 18 and 39%. When no fatigue damage is considered, the effect of global warming only induces lifetime reductions ranging between 1.4 and 2.3%. Under cyclic loading, total lifetime could be reduced by 7% by global warming action. These results highlight the importance of including the coupled effect of corrosion and fatigue for comprehensive lifetime assessment.

CHAPTER 6

CLOSURE

6.1 Conclusions

In accordance with the main objectives of this thesis, the following conclusions have been drawn:

1. Corrosion-fatigue of RC structures is a complex deterioration process that can be represented by diffusion, electrochemical and mechanical principles. Given that the whole process includes the interaction between various phenomena (i.e., chloride penetration, corrosion of reinforcement, concrete cracking and corrosion-fatigue of reinforcement bars), the discussion of the state-of-the-art in lifetime modeling focused on each phenomenon separately:
 - *Chloride penetration* is a diffusion/convection process modeled by analytical or numerical solutions of Fick's law. Analytical solutions are useful for sensitivity analyses and use few parameters. However, its assumptions are not valid for real exposure conditions. Numerical solutions consider the effects of: (1) chloride penetration in unsaturated conditions; (2) chloride binding capacity; (3) time-dependence of temperature, humidity and surface chloride concentration; and (4) flow of chlorides in two dimensions. Nevertheless, they require several parameters and are time-consuming.
 - *Corrosion of reinforcement* is governed by electrochemical principles and can be measured in terms of corrosion rate which is affected by temperature, humidity, oxygen availability and concrete electrical resistivity. Furthermore, the kinematics of corrosion rate can change when the RC member is cracked. However, current models of corrosion rate do not consider the interaction between these factors.
 - *Concrete cracking* is produced by the accumulation of corrosion products in the steel/concrete interface. There are analytical and numerical approaches to estimate the time to concrete cracking initiation and the crack growth. Since there is good agreement between experimental measures and results obtained for the analytical models, they are implemented in this study to determine the length of this stage.
 - *Corrosion-fatigue of reinforcement* appears when RC structures are located in chloride-contaminated environments and subjected to cyclic loading. Corrosion pits generate stress concentrations that can nucleate cracks in the reinforcing bars. Subsequently, the cyclic

load propagates the cracks until rupture. Although structural failures caused by the combined effect of corrosion and fatigue have not been reported, experimental testing evidence the lifetime reduction produced by corrosion-fatigue. Thus, it is necessary to develop a model that takes into account the combined corrosion-fatigue action to improve lifetime assessments.

2. Based on the needs for deterioration modeling defined in chapter 2, the following contributions to each stage of the model were made:

Chloride penetration: implementation of analytical and numerical solutions of Fick's diffusion law. While the analytical solutions are based on error function, the numerical solution combines finite difference and finite element methods to solve the governing equations of the problem.

Reinforcement corrosion: development of two models for corrosion rate. The first one accounts for the increase of oxygen availability as a result of concrete cracking. The second one uses a fuzzy approach to consider the effect of environmental aggressiveness after severe concrete cracking initiates.

Concrete cracking: implementation of analytical models to estimate: (1) the time to crack initiation and (2) the time to severe cracking. These models consider the stresses generated by the accumulation of corrosion products at the steel/concrete interface and were calibrated based on experimental testing.

Corrosion-fatigue of reinforcing bars: development of a model that combines the effects of corrosion and fatigue on the reduction/cracking of the cross-section of reinforcing bars. The model takes into account the interaction between: (1) corrosion induced by chloride ingress, (2) concrete cracking resulting from the accumulation of corrosion products and (3) reinforcement fatigue produced by cyclic loading. Corrosion-fatigue of reinforcement is modeled by linear elastic fracture mechanics and Paris-Erdogan law.

The model presented in this thesis is based on and combines extensive experimental studies at the different stages of the process. Moreover, the modularity of the proposed scheme has the advantage of being able to take account new information and/or observations either by updating the behavior parameters, or by introducing more refined and accurate models and components. For instance, the numerical applications presented in chapter 5 considered two models of chloride penetration.

3. As in all phenomena in nature, the corrosion-fatigue deterioration process is a random phenomenon. The main sources of uncertainty are related to: (1) material properties, (2) the model and its parameters and (3) environmental actions. Two kinds of uncertainties were identified in the corrosion-fatigue process, namely, randomness and fuzziness. Randomness was treated by random variables and stochastic processes. Time-invariant random variables represented the uncertainties of the material properties and the model and its parameters. The probabilistic models of time-invariant random variables were defined based on a literature survey. Stochastic processes described the environmental actions; thus, this study proposed stochastic models for:

- temperature and humidity (including the effect of global warming) and
- environmental chloride concentration (distinguishing between exposure to de-icing salts or sea).

On the other hand, fuzziness was used to model corrosion rate and was modeled by fuzzy sets. Based on measurements of corrosion rate reported in the literature, this fuzzy approach takes into account the influence of environmental aggressiveness after severe concrete cracking occurs. The advantage of this model lies in the consideration of experts' knowledge and empirical models or observations. For instance, the proposed model is based on an analytical model of corrosion rate for un-cracked concrete (Vu and Stewart, 2000) and the fuzzy observations of maximum corrosion rate defined by EN206 (Geocisa and the Torroja Institute, 2002).

4. The proposed model of corrosion-fatigue was illustrated by various numerical applications. The conclusions of these examples are summarized as follows:

Factors controlling chloride ingress: the results indicate that the mean of corrosion initiation time decreases when the randomness and the seasonal variations of humidity, temperature and chloride concentration, as well as convection are considered; and increases when chloride binding is taken into account. By comparing chloride penetration in one- and two-dimensions, it has been found that high probabilities of failure correspond to 2-D exposure. These results stress the importance of including the effects and the random nature of temperature, humidity, surface chloride concentration, chloride binding, convection and two-dimensional chloride ingress for a comprehensive lifetime assessment.

Impact of weather: the examples considered three environments –i.e., continental, oceanic and tropical. It was observed that the highest probabilities of corrosion initiation correspond to marine environments, in particular, for tropical environments. These results are explained by the facts that (1) structures placed in marine environments are exposed to chlorides all the time and (2) higher temperatures and humidities accelerate the penetration of chloride ions into the concrete matrix. The probability of corrosion initiation increases in structures close to the sea. This effect is more appreciable for the tropical environment because greater values of temperature and humidity reduce the time to corrosion initiation.

Effect of global warming: the results indicate that the lifetime reduction induced by global warming is more significant for structures located in chloride-contaminated environments far from the sea. The climate change effect is high for structures located in oceanic environments and leads to lifetime reductions ranging from 2 to 18%. These observations justify the implementation of countermeasures directed to (1) reduce and/or mitigate the action of global warming on weather and (2) minimize the impact of climate change on RC structures.

Sensitivity analysis of corrosion-fatigue damage: the failure probability of RC structures subjected to corrosion-fatigue depends highly on threshold corrosion rates, surface chloride concentration and traffic frequency. The expected time to pit nucleation has a smaller value in comparison with the expected time to corrosion initiation; therefore, the length of this stage can be neglected. It was also observed that pit-to-crack transition and crack

growth occur early when both the level of aggressiveness and traffic frequency increased. Regarding external loading, for traffic frequencies between 500 and 2000 cycles/day, the combined effect of corrosion-fatigue becomes paramount by leading to additional lifetime reductions between 18 and 39%. However, there is a limit after which the increase of traffic frequency does not produce appreciable changes in failure probability. If a target failure probability is set to 10^{-4} , for a structure with operating lifetime of 50 years, the structural configuration selected does not reach this value for all considered environmental conditions. Therefore, to guarantee a predefined target failure probability, it is necessary to implement countermeasures such as inspection and maintenance programs for corrosion control.

Interaction between corrosion-fatigue and weather: the type of model of weather actions (constant, time-variant and stochastic) influences failure probability. For instance, taking as a reference the stochastic model of weather, the time-variant and constant models overestimate the time to reach $p_f = 0.5$ respectively of 16 and 60 years. These results support the use of a comprehensive model of chloride ingress including realistic environmental inputs for an optimum lifetime assessment. It was observed that the failure probability increases when the level of aggressiveness and the frequency tend to higher values. Given that higher failure probabilities were computed after 50 years of exposure –i.e., $p_f > 10^{-4}$, it is claimed that a comprehensive management of RC structures exposed to chlorides should include sophisticated models of chloride ingress calibrated with experimental observations and monitored by inspections. The mean of total lifetime decreases for more aggressive environments and is lower for tropical than for oceanic environments. When no fatigue damage is considered, the effect of global warming only induces lifetime reductions ranging between 1.4 and 2.3%. Under cyclic loading, total lifetime could be reduced by 7% by global warming action. However, these results underestimate the real action of climate change because they do not include its effect after corrosion initiation. Further research in this area is required to improve the prediction after corrosion initiation.

6.2 Recommendations for future research

Based on the findings of this study, there are seven areas in which further research is needed to enhance the proposed model:

- determination of model parameters (for chloride penetration, concrete cracking and corrosion rate) for a wide range of concrete types;
- characterization of the parameters of crack propagation (according to the Paris-Erdogan law) for several types of reinforcing bars in corrosive environments;
- study and formulation of a model that considers the kinematics between concrete cracking and chloride penetration;
- consideration of the spatial variability of the phenomenon which generates multiple pits and cracks that affect structural performance;

- development of a corrosion rate model that takes into account the effects of concrete electrical resistivity and weather (including global warming);
- implementation of a stochastic model of cyclic loading that considers the increase of both the frequency and the magnitude of applied loads; and
- characterization and modeling of error propagation in the whole deterioration process.

APPENDIX A

RELIABILITY ANALYSIS

A.1 Time-invariant reliability analysis

Reliability methods have been conceived to take into account the uncertainty of the parameters of a given problem in terms of the failure probability of a structure. In this approach the governing parameters of the problem are modeled as random variables. Random variables can be grouped in a random vector \mathbf{X} which joint PDF of \mathbf{X} is equal to $f_{\mathbf{X}}(\mathbf{x})$. For reliability analysis, the domain of the problem \mathcal{D} is divided into the *failure domain* and the *safe domain* (Figure A.1). The failure domain \mathcal{D}_f is defined by:

$$\mathcal{D}_f = \{\mathbf{X} | g(\mathcal{M}(\mathbf{X})) \leq 0\} \quad (\text{A.1})$$

where $\mathcal{M}(\mathbf{X})$ represents the response of the system and $g(\mathcal{M}(\mathbf{X}))$ the *limit state function* of the problem. In the simplest case, $\mathcal{M}(\mathbf{X})$ is expressed as the subtraction between the resistance $\mathcal{R}(\mathbf{X})$ and the demand on the system $\mathcal{S}(\mathbf{X})$:

$$\mathcal{M}(\mathbf{X}) = \mathcal{R}(\mathbf{X}) - \mathcal{S}(\mathbf{X}) \quad (\text{A.2})$$

In reliability engineering analysis, $\mathcal{M}(\mathbf{X})$ is usually expressed in terms of displacement, strain, stress, etc. The *safety domain*, \mathcal{D}_s , is defined by:

$$\mathcal{D}_s = \{\mathbf{X} | g(\mathcal{M}(\mathbf{X})) > 0\} \quad (\text{A.3})$$

The boundary between these two domains constitutes the limit state surface –i.e., $\{g(\mathbf{X}, \mathcal{M}(\mathbf{X})) = 0\}$. By accounting for these definitions, the failure probability, p_f , is determined by:

$$p_f = \text{P}[g(\mathcal{M}(\mathbf{X})) \leq 0] = \int_{g(\mathcal{M}(\mathbf{x})) \leq 0} f_{\mathbf{X}}(\mathbf{x}) dx_1 \dots dx_n \quad (\text{A.4})$$

A.2 Time-dependent reliability analysis

In some cases, the input random variables or the response of the system can be time-dependent. Structures subjected to deterioration processes such as corrosion and fatigue are two examples of

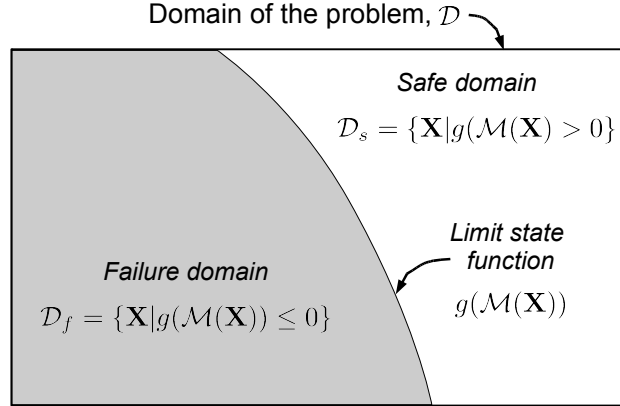


Figure A.1: Domain of the problem for reliability analysis.

time-dependent problems. In both cases, the resistance of the material is reduced and/or there are stochastic inputs during the life cycle of the structure. Examples of these actions are:

- *Environmental actions:* wind, temperature, humidity, chloride concentration, etc.
- *Operational actions:* cyclic loading induced by traffic, etc.

In these cases, the random variables become time-dependent $X(t, \omega)$ and are known as scalar random or stochastic processes. Then, at a given time t_0 , $X(t_0, \omega) \equiv X_{t_0}(\omega)$ represents a random variable. Where ω describes the *outcome*; all possible outcomes constitute the sample space Ω . Conversely, for a fixed outcome ω_0 , a sample function or trajectory is noted $x(t, \omega_0)$ or simply $x(t)$. A stochastic process is also characterized by a joint PDF of finite sets of variables $\{X_{t_1}, \dots, X_{t_n}\}$ for $t_1 < \dots < t_n \in \mathbb{R}^n$.

Time-dependent reliability analysis studies the evolution of failure probability over time. Towards this aim, the domain and sub-domains of the problem also depend on time, i.e., $\mathcal{D}(t)$. Thus, the *failure domain*, $\mathcal{D}_f(t)$ is written:

$$\mathcal{D}_f(t) = \{\mathbf{X} | g(\mathcal{M}(\mathbf{X}, t)) \leq 0\} \quad (\text{A.5})$$

where $\mathcal{M}(\mathbf{X}, t)$ and $g(\mathcal{M}(\mathbf{X}, t))$ represent the response of the system and the limit state function in time, respectively. Therefore, the time-dependent failure probability, $p_f(t)$, is computed as:

$$p_f(t) = P[g(\mathcal{M}(\mathbf{X}, t)) \leq 0] = \int_{g(\mathcal{M}(\mathbf{X}, t) \leq 0} f_{\mathbf{X}}(\mathbf{x}, t) dx_1 \dots dx_n \quad (\text{A.6})$$

where $f_{\mathbf{X}}(\mathbf{x}, t)$ represents the time-dependent joint PDF of the problem.

A.3 Methods for reliability assessment

Explicit solutions of equations A.4 or A.6 are difficult to find in most cases. Therefore, several methods have been proposed to evaluate failure probability. Sudret and Der Kiureghian (2000) classify these methods as function of the quantities of interest as:

1. when the mean value and the standard deviation are the quantities of interest, second moment analysis methods are used. This category includes: the *perturbation method*, the *weighted integral method* and the *quadrature method*.
2. when the region of interest is situated at the tails of the joint PDF, methods of structural reliability analysis should be implemented. The most commonly used methods in this category are: FORM/SORM, *importance sampling* and *directional simulation*.
3. when analysis is focused on the whole domain, *Monte Carlo simulation* is the basic approach to solve the problem.

Given the nature of the problem and the complexity of the system (chapters 3 and 4), this study has implemented Monte Carlo simulation and Latin Hypercube sampling.

A.3.1 Monte Carlo simulation

The Monte Carlo method is based on the *law of large numbers* and is a simple technique to estimate the expected value I of a given function, G :

$$I = \int_{\mathcal{D}} G(\mathbf{x}) f_{\mathbf{X}}(\mathbf{x}) dx_1 \dots dx_M \quad (\text{A.7})$$

where \mathbf{X} is a random vector of dimension M –i.e. $\mathbf{X} = (X_1, \dots, X_M)$; $f_{\mathbf{X}}(\mathbf{x})$ is the joint PDF of \mathbf{X} ; and \mathcal{D} the domain of integration. Equation A.7 can also be expressed in terms of the expected value $E[\cdot]$:

$$I = E[\mathbf{1}_{\mathcal{D}}(\mathbf{X})G(\mathbf{X})] \quad (\text{A.8})$$

where $\mathbf{1}_{\mathcal{D}}(\mathbf{X})$ is the characteristic function of \mathcal{D} which is equal to 1 if $\mathbf{X} \in \mathcal{D}$ and 0 otherwise. The law of large numbers establishes that the mean of independent realizations converges very likely to the mathematical expectation. Based on this definition, an unbiased estimator of I , Θ , gives an approximation to the expected value of $G(\mathbf{X})$ (i.e., $\Theta \approx E[G(\mathbf{X})]$):

$$\Theta = \frac{1}{N} \sum_{i=1}^N \mathbf{1}_{\mathcal{D}}(\mathbf{X}^{(i)})G(\mathbf{X}^{(i)}) \quad (\text{A.9})$$

where N is the number of realizations. Its variance σ^2 is defined as:

$$\sigma^2 = \frac{1}{N-1} \left[\frac{1}{N} \sum_{i=1}^N \mathbf{1}_{\mathcal{D}}(\mathbf{X}^{(i)})G(\mathbf{X}^{(i)})^2 - \Theta^2 \right] \quad (\text{A.10})$$

It can be observed from equation A.10 that the variance tends to zero for a large number of realizations –i.e., $N \rightarrow \infty$. This means that the estimator Θ is more accurate when the number of simulations increases.

Figure A.2a shows an example where the quantity of interest is the probability of failure. In this case, the characteristic function $\mathbf{1}_{\mathcal{D}_f}(\mathbf{X})$ indicates if a simulation belongs to the failure domain and

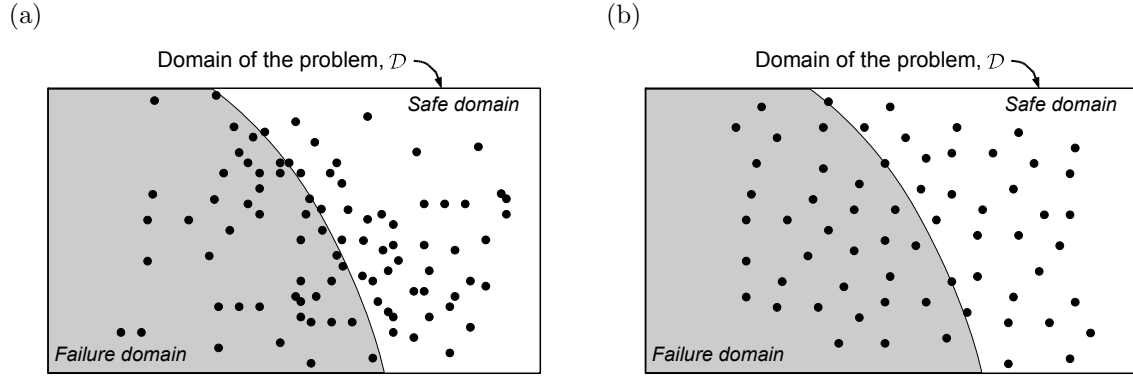


Figure A.2: Illustration of (a) Monte Carlo simulation and (b) Latin hypercube sampling.

p_f is estimated from equation A.9. It can also be noted that the distribution of the points is widely spread. While there are some empty areas, several points are concentrated in other areas. Hence, it is necessary to perform a large number of simulations to ensure that the estimator is representative of the problem.

A.3.2 Latin Hypercube sampling

Latin Hypercube sampling is a method used to reduce the variance of the estimator, and consequently, the number of simulations. This technique divides the domain of each random variable into K non-overlapping sub-domains on the basis of equal probability. For each sub-domain, a value is selected randomly with respect to its probability density. This operation is repeated N/K times. This method reduces variance by ensuring that there are realizations in each sub-domain. Thus for N simulations and K sub-domains, the estimator given by equation A.9 becomes:

$$\Theta^{LH} = \frac{1}{N} \sum_{i=1}^{N/K} \sum_{j=1}^K \mathbf{1}_{\mathcal{D}}(\mathbf{X}_j^{(i)}) G(\mathbf{X}_j^{(i)}). \quad (\text{A.11})$$

Figure A.2 compares simulations using Monte Carlo crude and Latin Hypercube sampling. Note that when Latin Hypercube sampling is implemented, the points are distributed more uniformly over the domain of the problem. Therefore, the evaluation of the expected value of the quantity of interest requires less simulations to estimate the solution.

APPENDIX B

BASICS OF FUZZY LOGIC

B.1 Fuzzy Sets

Fuzzy sets describe the meaning of *vague* or *imprecise* words. The difference between classical (or crisp) and fuzzy sets can be illustrated through the example presented in Figure B.1 (Ross, 2004). In a crisp set boundary (Figure B.1a), the points a and b clearly belong to the crisp set A ; and c is unambiguously not a member of A . In contrast, in a fuzzy set boundary (Figure B.1b), the point a belongs certainly to \tilde{A} and the point c is not a member of \tilde{A} . However, the membership of point b , which is on the boundary region, is ambiguous. Therefore, the degree of membership of b is associated with *membership function*. The membership function of the fuzzy set \tilde{A} is noted $\tilde{\mu}_{\tilde{A}}(\cdot)$ and varies between 0 and 1 –i.e., $\tilde{\mu}_{\tilde{A}}(\cdot) \in [0, 1]$. Let X be the universe of discourse, and x be a generic element of X , then a *fuzzy set* \tilde{A} in X is defined as the set of ordered pairs:

$$\tilde{A} = \{(x, \tilde{\mu}_{\tilde{A}}(x)) | x \in X\} \tag{B.1}$$

From the above discussion, it is observed that the construction of fuzzy sets depend on:

1. the identification of a suitable universe of discourse X and
2. the specification of an appropriate membership function $\tilde{\mu}_{\tilde{A}}(x)$.

The specification of membership functions is *subjective*, which means that the membership functions specified for the same concept may vary considerably. This subjectivity is originated from individual differences in perceiving or expressing abstract concepts. The definition of fuzzy sets is a simple extension of the definition of classical sets. Thus, if the value of the membership function $\tilde{\mu}_{\tilde{A}}(x)$ is restricted to either 0 or 1, then \tilde{A} is reduced to a classical set.

B.1.1 Characteristics of fuzzy sets

A fuzzy set is uniquely specified by its membership function which is defined by the following characteristics:

1. The *support* of a fuzzy set \tilde{A} is the set of all points $x \in X$ such that $\tilde{\mu}_{\tilde{A}}(x) > 0$:

$$\text{support}(\tilde{A}) = \{x | \tilde{\mu}_{\tilde{A}}(x) > 0\} \tag{B.2}$$

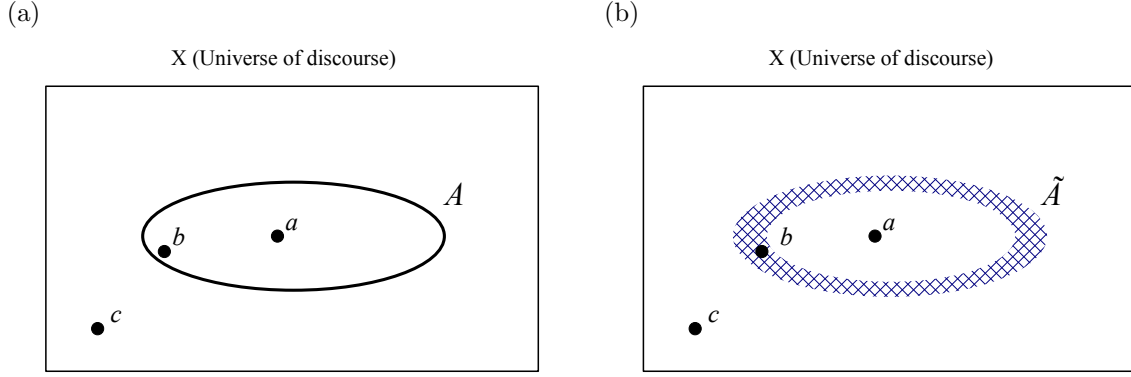


Figure B.1: (a) Crisp set boundary. (b) Fuzzy set boundary.

2. The *core* of a fuzzy set \tilde{A} is the set of all points $x \in X$ such that $\tilde{\mu}_{\tilde{A}}(x) = 1$:

$$\text{core}(\tilde{A}) = \{x | \tilde{\mu}_{\tilde{A}}(x) = 1\} \quad (\text{B.3})$$

3. The *crossover point* of a fuzzy set \tilde{A} is a point $x \in X$ at which $\tilde{\mu}_{\tilde{A}}(x) = 0.5$:

$$\text{crossover}(\tilde{A}) = \{x | \tilde{\mu}_{\tilde{A}}(x) = 0.5\} \quad (\text{B.4})$$

B.1.2 Set theoretical operations

Fuzzy sets have similar operations corresponding to ordinary set operations (union, intersection, and complement). Before describing these set operations, the notion of containment is defined. The fuzzy set \tilde{A} is contained in the fuzzy set \tilde{B} (or, equivalently, \tilde{A} is a subset of \tilde{B} , or \tilde{A} is smaller than or equal to \tilde{B}) if and only if:

$$\tilde{A} \subseteq \tilde{B} \Leftrightarrow \tilde{\mu}_{\tilde{A}}(x) \leq \tilde{\mu}_{\tilde{B}}(x) \quad (\text{B.5})$$

Thus the main *set operations* for fuzzy sets are:

1. The *union* or *disjunction* of two fuzzy sets \tilde{A} and \tilde{B} is a fuzzy set \tilde{C} , written as $\tilde{C} = \tilde{A} \cup \tilde{B}$ or $\tilde{C} = \tilde{A}$ OR \tilde{B} , whose membership function is related to those of \tilde{A} and \tilde{B} by:

$$\tilde{\mu}_{\tilde{C}}(x) = \max[\tilde{\mu}_{\tilde{A}}(x), \tilde{\mu}_{\tilde{B}}(x)] = \tilde{\mu}_{\tilde{A}}(x) \vee \tilde{\mu}_{\tilde{B}}(x) \quad (\text{B.6})$$

2. The *intersection* or *conjunction* of two fuzzy sets \tilde{A} and \tilde{B} is a fuzzy set \tilde{C} , written as $\tilde{C} = \tilde{A} \cap \tilde{B}$ or $\tilde{C} = \tilde{A}$ AND \tilde{B} , whose membership function is related to those of \tilde{A} and \tilde{B} by:

$$\tilde{\mu}_{\tilde{C}}(x) = \min[\tilde{\mu}_{\tilde{A}}(x), \tilde{\mu}_{\tilde{B}}(x)] = \tilde{\mu}_{\tilde{A}}(x) \wedge \tilde{\mu}_{\tilde{B}}(x) \quad (\text{B.7})$$

3. The *complement* or *negation* of a fuzzy set \tilde{A} , denoted by $\tilde{\bar{A}}$ is defined as:

$$\tilde{\mu}_{\tilde{\bar{A}}}(x) = 1 - \tilde{\mu}_{\tilde{A}}(x) \quad (\text{B.8})$$

4. The *cartesian product* of the fuzzy sets A and B which are respectively defined in X and Y , is a fuzzy set in the product space $X \times Y$ with the membership function:

$$\tilde{\mu}_{\tilde{A} \times \tilde{B}}(x, y) = \min[\tilde{\mu}_{\tilde{A}}(x), \tilde{\mu}_{\tilde{B}}(y)] \quad (\text{B.9})$$

5. Similarly, the *cartesian co-product* $A + B$ is a fuzzy set with the membership function:

$$\tilde{\mu}_{\tilde{A} + \tilde{B}}(x, y) = \max[\tilde{\mu}_{\tilde{A}}(x), \tilde{\mu}_{\tilde{B}}(y)] \quad (\text{B.10})$$

B.2 Fuzzy inference systems

Also known as fuzzy-rule-based system, fuzzy expert system, or fuzzy logic controller, the fuzzy inference system (FIS) is a popular computing framework which has been successfully applied to a wide variety of fields such as automatic control, data classification, decision analysis, expert systems, time series prediction, robotics, etc. The FIS is based on the concepts of fuzzy set theory, fuzzy if-then rules, and fuzzy reasoning and is basically composed of three conceptual components (Jang et al., 1997):

1. a *rule base*, which contains the set of fuzzy rules;
2. a *database* (or *dictionary*), which defines the membership functions; and
3. a *reasoning mechanism*, which performs the inference procedure between the rules and the membership functions.

Figure B.2 depicts a typical block diagram for a FIS. The system can take either fuzzy or crisp inputs. However, the output of the FIS at the end of the aggregator block is fuzzy. Due to the fact that for many engineering applications it is suitable to have crisp outputs, a defuzzification procedure transforms the output fuzzy set into a crisp single value. The most popular fuzzy inference systems in engineering applications are (Jang et al., 1997; Ross, 2004):

- Mamdani fuzzy models,
- Sugeno fuzzy models and
- Tsukamoto fuzzy models.

The following subsection presents the Sugeno fuzzy inference system which has been implemented in this study to model the randomness related to vagueness and imprecision.

B.2.1 Sugeno fuzzy models

The Sugeno fuzzy inference system (also known as the TSK fuzzy model) aims to develop a systematic approach for generating fuzzy rules from a given input-output data set. A typical fuzzy rule in a

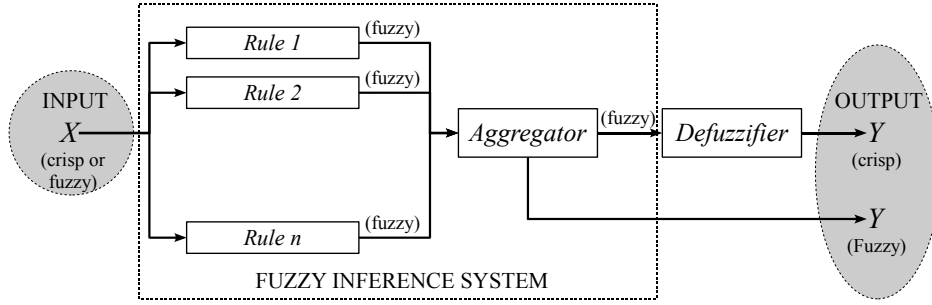


Figure B.2: Block diagram for fuzzy inference systems.

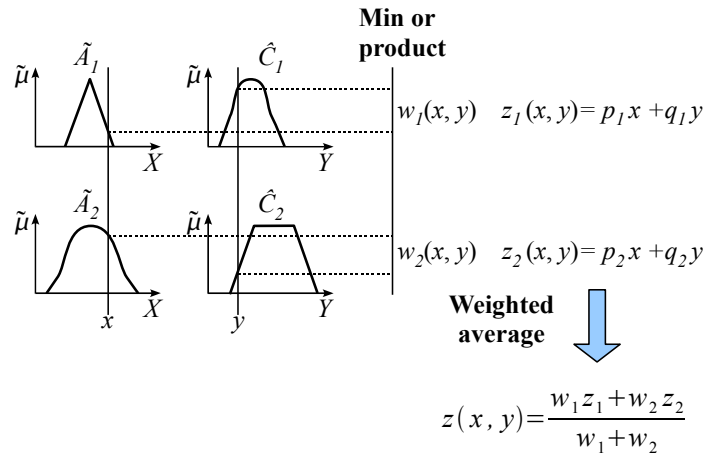


Figure B.3: The Sugeno fuzzy model.

Sugeno fuzzy model takes the form:

$$\underbrace{\text{if } x \text{ is } \tilde{A} \text{ and } y \text{ is } \tilde{B}}_{\text{Input}} \text{ then } \underbrace{z = f(x, y)}_{\text{Output}} \quad (\text{B.11})$$

where \tilde{A} and \tilde{B} are fuzzy sets in the input and $z = f(x, y)$ is a crisp function in the output. Usually $f(x, y)$ is polynomial in terms of the input variables x and y , but it can be any function as long as it can appropriately describe the output of the model within the fuzzy region specified by the antecedent of the rule.

Figure B.3 shows the fuzzy reasoning procedure for a Sugeno fuzzy model. This system has two inputs x and y and one output z related by the following rules:

$$\begin{cases} \text{if } x \text{ is } \tilde{A}_1 \text{ and } y \text{ is } \tilde{C}_1 & \text{then } z_1(x, y) = p_1x + q_1y \\ \text{if } x \text{ is } \tilde{A}_2 \text{ and } y \text{ is } \tilde{C}_2 & \text{then } z_2(x, y) = p_2x + q_2y \end{cases} \quad (\text{B.12})$$

where p_1, p_2, q_1 and q_2 are constants of the output function. Note that since each rule has a crisp

output –i.e., z_1 and z_2 , the overall output z is obtained via weighted average:

$$z(z, y) = \frac{w_1(x, y)z_1(x, y) + w_2(x, y)z_2(x, y)}{w_1(x, y) + w_2(x, y)} \quad (\text{B.13})$$

where w_1 and w_2 can be estimated as the Cartesian product of the membership functions (i.e., equation B.10):

$$\begin{aligned} w_1(x, y) &= \min[\tilde{\mu}_{\tilde{A}_1}(x), \tilde{\mu}_{\tilde{C}_1}(y)] \text{ or } w_1(x, y) = \tilde{\mu}_{\tilde{A}_1}(x)\tilde{\mu}_{\tilde{C}_1}(y) \\ w_2(x, y) &= \min[\mu_{\tilde{A}_2}(x), \tilde{\mu}_{\tilde{C}_2}(y)] \text{ or } w_2(x, y) = \tilde{\mu}_{\tilde{A}_2}(x)\tilde{\mu}_{\tilde{C}_2}(y) \end{aligned} \quad (\text{B.14})$$

The advantage of the Sugeno model is that it directly computes the crisp output, avoiding the time-consuming process of defuzzification required for other fuzzy models. However, this simplification could lead to the loss of membership function linguistic meanings unless the sum of firing strengths (that is, $\sum_i w_i$) is close to unity.

BIBLIOGRAPHY

- Ababneh, A., Benboudjema, F., and Xi, Y. (2003). Chloride penetration in unsaturated concrete. *Journal of Materials in Civil Engineering ASCE*, 15:183–191.
- ACI Committee 215 (1993). Considerations for design of concrete structures subjected to fatigue loading. Technical Report ACI 215R-74, American Concrete Institute.
- Ahn, S., Lawrence, F., and Metzger, M. (1992). Corrosion fatigue of an HSLA steel. *Fatigue and Fracture of Engineering Materials and Structures*, 15:625–642.
- Ahn, W. and Reddy, D. (2001). Galvanostatic testing for the durability of marine concrete under fatigue loading. *Cement and Concrete Research*, 31:343–349.
- Akita, H., Fujiwara, T., and Ozaka, Y. (1997). A practical procedure for the analysis of moisture transfer within concrete due to drying. *Magazine of Concrete Research*, 49(179):129–137.
- Alonso, C., Andrade, C., Rodriguez, J., and Diez, J. (1998). Factors controlling cracking of concrete affected by reinforcement corrosion. *Materials and Structures*, 21(211):435–441.
- Andrade, C., Alonso, C., and Molina, F. (1993). Cover cracking as a function of rebar corrosion: Part 1—experimental test. *Material and Structures*, 26:453–464.
- Barsom, J. and Rolfe, S. (1999). *Fracture and fatigue control in structures*. ASTM, Philadelphia.
- Bazant, Z. (1979). Physical model for steel corrosion in concrete sea structures—theory. *Journal of the Structural Division ASCE*, 105:1137–1153.
- Bazant, Z. and Najjar, L. (1971). Drying of concrete as a nonlinear diffusion problem. *Cement and Concrete Research*, 1:461–473.
- Bazant, Z. and Najjar, L. (1972). Nonlinear water diffusion in nonsaturated concrete. *Materials and Structures*, 5(25):3–20.
- Bazant, Z. and Thonguthai, W. (1978). Pore pressure and drying of concrete at high temperature. *Journal of the Engineering Mechanics Division ASCE*, 104:1059–1079.
- Bhide, S. (1999). Material usage and condition of existing bridges in the U.S. Technical Report SR342, Portland Cement Association, Skokie, Ill.
- Blockley, D. (1996). *Process re-engineering for safety*, pages 51–66. Telford.

- Brunauer, S., Skalny, J., and Bodor, E. (1969). Adsorption in nonporous solids. *Journal of Colloid Interface Science*, 30:546–552.
- CC Technologies Laboratories Inc. (2001). Corrosion costs and preventive strategies in the United States. Technical Report FHWA-RD-01-156, Federal Highway Administration (FHWA), Office of Infrastructure Research and Development.
- Chen, G. and Duquette, D. (1992). Corrosion fatigue of a precipitation-hardened Al-Li-Zr alloy in a 0.5 M sodium chloride solution. *Metallurgical transactions*, 23:1563–1572.
- Chen, G., Wan, K., Gao, M., Wei, R., and Flournoy, T. (1996). Transition from pitting to fatigue crack growth modeling of corrosion fatigue crack nucleation in a 2024-t3. aluminum alloy. *Materials Science and Engineering*, A219:126–132.
- Clifton, J. (1993). Predicting the service life of concrete. *ACI Materials Journal*, (90):611–617.
- Collepari, M., Marciallis, A., and Turriziani, R. (1972). Penetration of chloride ions in cement pastes and in concretes. *Journal of the American Ceramic Society*, 55(10):534–535.
- Duracrete (2000). Statistical quantification of the variables in the limit state functions. Technical report, The European Union - Brite EuRam III - Contract BRPR-CT95-0132 - Project BE95-1347/R9.
- European standard (2004). *Eurocode 1 and 2: Basis of design and actions on structures and design of concrete structures*, afnor edition.
- Fang, C., Lundgren, K., Chen, L., and Zhu, C. (2004). Corrosion influence on bond in reinforced concrete. *Cement and Concrete Research*, 34:2159–2167.
- Gangloff, R. (2005). *Environmental cracking corrosion fatigue*, pages 302–21. ASTM International, West Conshohocken.
- Geocisa and the Torroja Institute (2002). Contecvet: A validated users manual for assessing the residual service life of concrete structures. manual for assessing corrosion-affected concrete structures. annex C calculation of a representative corrosion rate. Technical Report EC Innovation Program IN309021, Geocisa and Torroja Institute.
- Ghanem, R. and Spanos, P. (1991). *Stochastic Finite Elements: A Spectral Approach*. Springer, New York, USA.
- Glass, G. and Buenfeld, N. (2000). The influence of the chloride binding on the chloride induced corrosion risk in reinforced concrete. *Corrosion Science*, 42(2):329–344.
- González, J., Andrade, C., Alonso, C., and Feliú, S. (1995). Comparison of rates of general corrosion and maximum pitting penetration on concrete embedded steel reinforcement. *Cement and Concrete Research*, 25:257–264.
- Goswami, T. and Hoepfner, D. (1995). *Pitting corrosion fatigue of structural materials*, pages 129–139. ASME, New York.

- Grata, J. (2005). Road salt, hits from trucks likely led to bridge collapse. *Pittsburgh Post-Gazette*.
- Gut, A. (2005). *Probability: A Graduate Course*. Springer Texts in Statistics.
- Haldar, A. and Mahadevan, S. (2000). *Probability, Reliability, and Statistical Methods in Engineering Design*. John Wiley and Sons.
- Han, S. (2007). Influence of diffusion coefficient on chloride ion penetration of concrete structures. *Construction and Building Materials*, 21(2):370–378.
- Harlow, D. and Wei, R. (1998). A probability model for the growth of corrosion pits in aluminum alloys induced by constituent particles. *Engineering Fracture Mechanics*, 59:305–325.
- Houghton, J. (2005). Global warming. *Reports on Progress in Physics*, 68:1343–1403.
- Husni, R. e. a. (2003). *Acciones sobre las estructuras de hormigón*, pages 39–108. Red Rehabilitar CYTED, Guarulhos.
- IPCC (2007). Climate change 2007: The physical science basis. Contribution of working group I to the fourth assessment report of the intergovernmental panel on climate change. Technical report, Intergovernmental Panel on Climate Change.
- Jaffer, S. and Hansson, C. (2008). The influence of cracks on chloride-induced corrosion of steel in ordinary Portland cement and high performance concretes subjected to different loading conditions. *Corrosion Science*, 50(12):3343–3355.
- Jang, J.-S. R., Sun, C.-T., and Mizutani, E. (1997). *Neuro-fuzzy and soft computing: a computational approach to learning and machine intelligence*. Prentice-Hall, Upper Saddle River, USA.
- Jones, D. (1992). *Principles and prevention of corrosion*. Macmillan Publishing Co, New York.
- Kent, D. and Park, R. (1971). Flexural members with confined concrete. *Journal of the Structural Division ASCE*, 97:1969–1990.
- Khan, A., Cook, W., and Mitchell, D. (1998). Thermal properties and transient thermal analysis of structural members during hydration. *ACI Materials Journal*, 95(3):293–303.
- Kondo, Y. (1989). Prediction of fatigue crack initiation life based on pit growth. *Corrosion*, 45:7–11.
- Liang, M., Jin, W., Yang, R., and Huang, N. (2005). Predeterminate model of corrosion rate of steel in concrete. *Cement and concrete research*, (35):1827–1833.
- Liang, M., Lin, L., and Liang, C. (2002). Service life prediction of existing reinforced concrete bridges exposed to chloride environment. *Journal of Infrastructure Systems ASCE*, 8(3):76–85.
- Liang, M. and Yang, R. (2004). Theoretical elucidation on the on-site measurements of corrosion rate of reinforcements. *Construction and building materials*, 19:175–180.
- Liu, Y. (1996). *Modeling the Time-to-Corrosion Cracking of the Cover Concrete in Chloride Contaminated Reinforced Concrete Structures*. PhD thesis, Virginia Polytechnic Institute and State University, Blacksburg, Virginia.

- Liu, Y. and Weyers, R. (1998). Modeling the time-to-corrosion cracking of the cover concrete in chloride contaminated reinforced concrete structures. *ACI Materials Journal*, 95:675–681.
- López, W., González, J., and Andrade, C. (1993). Influence of temperature on the service life of rebars. *Cement and Concrete Research*.
- Lounis, Z. (2005). *Uncertainty modeling of chloride contamination and corrosion of concrete bridges*, pages 491–511. Springer, USA.
- Martín-Pérez, B., Pantazopoulou, S., and Thomas, M. (2001). Numerical solution of mass transport equations in concrete structures. *Computers and Structures*, 79:1251–1264.
- McGee, R. (2000). Modelling of durability performance of Tasmanian bridges. In Melchers, R. and Stewart, M., editors, *Applications of statistics and probability in civil engineering*, pages 297–306, Rotterdam. Balkema.
- Melchers, R. (1999). *Structural reliability-analysis and prediction*. Ellis Horwood Series in Civil Engineering, Chichester.
- Mori, Y. and Ellingwood, B. (1995). Reliability-based life prediction of structures degrading due to environment and repeated loading. In Lemaire, M., Favre, J., and Mébarki, A., editors, *Applications of Statistics and Probability: Civil Engineering Reliability and Risk Analysis*, pages 971–976, Paris, France. Balkema.
- Murakami, Y. and Nisitani, H. (1975). Stress intensity factor for circumferentially cracked round bar in tension. *Transactions of the Japan Society of Mechanical Engineers*, 41:360–369.
- Neville, A. (1981). *Properties of Concrete (3rd ed.)*. Longman Scientific & Technical.
- Neville, A. (1995). Chloride attack of reinforced concrete: an overview. *Materials and Structures*, 28:63–70.
- Nielsen, A. (1985). *Durability*, pages 200–243. Aalborg Cement Company, Aalborg Portland.
- Nilsson, L.-O., Massat, M., and Tang, L. (1994). The effect of non-linear chloride binding on the prediction of chloride penetration into concrete structure. In Malhotra, V., editor, *Durability of Concrete, ACI SP-145*, pages 469–486, Detroit, USA. ACI.
- Niu, D., Wang, L., and Wang, Q. (1996). Determination of the diffusion coefficient of dioxidation in concrete. *Journal of Xian University of Science and Technology*, 28:6–9. In Chinese.
- Page, C., Short, N., and Tarras, A. E. (1981). Diffusion of chloride ions in hardened cement pastes. *Cement and Concrete Research*, 11(3):395–406.
- Papadakis, V., Roumeliotis, A., Fardis, M., and Vagenas, C. (1996). *Mathematical modelling of chloride effect on concrete durability and protection measures*, pages 165–174. E&FN Spon, London (UK).
- Rajasankar, J. and Iyer, N. (2006). A probability-based model for growth of corrosion pits in aluminum alloys. *Engineering Fracture Mechanics*, 73:553–570.

- Ross, S. and Pekoz, E. (2007). *A Second Course in Probability*. Pekozbooks, Boston, MA.
- Ross, T. (2004). *Fuzzy Logic with Engineering Applications*. Wiley, Chinchester, 2 edition.
- Saetta, A., Scotta, R., and Vitaliani, R. (1993). Analysis of chloride diffusion into partially saturated concrete. *ACI Materials Journal*, 90(5):441–451.
- Salah el Din, A. and Lovegrove, J. (1982). Fatigue of cold worked ribbed reinforcing bar – a fracture mechanics approach. *International Journal of Fatigue*, 4:15–26.
- Samson, E. and Marchand, J. (2007). Modeling the transport of ions in unsaturated cement-based materials. *Computers and Structures*, 85:1740–1756.
- Schiessl, P. and Raupach, M. (1997). Laboratory studies and calculations on the influence of crack width on chloride-induced corrosion of steel in concrete. *ACI Materials Journal*, 94:56–62.
- Schijve, J. (2004). *Fatigue of structures and materials*. Kluwer academic publisher, New York.
- Shi, P. and Mahadevan, S. (2001). Damage tolerance approach for probabilistic pitting corrosion fatigue life prediction. *Engineering Fracture Mechanics*, 68:1493–1507.
- Smithson, M. (1989). *Ignorance and uncertainty: emerging paradigms*. Springer-Verlag, New York.
- Stewart, M. (2004). Spatial variability of pitting corrosion and its influence on structural fragility and reliability of RC beams in flexure. *Structural Safety*, 26:453–470.
- Sudret, B. and Der Kiureghian, A. (2000). Stochastic finite elements and reliability – a state-of-the-art report. Technical Report UCB/SEMM-2000/08.
- Suresh, S. (1998). *Fatigue of materials*. Cambridge University Press, 2 edition edition.
- Tang, L. and Nilsson, L. (1993). Chloride binding capacity and binding isotherms of OPC pastes and mortars. *Cement and Concrete Research*, 23:247–253.
- Thoft-Christensen, P. (2000). Stochastic modelling of the crack initiation time for reinforced concrete structures. In *ASCE Structures Congress*, Philadelphia, USA.
- Thoft-Christensen, P. (2002). Deterioration of concrete structures. In *Proceedings of the First International Conference on Bridge Maintenance, Safety and Management, IABMAS'02*, Barcelona, Spain.
- Tuutti, K. (1982). Corrosion of steel in concrete. *Swedish Cement and Concrete Institute*.
- Val, D. (2006). Service-life performance of RC structures made with supplementary cementitious materials in chloride-contaminated environments. In *Proceedings of the international RILEM-JCI seminar on concrete durability and service life planning*, pages 363–373, Ein-Bokek, Israel.
- Val, D. and Melchers, R. (1997). Reliability of deteriorating RC slab bridges. *Journal of Structural Engineering ASCE*, 123(12):1638–1644.

- Val, D. and Stewart, M. (2003). Life-cycle analysis of reinforced concrete structures in marine environments. *Structural safety*, 25:343–362.
- Val, D. and Trapper, P. (2008). Probabilistic evaluation of initiation time of chloride-induced corrosion. *Reliability Engineering and System Safety*, 93:364–372.
- Vu, K. (2003). *Corrosion-induced cracking and spatial time-dependent reliability analysis of reinforced concrete structures*. PhD thesis, University of Newcastle, New South Wales, Australia.
- Vu, K. and Stewart, M. (2000). Structural reliability of concrete bridges including improved chloride-induced corrosion. *Structural Safety*, 22:313–333.
- Vu, K. and Stewart, M. (2005). Predicting the likelihood and extent of reinforced concrete corrosion-induced cracking. *Journal of Structural Engineering ASCE*, 131:1681–1689.
- Vu, K., Stewart, M., and Mullard, J. (2005). Corrosion-induced cracking: Experimental data and predictive models. *ACI Structural Journal*, 102:719–726.
- Xi, Y., Bažant, Z., and Jennings, H. (1994). Moisture diffusion in cementitious materials – adsorption isotherms. *Advanced Cement Based Materials*, 1(6):248–257.
- Yokozeki, K., Motohashi, K., Okada, K., and Tsutsumi, T. (1997). A rational model to predict the service life of RC structures in a marine environment. In *Fourth CANMET/ACI International Conference on Durability of Concrete*, pages 778–799.
- Zhang, R. and Mahadevan, S. (2001). Reliability-based reassessment of corrosion fatigue life. *Structural safety*, 23:77–91.